



SENS4ICE

SENSORS AND CERTIFIABLE HYBRID ARCHITECTURES
FOR SAFER AVIATION IN ICING ENVIRONMENT

Final report on evaluation of technologies developed in SENS4ICE and technical project results

Deliverable D4.4

Lead beneficiary (organisation):	DLR
Document manager:	Christoph Deiler
Actual submission date:	06/02/2024
Dissemination level:	Public
Grant Agreement number:	824253
Project acronym:	SENS4ICE
Project title:	SENSors and certifiable hybrid architectures FOR safer aviation in ICing Environment
Funding scheme:	Research and Innovation Action
Project coordinator:	DLR (German Aerospace Center)
Project website:	www.sens4ice-project.eu



This project has received funding from the European Union's Horizon 2020 research and innovation programme under grant agreement No 824253.



File name **SENS4ICE_D4.4_Final_Report_DLR_20240131_v2.docx**

APPROVALS

Role	Name	Organisation	Date
Coordinator	Schwarz	DLR	31 JAN 2024
WP leader	Deiler	DLR	19 DEC 2023
Task leader	Deiler	DLR	19 DEC 2023
Other (quality)	Behrendt	L-UP	22 JAN 2024

DOCUMENT HISTORY

Version	Date	Modification	Author
1	30 NOV 2023	Created	Deiler
2	18 DEC 2023	Finalized	Schwarz
3	22 JAN 2024	Quality review	Behrendt

LIST OF AUTHORS

Name	Organisation
Document manager/editor/WP4 lead/Task 4.4 lead: Christoph DEILER	DLR
Project coordinator and co-editor: Carsten SCHWARZ	DLR
Task 4.1 lead: El Hassan RIDOUANE	Collins Aerospace
Task 4.2 lead: Annagrazia ORAZZO	SAFRAN
Task 4.3 lead: Tina JURKAT-WITSCHAS	DLR
Contributors:	DLR, ATR, AeroTex, CIRA, CNRS-Safire, Collins, Embraer, Honeywell, INTA, Leonardo, L-up, ONERA, TU Braunschweig, SAFRAN, NRC

DISTRIBUTION LIST

This deliverable report is public.





TABLE OF CONTENTS

EXECUTIVE SUMMARY	13
1. INTRODUCTION	13
2. SLD ICE WIND TUNNEL TESTING	15
3. SLD ICING FLIGHT TEST CAMPAIGNS AND ATMOSPHERE CHARACTERISATION	19
3.1. FLIGHT CAMPAIGN NORTH AMERICA	21
3.2. FLIGHT CAMPAIGN EUROPE	27
3.3. COMPARISON OF FLIGHT CAMPAIGN RESULTS WITH APPENDIX O ENVELOPES.....	35
4. SATELLITE-BASED DETECTION AND NOWCASTING OF ICING CONDITIONS	37
5. DIRECT ICE DETECTION TECHNOLOGIES DEVELOPMENT, MATURATION AND DEMONSTRATION	40
5.1. AEROTEX AIP - ATMOSPHERIC ICING PATCH	41
5.1.1. <i>Technology Description</i>	41
5.1.2. <i>Technology status at project start</i>	42
5.1.3. <i>Technical Work</i>	42
5.1.4. <i>Flight Test</i>	43
5.1.5. <i>Current TRL</i>	44
5.1.6. <i>Short summary of further development, maturation and exploitation</i>	44
5.2. COLLINS – IDS	45
5.2.1. <i>Technology Description</i>	45
5.2.2. <i>Technology status at project start</i>	46
5.2.3. <i>Technical Work</i>	46
5.2.4. <i>Flight Test</i>	46
5.2.5. <i>Current TRL</i>	48
5.2.6. <i>Short summary of further development, maturation, and exploitation</i>	48
5.3. DLR – LILD	49
5.3.1. <i>Technology Description</i>	49
5.3.2. <i>Technology status at project start</i>	49
5.3.3. <i>Technical Work</i>	49
5.3.4. <i>Flight Test</i>	50
5.3.5. <i>Current TRL</i>	52
5.3.6. <i>Short summary of further development, maturation, and exploitation</i>	52
5.4. DLR – CM2D	53
5.4.1. <i>Technology Description</i>	53
5.4.2. <i>Technology status at project start</i>	53
5.4.3. <i>Technical Work</i>	53
5.4.4. <i>Flight Test</i>	54
5.4.5. <i>Current TRL</i>	56
5.4.6. <i>Short summary of further development, maturation, and exploitation</i>	56
5.5. HONEYWELL – SRP	57
5.5.1. <i>Technology Description</i>	57
5.5.2. <i>Technology status at project start</i>	57
5.5.3. <i>Technical Work</i>	57
5.5.4. <i>Flight Test</i>	58
5.5.5. <i>Current TRL</i>	59
5.5.6. <i>Short summary of further development, maturation, and exploitation</i>	59
5.6. INTA – FOD	60
5.6.1. <i>Technology Description</i>	60
5.6.2. <i>Technology status at project start</i>	61
5.6.3. <i>Technical Work</i>	61
5.6.4. <i>Flight Test</i>	61
5.6.5. <i>Current TRL</i>	63
5.6.6. <i>Short summary of further development, maturation and exploitation</i>	63





5.7. ONERA – AHDEL	64
5.7.1. <i>Technology Description</i>	64
5.7.2. <i>Technology status at project start</i>	65
5.7.3. <i>Technical Work</i>	65
5.7.4. <i>Ice Wind Tunnel Tests</i>	65
5.7.5. <i>Flight Test</i>	67
5.7.6. <i>Current TRL</i>	67
5.7.7. <i>Short summary of further development, maturation and exploitation</i>	67
5.8. ONERA – AMPERA.....	68
5.8.1. <i>Technology Description</i>	68
5.8.2. <i>Technology status at project start</i>	69
5.8.3. <i>Technical Work</i>	69
5.8.4. <i>Flight Test</i>	70
5.8.5. <i>Current TRL</i>	71
5.8.6. <i>Short summary of further development, maturation and exploitation</i>	71
5.9. SAFRAN – AOD	72
5.9.1. <i>Technology Description</i>	72
5.9.2. <i>Technology status at project start</i>	72
5.9.3. <i>Technical Work</i>	72
5.9.4. <i>Laboratory Tests</i>	73
5.9.5. <i>Ice Wind Tunnel Tests</i>	75
5.9.6. <i>Current TRL</i>	75
5.9.7. <i>Short summary of further development, maturation and exploitation</i>	75
5.10. SAFRAN – PFIDS	76
5.10.1. <i>Technology Description</i>	76
5.10.2. <i>Technology status at project start</i>	76
5.10.3. <i>Technical Work</i>	77
5.10.4. <i>Flight Test</i>	77
5.10.5. <i>Current TRL</i>	79
5.10.6. <i>Short summary of further development, maturation and exploitation</i>	79
6. HYBRID ICE DETECTION ARCHITECTURE INCLUDING INDIRECT ICE DETECTION	80
6.1. SHORT SUMMARY.....	80
6.2. GENERAL DESCRIPTION OF THE HIDS	81
6.2.1. <i>Specific Implementation during the North American Campaign</i>	83
6.2.2. <i>Specific Implementation during the European Campaign</i>	83
6.3. INDIRECT ICE DETECTION ALGORITHM AND IMPLEMENTATION	84
6.4. FLIGHT TEST RESULTS	87
6.4.1. <i>North American Flight Test Campaign</i>	87
6.4.2. <i>European Flight Test Campaign</i>	94
6.5. FURTHER DEVELOPMENT, MATURATION AND EXPLOITATION	105
7. CONCLUSIONS AND RECOMMENDATIONS	106
7.1. TRL PROGRESS IN SENS4ICE.....	106
7.2. DIRECT AND REMOTE ICE DETECTION TECHNOLOGY CONCLUSIONS	108
7.3. HYBRID AND INDIRECT ICE DETECTION CONCLUSIONS.....	108
7.4. SENS4ICE RECOMMENDATIONS	109
8. REFERENCES	111
9. ANNEX HORIZON 2020 TRL DEFINITIONS	113





GLOSSARY

Acronym	Signification
A/C	Aircraft
AHDEL	Atmospheric Hydrometeor Detector based on Electrostatics
AIP	Atmospheric Icing Patch
AIWT	Atmospheric Icing Wind Tunnel
AMPERA	Atmospheric Measurement of Potential and ElectRic field on Aircraft
AOD	Appendix O Discriminator
APP. C	Appendix C
APP. O	Appendix O
BCPD	Backscatter Cloud Probe with Polarization Detection
BIWT	Braunschweig Icing Wind Tunnel
CAD	Computer-Aided Design
CCP	Cloud Combination Probe
CDP	Cloud Droplet Probe
CER	Contrôle Essais Réception / Dedicated ATC for tests & acceptance
CM2D	Cloud Multi-Detection Device
D	Deliverable
DID	Direct Ice Detection
DIDS	Direct Ice Detection Sensors
DWT	Discrete Wavelet Transforms
EFM	Electric Field Mill
FBGS	Fiber Bragg Grating Sensors
FDAU	Flight Data Acquisition Unit
FOD	Fiber Optic Detector
FPGA	Field-Programmable Gate Array
FT	Flight Test
FTI	Flight Test Instrumentation
FZDZ	Freezing Drizzle
FZRA	Freezing Rain
HIDS	Hybrid Ice Detection System





IAR	Ice Accretion Rate
IC	Icing Condition
IDS	Ice Differentiator System
IID	Indirect Ice Detection
IIDS	Indirect Ice Detection System
IWT	Icing Wind Tunnel
IPS	Ice Protection System
LILD	Local Ice Layer Detector
LW	Liquid Water Icing Conditions
LWC	Liquid Water Content
MED	Median Effective Diameter
MRL	Manufacturing Readiness Level
MVD	Median Volume Diameter
NRC	National Research Council of Canada
OF	Observational Flight
PC	Personal Computer
PCB	Printed Circuit Board
PFIDS	Primary in-Flight Icing Detection System
PICU	Power Interface Control Unit
R&D	Research & Development
SAFIRE	Service des avions français instrumentés pour la recherche en environnement (French facility for airborne research)
SENS4ICE	SENSors and certifiable hybrid architectures for safer aviation in ICing Environment
SLD	Supercooled Large Drops
SRP	Short Range Particulate
TAT	Total Air Temperature
TRL	Technology readiness level
TWC	Total Water Content
TUBS	Technische Universität Braunschweig
UAV	Unmanned Aerial Vehicle
UTC	Coordinated Universal Time





LIST OF FIGURES

FIGURE 1: IMPINGEMENT BEHIND LEADING EDGE POTENTIALLY AFFECTING UNPROTECTED AREAS.....	14
FIGURE 2: SENS4ICE LAYERED SAFETY CONCEPT FOR LIQUID WATER ICING.....	15
FIGURE 3: SENS4ICE SENSOR DETECTION RATES OVERVIEW FOR APP. C AND O ICING CONDITION IWT TEST POINTS FOR SEVEN DETECTION TECHNOLOGIES.....	17
FIGURE 4: MEASURED SENSOR RESPONSE TIMES COMPARED TO REQUIRED RESPONSE TIMES FOR APP. C IWT TEST POINTS (TOP) MEASURED SENSOR RESPONSE TIMES COMPARED TO REQUIRED RESPONSE TIMES FOR DETECTING LIQUID WATER (LW) ICING CONDITIONS FOR APP. O IWT TEST POINTS (BOTTOM).....	18
FIGURE 5: MEASURED SENSOR RESPONSE TIMES COMPARED TO REQUIRED RESPONSE TIMES FOR DIFFERENTIATING APP. C CONDITIONS FROM APP. O CONDITIONS IN IWT (FOR SENSORS PROVIDING DIFFERENTIATION INFORMATION).....	19
FIGURE 6: NORTH AMERICAN FLIGHT CAMPAIGN EMBRAER PHENOM 300 AIRCRAFT [COPYRIGHT EMBRAER/SENS4ICE PROJECT].....	20
FIGURE 7: EUROPEAN FLIGHT CAMPAIGN SAFIRE ATR 42 ENVIRONMENTAL RESEARCH AIRCRAFT [IMAGE DLR/SENS4ICE PROJECT WITH SAFIRE PERMISSION].....	20
FIGURE 8: EMBRAER PHENOM 300 WITH ICE ACCRETION ON WING [COPYRIGHT EMBRAER].....	21
FIGURE 9: SAFIRE ATR 42 HORIZONTAL TAIL WITH ICE ACCRETION [IMAGE DLR/SENS4ICE PROJECT WITH SAFIRE PERMISSION].....	21
FIGURE 10: GROUND TRACKS OF THE NORTH AMERICAN SENS4ICE CAMPAIGN IN FEBRUARY/MARCH 2023[CREDIT DLR/SENS4ICE PROJECT MADE WITH NATURAL EARTH].....	22
FIGURE 11: DISTRIBUTION OF ICD LWC MEASUREMENTS IN APPENDIX C CONDITIONS (LEFT) AND ICD TWC MEASUREMENTS IN APPENDIX O CONDITIONS (RIGHT) FOR NORTH AMERICA FLIGHT CAMPAIGN. THE COUNTS ARE BASED ON 15 SECOND ROLLING AVERAGES WHICH WERE COMPUTED FOR EACH SECOND. BECAUSE APPENDIX O CONDITIONS ARE ONLY DEFINED IF VERY FEW ICE CRYSTALS ARE PRESENT, THE TWC IS ASSUMED TO BE EQUIVALENT TO THE LWC IN THESE CASES.....	23
FIGURE 12: LWC CONTAINED IN SLDS (I.E. ALL DROPLETS WITH DIAMETERS LARGER THAN 100 µM) DURING THE NORTH AMERICAN FLIGHT CAMPAIGN. THE DATA ARE BASED ON 15 SECOND ROLLING AVERAGES.....	23
FIGURE 13: MAP OF SELECTED FLIGHT PATHS FROM THE NORTH AMERICAN CAMPAIGN COLOUR CODED WITH THE LWC MEASURED BY THE ICD. ENHANCED LWD SHOWS REGION OF ICING ENCOUNTERS. ONLY FLIGHTS F1475-1, F1475-2, F1476, F1477-1, F1477-2 ARE INCLUDED IN THE PLOT. [21].....	24
FIGURE 14: ALTITUDE (LEFT) AND TEMPERATURE (RIGHT) PROFILE OF THE ALL ICING ENCOUNTERS OF THE NORTH AMERICAN TEST CAMPAIGN DIVIDED IN APP. C AND APP. O CONDITIONS AS DEFINED ABOVE. SHOWN ARE MEAN AND 95 PERCENTILES OF THE LWC CONTAINED IN APPENDIX C AND APPENDIX O CLASSIFIED CLOUDS. LWC DATA ARE BASED ON 15 SECOND AVERAGES.....	24
FIGURE 15: CUMULATIVE MASS DISTRIBUTIONS FOR EACH APPENDIX O ENCOUNTER OBSERVED DURING THE NORTH AMERICAN FLIGHT TEST CAMPAIGN. MVDs WERE ON AVERAGE 23 µM. THE CUMULATIVE MASS CURVES FOR FREEZING DRIZZLE MVD < 40 µM AND MVD > 40 µM FROM COBER AND ISAAC [31] ARE PLOTTED IN ORANGE AND RED, RESPECTIVELY.....	25
FIGURE 16: NEVZOROV TWC OF THE APPENDIX O ENCOUNTERS DURING THE NORTH AMERICAN SENS4ICE CAMPAIGN IN COMPARISON TO THE LWC ENVELOPES OF FREEZING DRIZZLE MVD < 40 µM (A) AND FREEZING DRIZZLE MVD > 40 µM (B). THE NEVZOROV TWC IS ASSUMED TO BE EQUIVALENT TO THE LWC IN APPENDIX O CONDITIONS BECAUSE APPENDIX O ENCOUNTERS WERE REQUIRED TO CONTAIN FEW ICE CRYSTALS. DUE TO AMBIGUITIES THAT MAY EXIST IN THE DETECTION OF PARTICLES(SEE D4.3) AND DUE TO THE CHANCE OF INTERMITTENT MIXED-PHASE POCKETS THE TWC MEASUREMENT OF THE NEVZOROV MAY BE CONTAMINATED BY ICE AND THUS TOO HIGH FOR SOME OF THE ENCOUNTERS SHOWN. ONLY ENCOUNTERS LONGER THAN 30 SECONDS WERE USED FOR THIS PLOT.....	26
FIGURE 17 PRESSURE AND ALTITUDE OF APPENDIX O CONDITIONS ENCOUNTERED DURING THE NORTH AMERICAN SENS4ICE CAMPAIGN IN COMPARISON TO THE ENVELOPE FOR FZDZ FROM APPENDIX O.....	26
FIGURE 18: FREQUENCY OF OCCURRENCE OF DIFFERENT CLOUD CONDITIONS DURING THE NORTH AMERICAN SENS4ICE CAMPAIGN.....	27
FIGURE 19: FLIGHT CAMPAIGN EUROPE APRIL 2023 GROUND TRACKS [CREDIT SAFIRE/SENS4ICE PROJECT, MAP DATA FROM OPENSTREETMAP].....	28
FIGURE 20: MEAN AND 95TH PERCENTILE OF THE LWC IN APP. C AND APP. O CONDITIONS PLOTTED AGAINST THE TEMPERATURE FOR THE DATA OF THE EUROPEAN FLIGHT TEST CAMPAIGN. THE APP. C VALUES ARE BASED ON THE NEVZOROV LWC SENSOR, THE APPENDIX O VALUES ON THE NEVZOROV TWC SENSOR (SEE D4.3). ONLY FLIGHTS WHERE THE NEVZOROV WORKED ARE USED FOR THIS PLOT. THE DATA ARE BASED ON 30 SECOND AVERAGES.....	30





FIGURE 21: DISTRIBUTION OF NEVZOROV TWC IN APPENDIX C (A) AND APPENDIX O (B) CONDITION DURING THE EUROPEAN SENS4ICE CAMPAIGN. THE COUNTS ARE BASED ON ROLLING 30 SECOND AVERAGES THAT WERE EVALUATED COMPUTED FOR EACH SECOND.....	31
FIGURE 22: HISTOGRAM OF LWC CONTAINED IN SLDs (I.E. ALL DROPLETS WITH DIAMETERS LARGER THAN 100 μm) DURING THE EUROPEAN FLIGHT CAMPAIGN. THE COUNTS ARE BASED ON ROLLING 30 SECOND AVERAGES THAT WERE EVALUATED COMPUTED FOR EACH SECOND.....	32
FIGURE 23: CUMULATIVE MASS DISTRIBUTIONS FOR EACH APPENDIX O ENCOUNTER OBSERVED DURING THE EUROPEAN FLIGHT CAMPAIGN. THE MEAN CURVE IS PLOTTED IN BLACK, THE MVD OF THE MEAN CURVE IS 45 μm . THE CUMULATIVE MASS CURVES FOR FREEZING DRIZZLE MVD < 40 μm AND MVD > 40 μm FROM COBER AND ISAAC [31] ARE PLOTTED IN ORANGE AND RED, RESPECTIVELY.	33
FIGURE 24: NEVZOROV TWC OF THE APPENDIX O ENCOUNTERS DURING THE EUROPEAN SENS4ICE CAMPAIGN IN COMPARISON TO THE LWC ENVELOPES OF FREEZING DRIZZLE MVD < 40 μm (A) AND FREEZING DRIZZLE MVD > 40 μm (B). THE NEVZOROV TWC IS ASSUMED TO BE EQUIVALENT TO THE LWC IN APPENDIX O CONDITIONS BECAUSE APPENDIX O ENCOUNTERS WERE REQUIRED TO CONTAIN FEW ICE CRYSTALS. DUE TO AMBIGUITIES THAT MAY EXIST IN THE DETECTION OF PARTICLES (SEE SENS4ICE DELIVERABLE D4.3 [8]) AND DUE TO THE CHANCE OF INTERMITTENT MIXED-PHASE POCKETS THE TWC MEASUREMENT OF THE NEVZOROV MAY BE CONTAMINATED BY ICE AND THUS TOO HIGH FOR SOME OF THE ENCOUNTERS SHOWN. ONLY ENCOUNTERS LONGER THAN 30 SECONDS WERE USED FOR THIS PLOT.....	33
FIGURE 25: PRESSURE AND ALTITUDE OF APPENDIX O CONDITIONS ENCOUNTERED DURING THE EUROPEAN SENS4ICE CAMPAIGN IN COMPARISON TO THE ENVELOPE FOR FZDZ FROM APPENDIX O.	34
FIGURE 26: OVERVIEW OF SAMPLED TIME IN DIFFERENT CLOUD CONDITIONS FOR ALL FLIGHTS DURING THE EUROPEAN CAMPAIGN (EXCEPT OF3 AND OF4).	35
FIGURE 27: COMPARISON OF THE NEVZOROV TWC MEASURED DURING FREEZING DRIZZLE ENCOUNTERS WITH MVD < 40 μm DURING BOTH FLIGHT CAMPAIGNS WITH THE APPENDIX O ENVELOPE FOR FREEZING DRIZZLE MVD < 40 μm . THE NEVZOROV TWC IS ASSUMED TO BE EQUIVALENT TO THE LWC IN APPENDIX O CONDITIONS BECAUSE APPENDIX O ENCOUNTERS WERE REQUIRED TO CONTAIN FEW ICE CRYSTALS. DUE TO AMBIGUITIES THAT MAY EXIST IN THE DETECTION OF PARTICLES (SEE SECTION 3.3) AND DUE TO THE CHANCE OF INTERMITTENT MIXED-PHASE POCKETS THE TWC MEASUREMENT OF THE NEVZOROV MAY BE CONTAMINATED BY ICE AND THUS TOO HIGH FOR SOME OF THE ENCOUNTERS SHOWN. ONLY ENCOUNTERS LONGER THAN 30 SECONDS WERE USED FOR THIS PLOT.....	36
FIGURE 28: COMPARISON OF THE NEVZOROV TWC MEASURED DURING FREEZING DRIZZLE ENCOUNTERS WITH MVD > 40 μm DURING BOTH FLIGHT CAMPAIGNS WITH THE APPENDIX O ENVELOPE FOR FREEZING DRIZZLE MVD > 40 μm (LEFT: TWO DIFFERENT FLIGHT CAMPAIGNS COLOUR CODED, RIGHT MVD COLOUR CODED). THE NEVZOROV TWC IS ASSUMED TO BE EQUIVALENT TO THE LWC IN APPENDIX O CONDITIONS BECAUSE APPENDIX O ENCOUNTERS WERE REQUIRED TO CONTAIN FEW ICE CRYSTALS. DUE TO AMBIGUITIES THAT MAY EXIST IN THE DETECTION OF PARTICLES (SEE SECTION 3.3) AND DUE TO THE CHANCE OF INTERMITTENT MIXED-PHASE POCKETS THE TWC MEASUREMENT OF THE NEVZOROV MAY BE CONTAMINATED BY ICE AND THUS TOO HIGH FOR SOME OF THE ENCOUNTERS SHOWN. ONLY ENCOUNTERS LONGER THAN 30 SECONDS WERE USED FOR THIS PLOT.	36
FIGURE 29: EXAMPLE OF THE GRAPHICAL OUTPUT OF THE ICING DETECTION ALGORITHM REFERRED TO 25 APRIL 2023 AT 12:00 UTC. THE MAP ON THE LEFT SHOWS THE ICING HAZARD CLASSIFIED IN LIGHT, MODERATE AND SEVERE PLUS AN ADDITIONAL FLAG INDICATING POSSIBLE SLD CONDITIONS. THE TWO MAPS ON THE RIGHT REPORT THE CORRESPONDING MINIMUM AND MAXIMUM ALTITUDES ESTIMATED BY THE ALGORITHM.	37
FIGURE 30: EXAMPLE OF THE METHODOLOGY USED TO COMPARE FLIGHT DATA AND SATELLITE DATA. EACH PANEL SHOWS, ON THE LEFT SIDE, THE MAP OF THE CIRA DETECTION TOOL AND, ON THE RIGHT SIDE, THE TIME SERIES OF THE FLIGHT VARIABLES.	38
FIGURE 31: COMPARISON BETWEEN THE TIME SERIES OF THE VARIABLES OBSERVED DURING THE FLIGHT AND THE OUTPUT OF CIRA DETECTION TOOL.	39
FIGURE 32: AIP HEATER (LEFT) AND AN INSULATED MOUNT (RIGHT).	41
FIGURE 33: EXAMPLE SHOWING SENSOR LOCATIONS ON THE FORWARD FUSELAGE.	41
FIGURE 34: EXAMPLE OF SENSOR RESPONSE FOR LARGE DROPLET ICING CONDITIONS (LOWER).	42
FIGURE 35: CANDIDATE CONFIGURATIONS FOR THE AIP SYSTEM.	42
FIGURE 36: AIP SENSORS MOUNTED ALONG THE CENTRELINE OF THE AIRCRAFT [IMAGE AEROTEX WITH EMBRAER PERMISSION/ SENS4ICE PROJECT].	43
FIGURE 37: AIP SYSTEM RESPONSE FOR FLIGHT 1475, SHOWN ALONGSIDE DATA FROM THE REFERENCE SENSORS.	44
FIGURE 38: OVERVIEW OF COLLINS-IDS STRUCTURE, POSSIBLE MOUNTING LOCATION, AND COMMUNICATION WITH THE AIRCRAFT [PHENOM 300 AIRCRAFT IMAGE COPYRIGHT EMBRAER].	45





FIGURE 39: COLLINS-IDS SENSORS MOUNTED ON THE VERTICAL FIN OF THE AIRCRAFT [IMAGE COPYRIGHT EMBRAER/SENS4ICE PROJECT].	46
FIGURE 40: CLASSIFICATION BOUNDARIES FOR ALL THREE CONDITIONS. DRY CONDITIONS (GREEN), APP C CONDITIONS (BLUE), AND APP O (RED).	47
FIGURE 41: APP. C AND APP. O ENCOUNTERS DURING FLIGHT TEST. BOTTOM FIGURE IS GROUND TRUTH, TOP GRAPH IS COLLINS-IDS SENSOR AND DETECTOR OUTPUTS.	48
FIGURE 42: SENSOR PRINCIPLE (LEFT) AND SENSOR SETUP (RIGHT).	49
FIGURE 43: MOUNTING PRINCIPLE ON AIRCRAFT.	49
FIGURE 44: FLIGHT TEST SENSOR HARDWARE.	50
FIGURE 45: TRANSDUCER PLACEMENT ON TEST AIRCRAFT [AIRCRAFT IMAGE SAFIRE].	51
FIGURE 46: ICE FLAGS OF MICROPHYSICS (μ P) AND LILD WITH STATIC AIR TEMPERATURE.	52
FIGURE 47: SENSOR HEAD OF THE NEVZOROV PROBE.	53
FIGURE 48: SCATTERING CROSS SECTIONS FOR THE PARALLEL AND THE PERPENDICULAR COMPONENT OF THE BACKSCATTERED LIGHT FROM DROPLETS OF A GIVEN DIAMETER.	54
FIGURE 49: NEVZOROV PROBE AND BCPD INTEGRATED ON THE SAFIRE ATR-42 AIRCRAFT DURING THE EUROPEAN SENS4ICE CAMPAIGN [IMAGE DLR / SENS4ICE PROJECT].	55
FIGURE 50: CLOUD CONDITION DETECTED BY THE CM2D (BLUE) AND APP. O INDICATION FROM THE REFERENCE DATA (ORANGE).	56
FIGURE 51: FLUSH MOUNTED SENSOR OPTICAL DESIGN.	57
FIGURE 52: OPTICAL SENSOR DATA ANALYSIS: FLIGHT 1476. (NO COLLECTION EFFICIENCY CORRECTIONS APPLIED, SENSOR NON-LINEARITIES CORRECTIONS NOT APPLIED, BETTER RESULTS ARE EXPECTED)	59
FIGURE 53: OPTICAL SENSOR DATA ANALYSIS: FLIGHT 1481. (NO COLLECTION EFFICIENCY CORRECTIONS APPLIED, SENSOR NON-LINEARITIES CORRECTIONS NOT APPLIED, BETTER RESULTS ARE EXPECTED)	59
FIGURE 54: SENSOR ICE ACCRETION PROFILE PREDICTED BY THE SENSOR.	60
FIGURE 55: DWT COEFFICIENTS OF THE SIXTH, FIFTH AND FOURTH LEVELS.	61
FIGURE 56: INTA-FOD FLIGHT TEST DIRECT SENSING PROBE INSTALLED IN THE LEFT SIDE FUSELAGE OF THE AIRCRAFT [IMAGES INTA/ SENS4ICE PROJECT].	62
FIGURE 57: FOD MEASURED LWC COMPARED TO NEVZOROV.	62
FIGURE 58: PROBE DE-ICING (FLIGHT 27 APRIL 2023).	63
FIGURE 59: (A) DIAGRAM OF THE ELECTRICAL CHARGING OF A PARTICLE WHEN CROSSING ELECTRIC CHARGES CREATED BETWEEN TWO ELECTRODES (N AND G). (B) MEASUREMENT OF PARTICLE'S ELECTRIC CHARGE (Q) BY AN INDUCTIVE RING OF RADIUS a AND LENGTH L . THIS RING IS CONNECTED TO AN ELECTRONIC CIRCUIT THAT AMPLIFIES THE INDUCTIVE CURRENT.	64
FIGURE 60: GRAPH SHOWING MEASURED VS REQUIRED RESPONSE TIME FOR ALL TEST IN THE SENS4ICE MATRIX (8 POINTS). ALL THE POINTS BELOW THE BLACK DASHED LINE INDICATE A RESPONSE TIME THAT MET THE REQUIREMENTS.	66
FIGURE 61: GRAPH SHOWING MEASURED VS TUNNEL LWC (A) AND MVD (B) FOR THE TESTED POINTS CONCERNING SENS4ICE MATRIX AND ACADEMIC RUNS. ALL THE POINTS BELOW (ABOVE) THE BLACK DASHED LINE INDICATE A MEASURED LWC/MVD UNDERESTIMATING (OVERESTIMATING) THE CALIBRATED TUNNEL VALUES.	66
FIGURE 62: ILLUSTRATION OF THE AIRCRAFT CHARGING PROCESS DUE TO PARTICLE IMPACTS. (A) BEFORE IMPACTS AND (B) AFTER IMPACTS.	68
FIGURE 63: TIME HISTORY OF AIRCRAFT POTENTIAL (BLACK CURVE- UNITS: V) DEDUCED FROM AMPERA, AND TWC (GREY CURVE – UNITS: G.M ⁻³) FROM THE IKP2 PROBE. FIGURE TAKEN FROM REFERENCE [14].	68
FIGURE 64: ELECTROSTATIC SIMULATION ON THE SAFIRE ATR42 PLATFORM SHOWING THE DISTRIBUTION FOR THE NORMAL FIELD COEFFICIENTS V (UPPER), EX (LOWER LEFT), EY (LOWER CENTRE) AND EZ (LOWER RIGHT).	69
FIGURE 65: SAFIRE ATR42 AIRCRAFT DRAWING WITH INDICATION OF THE TWO RIGHT SIDE WINDOWS WHERE THE EFM ARE INSTALLED, EFM2 AND 4 (LEFT, IMAGE SAFIRE). PICTURE SHOWING THE TWO OTHERS MILLS, EFM1 AND 3, INSTALLED SYMMETRICALLY IN THE LEFT SIDE WINDOWS (RIGHT, IMAGE ONERA/ SENS4ICE PROJECT WITH SAFIRE PERMISSION).	70
FIGURE 66: AIRCRAFT ELECTROSTATIC POTENTIAL AND ALTITUDE FOR THE FLIGHT OF APRIL 3 RD 2023, SHOWING THE EXCELLENT SENSITIVITY OF THIS MEASUREMENT WHEN PASSING THROUGH CLOUDS.	70
FIGURE 67: LWC AND AIRCRAFT ELECTROSTATIC POTENTIAL COMPARISON (UPPER) AND AMPERA ATMOSPHERIC ICING FLAG AND ROSEMOUNT ICE ACCRETION FLAG (LOWER).	71
FIGURE 68: CAD OF THE AOD.	73
FIGURE 69: PICTURE OF A CUVETTE FILLED WITH 200 μ M DIAMETER BEADS GRABBED WITH THE LAB AOD.	73
FIGURE 70: DIAMETER MEASURED BY THE AOD.	73
FIGURE 71: RELATIVE ERROR ON THE MVD AND DMAX MEASURED WITH THE AOD	74





FIGURE 72: NUMBER OF BEADS DETECTED AS AN SLD LARGER THAN 100 μm WITH REGARD TO THE BEAD DIAMETER.	74
FIGURE 73: PFIDS WORKING PRINCIPLE.	76
FIGURE 74: TYPICAL PFIDS DETECTION CYCLE	76
FIGURE 75: INSTALLATION OF PFIDS ON PHENOM 300 [IMAGES EMBRAER/ SENS4ICE PROJECT].	77
FIGURE 76: EXAMPLE OF WATER CATCH SIMULATIONS RESULTS.	77
FIGURE 77: PFIDS DETECTION RESULTS FOR THE FLIGHT 1475-LEG 2 OF NORTH AMERICA FLIGHT TEST CAMPAIGN. IN THE FIRST SUBPLOT IS REPORTED THE MVD SIGNAL; IN THE SECOND SUBPLOT IS REPORTED THE LWC SIGNAL, IN BLACK, AND THE REFERENCE ICE FLAG REPRESENTED BY THE AREAS FILLED IN BLUE; THE THIRD SUBPLOT DISPLAYS PFIDS IAR MEASURE, IN BLACK, AND THE PFIDS ICE FLAG REPRESENTED BY THE AREAS FILLED IN GREEN.	78
FIGURE 78: PFIDS DETECTION RESULTS FOR THE FLIGHT 1476-LEG 1 OF NORTH AMERICA FLIGHT TEST CAMPAIGN. IN THE FIRST SUBPLOT IS REPORTED THE MVD SIGNAL; IN THE SECOND SUBPLOT IS REPORTED THE LWC SIGNAL, IN BLACK, AND THE REFERENCE ICE FLAG REPRESENTED BY THE AREAS FILLED IN BLUE; THE THIRD SUBPLOT DISPLAYS PFIDS IAR MEASURE, IN BLACK, AND THE PFIDS ICE FLAG REPRESENTED BY THE AREAS FILLED IN GREEN.	79
FIGURE 79: SENS4ICE HYBRID ICE DETECTION SYSTEM OVERVIEW (PICTURES CREDIT DLR / EMBRAER / SAFIRE).	80
FIGURE 80: SCHEMATIC REPRESENTATION OF HIDS ARBITRATION FUNCTION.	82
FIGURE 81: ATR HIDS, ON THE LEFT, AND HIDS-PC USER INTERFACE, ON THE RIGHT [IMAGES SAFRAN/ SENS4ICE PROJECT].	82
FIGURE 82: BASIC HIDS ARCHITECTURE FOR NORTH AMERICAN FLIGHT TESTS.	83
FIGURE 83: BASIC HIDS ARCHITECTURE FOR EUROPEAN FLIGHT TESTS.	84
FIGURE 84: EXPECTED ICING INFLUENCE ON AIRCRAFT AERODYNAMICS (LIFT AND DRAG COEFFICIENT); ADAPTED FROM [4].	85
FIGURE 85: BASIC PRINCIPLE OF THE IID METHOD BASED ON THE AIRCRAFT POWER IMBALANCE.	86
FIGURE 86: μ PHYSICS AND A/C DATA FOR FT1476-1. THE RED LINES REPRESENT THE CALCULATED AVERAGE VALUES OF EACH PARAMETERS DURING THE ICING ENCOUNTERS. SUCH VALUES ARE REPORTED IN TABLE 9....	88
FIGURE 87: ICE DETECTION SIGNAL OF DIDSS AND IID FOR THE ICING ENCOUNTERS OF FT1476-1. FROM THE BOTTOM TO THE TOP: μP , IID, PFIDS, SRP, IDS.	89
FIGURE 88: APP O DETECTION SIGNALS OF DIDSS FOR THE ICING ENCOUNTERS OF FT1476-1. FROM THE BOTTOM TO THE TOP: μP , SRP, IDS.	90
FIGURE 89: TIME HISTORY OF IID SYSTEM PERFORMANCE DURING SPECIFIC ICING ENCOUNTER FROM THE FIRST EXAMPLE FLIGHT (FEBRUARY 25 RD , 2023, 12:45:49 UTC TO 12:55:49 UTC): ALTITUDE AND INDICATED AIRSPEED (TOP), NOMINAL DRAG ESTIMATION AND IID DETECTION OUTPUT (SECOND PLOT), AND MVD AND LWC OF ENCOUNTERED ICING CONDITIONS (THIRD PLOT) INCLUDING THE INDICATION OF THE AMOUNT OF SLD (DASHED LINES), AND STATIC AIR TEMPERATURE AND AVERAGE ENGINE FAN SPEED (BOTTOM); DETECTION THRESHOLD AT 10% RELATIVE DRAG INCREASE; ADJUSTED ENGINE THRUST MODEL BEHAVIOUR.	91
FIGURE 90: ICE DETECTION SIGNAL OF DIDSS AND IID FOR IC3 OF FT1476-1. FROM THE BOTTOM TO THE TOP: μP , IID, PFIDS, SRP, IDS.	92
FIGURE 91: RESULTS OF HIDS ARBITRATION FOR THE COUPLE PFIDS/IID, ON THE LEFT, AND THE COUPLE SRP/IID, ON THE RIGHT. FROM THE TOP TO THE BOTTOM: LWC CURVE AND μP ICE FLAG; IID ICE FLAG; DID IAR OR LWC CURVE AND ICE FLAG; DID APP O FLAG (NOT AVAILABLE FOR PFIDS SINCE IT CANNOT DISCRIMINATE); HIDS ARBITRATION RESULTS; HIDS ARBITRATION STATUS.	93
FIGURE 92: RESULTS OF HIDS ARBITRATION FOR THE COUPLE IDS/IID. FROM THE TOP TO THE BOTTOM: LWC CURVE AND μP ICE FLAG; IID ICE FLAG; IDS ICE FLAG; IDS APP O FLAG; HIDS ARBITRATION RESULTS; HIDS ARBITRATION STATUS.	94
FIGURE 93: A/C DATA, μP DATA, REFERENCE ICING FLAGS AND IID OUTPUTS FOR THE FLIGHT AS230018. FROM THE TOP TO THE BOTTOM: A/C ALTITUDE TIME HISTORY AND IPS ACTIVATION; NEVZOROV MEASUREMENTS OF LWC AND TWC; TEMPERATURE TIME HISTORY (BOTH SAT AND TAT) AND RICE REFERENCE PROBE ICE FLAGS; μP ICE FLAGS; IID RELATIVE DRAG INCREASE AND ICE FLAGS.	95
FIGURE 94: ICE DETECTION SIGNAL OF DIDSS AND IID FOR THE ICING ENCOUNTERS OF FLIGHT AS230018. FROM THE TOP TO THE BOTTOM: RICE (REFERENCE), μP , IID, AMPERA, LILD, FOD.	96
FIGURE 95: TIME HISTORY OF IID SYSTEM PERFORMANCE DURING SPECIFIC ICING ENCOUNTER FROM THE FIRST EXAMPLE FLIGHT (APRIL 24 TH , 2023, 14:18:20 UTC TO 14:36:40 UTC): ALTITUDE AND INDICATED AIRSPEED (TOP), NOMINAL DRAG ESTIMATION AND IID DETECTION OUTPUT (SECOND PLOT), ICE BUILT-UP ON REFERENCE ACCRETION ICE SENSOR AND STATIC AIR TEMPERATURE (THIRD PLOT), AND MVD AND LWC OF ENCOUNTERED	





ICING CONDITIONS (SOLID LINE) INCLUDING THE INDICATION OF THE AMOUNT OF SLD (DASHED LINES) (BOTTOM); UPDATED DETECTION THRESHOLD AT 10% RELATIVE DRAG INCREASE.	97
FIGURE 96: EVOLUTION OF ICE ACCRETION ON THE AIRFRAME DURING ICING ENCOUNTER: CAMERA VIEWS ON LEFT & RIGHT WING AND HORIZONTAL TAIL FOR SPECIFIC MOMENTS DURING FLIGHT (INCREASED BRIGHTNESS AND CONTRAST); CORRESPONDING TO ENCOUNTER AND IID DETECTION OUTPUT GIVEN IN FIGURE 95; CREDIT SAFIRE/ SENS4ICE PROJECT.....	98
FIGURE 97: ON THE RIGHT, μP , A/C DATA AND REFERENCE ICE FLAGS DURING THE TIME INTERVAL [14:19:00 – 14:28:00] UTC OF FLIGHT AS230018. ON THE LEFT: DIDSS, IID AND REFERENCE ICE FLAGS DURING THE TIME INTERVAL [14:19:00 – 14:28:00] UTC OF FLIGHT AS230018.....	99
FIGURE 98: TIME HISTORY OF IID SYSTEM PERFORMANCE DURING SPECIFIC ICING ENCOUNTER FROM THE FIRST EXAMPLE FLIGHT (APRIL 24 TH , 2023, 14:42:29 UTC TO 15:02:39 UTC): ALTITUDE AND INDICATED AIRSPEED (TOP), NOMINAL DRAG ESTIMATION AND IID DETECTION OUTPUT (SECOND PLOT), ICE BUILT-UP ON REFERENCE ACCRETION ICE SENSOR AND STATIC AIR TEMPERATURE (THIRD PLOT), AND MVD AND LWC OF ENCOUNTERED ICING CONDITIONS (SOLID LINE) INCLUDING THE INDICATION OF THE AMOUNT OF SLD (DASHED LINES) (BOTTOM); UPDATED DETECTION THRESHOLD AT 10% RELATIVE DRAG INCREASE.	100
FIGURE 99: EVOLUTION OF ICE ACCRETION ON THE AIRFRAME DURING ICING ENCOUNTER: CAMERA VIEWS ON LEFT & RIGHT WING AND HORIZONTAL TAIL FOR SPECIFIC MOMENTS DURING FLIGHT (INCREASED BRIGHTNESS AND CONTRAST); CORRESPONDING TO ENCOUNTER AND IID DETECTION GIVEN IN FIGURE 98; CREDIT SAFIRE / SENS4ICE PROJECT.	101
FIGURE 100: ON THE RIGHT, μP , A/C DATA AND REFERENCE ICE FLAGS DURING THE TIME INTERVAL [14:42:00 – 15:01:00] UTC OF FLIGHT AS230018. ON THE LEFT: DIDSS, IID AND REFERENCE ICE FLAGS DURING THE TIME INTERVAL [14:42:00 – 15:01:00] UTC OF FLIGHT AS230018.....	102
FIGURE 101: RESULTS OF HIDS ARBITRATION FOR THE COUPLE AMPERA/IID. FROM THE TOP TO THE BOTTOM: TWC CURVE AND RICE ICE FLAG; AMEPRA TWC MEASUREMENTS AND ICE FLAGS; IID ICE FLAGS; HIDS ARBITRATION RESULTS; HIDS ARBITRATION STATUS.....	103
FIGURE 102: RESULTS OF HIDS ARBITRATION FOR THE COUPLE LILD/IID. FROM THE TOP TO THE BOTTOM: LWC CURVE AND RICE ICE FLAG; LILD IAR MEASUREMENTS AND ICE FLAGS; IID ICE FLAGS; HIDS ARBITRATION RESULTS; HIDS ARBITRATION STATUS.....	104
FIGURE 103: RESULTS OF HIDS ARBITRATION FOR THE COUPLE FOD/IID. FROM THE TOP TO THE BOTTOM: LWC CURVE AND RICE ICE FLAG; FOD IAR MEASUREMENTS AND ICE FLAGS; IID ICE FLAGS; HIDS ARBITRATION RESULTS; HIDS ARBITRATION STATUS.....	105
FIGURE 104: SCHEMATIC ACTIVATION AND MONITORING OF IPS PROVIDED BY HIDS.	108

LIST OF TABLES

TABLE 1: COMMON TEST POINTS BETWEEN IWT FACILITIES TUBS, COLLINS AND NRC.	16
TABLE 2: GROUPING BETWEEN SENSORS AND IWT FACILITIES AS WELL SUMMARY RESULT OF SENS4ICE EVALUATION.	17
TABLE 3: FLIGHTS OF THE NORTH AMERICAN SENS4ICE FLIGHT CAMPAIGN.	22
TABLE 4: FLIGHTS OF THE EUROPEAN FLIGHT TEST CAMPAIGN.	29
TABLE 5: SENS4ICE SENSOR TECHNOLOGIES OVERVIEW, SENSOR TYPES AND PRINCIPLES.	40
TABLE 6: CONFUSION MATRIX FOR COLLINS-IDS DETECTION AND DIFFERENTIATION ALGORITHM.	47
TABLE 7: FLIGHT TESTING OF CM2D COMPONENTS.	55
TABLE 8: RESULTS SUMMARY TABLE, INCLUDING THE STANDARD AND ACADEMIC TEST POINTS (AHDEL SENSOR)...	67
TABLE 9: CHARACTERISTICS OF IC1, IC2, IC3, IC4 AND IC 5 FOR FT1476-1.....	88
TABLE 10: NUMBER OF ICING ENCOUNTERS FOR FT 1475-1 AND NUMBER OF IC /APP. O FLAGS RAISED BY EACH DETECTOR. NOTE THAT IID AND PFIDS ARE NOT ABLE TO DISCRIMINATE BETWEEN APP. C AND APP. O ICING CONDITIONS.....	90
TABLE 11: IID AND DIDSS RESPONSE TIME FOR THE 5 APP O CONDITIONS OF FT 1476-1.....	92
TABLE 12: SUMMARY OF THE NUMBER OF IPS ACTIVATION, REFERENCE ICE FLAGS AND INDIRECT ICE DETECTION FOR THE FLIGHT AS230018.	95
TABLE 13: IID AND DIDSS RESPONSE TIME FOR THE ICING ENCOUNTER DURING THE TIME INTERVAL [14:19:00 – 14:28:00] UTC OF FLIGHT AS230018.....	99
TABLE 14: IID AND DIDSS RESPONSE TIME FOR THE ICING ENCOUNTER DURING THE TIME INTERVAL [14:42:00 – 15:01:00] UTC OF FLIGHT AS230018.....	102
TABLE 15: SENS4ICE TECHNOLOGY MATURATION PROGRESSION IN TERMS OF TRLs.	107





If not acknowledged otherwise, images courtesy of the SENS4ICE consortium partners.

This document reflects only the consortium's view. The European Commission and the European Climate, Infrastructure and Environment Executive Agency (CINEA) are not responsible for any use that may be made of the information it contains.

This document is one of the four final public deliverables for the EU-funded project SENS4ICE (Grant Agreement No 824253, 2019-2023):

D4.1 Sensor evaluation results and final roadmaps for future technology development and exploitation

D4.2 Final report on hybrid ice detection development

D4.3 Final report on airborne demonstration and atmospheric characterisation

D4.4 Final report on evaluation of technologies developed in SENS4ICE and technical project results





Executive summary

The EU-funded Horizon 2020 project SENS4ICE addresses reliable detection and discrimination of supercooled large droplets (SLD) icing conditions. These conditions are considered as particularly safety-relevant and have been included in airplane certification specifications. The SENS4ICE project comprised technology development, icing wind tunnel upgrading/testing and flight testing. The first part of the project was devoted to the development and maturation of icing detection technologies, with a focus on App. O (of 14 CFR Part 25 and CS-25) icing conditions. Ice wind tunnel testing (including App. O) of the developed sensing technologies concluded the first part of the project. The second part of the project was dedicated to flight testing of icing technologies in natural icing conditions including App. O.

This document summarises the final SENS4ICE results for novel SLD icing detection technologies. Considerable progress was made in developing, maturing and demonstrating direct, indirect and remote ice detection technologies particularly for SLD icing, including icing wind tunnel testing and flight campaigns in natural icing conditions. The demonstrated novel ice detection technologies facilitate broad and promising applications for many different air vehicle types and several applications including ensuring operational safety and supporting certification activities. The core outcome of the SENS4ICE project is a hybrid ice detection solution to tackle the challenging task of SLD detection. It is combining one or several direct ice detection technologies with the indirect approach to generate quick and robust warnings and continuous ice accretion and flight performance monitoring, also supporting efficiency optimization of ice protection systems. This hybrid ice detection was successfully tested and demonstrated in two flight test campaigns. The novel technologies successfully demonstrated in SENS4ICE may serve as a game changer to pave the way towards ensuring safety and certification for next generation air vehicles including greener aviation and revolutionary electrical or unmanned or urban air mobility vehicles.

Based on the SENS4ICE lessons learned and knowledge gained it is apparent that further data collection and analysis is imperative for a better physical understanding and further maturing of ice detection technologies to an operational level, including a clear path towards certification requirements. Safe aircraft operations in icing conditions are not related solely to atmospheric icing conditions but also to ice formation on airframe and furthermore very importantly to the degradation of flight characteristics. This changes for view on any certification path/ definition acceptable means of compliance particularly for new aircraft designs. A collaborative effort is needed involving all relevant stakeholders including industry, research, flight operations and aviation authorities.

1. Introduction

Modern commercial and business aircraft operate worldwide in all weather conditions, including atmospheric conditions in which ice may accumulate on the aircraft. This can adversely affect the aerodynamics, performance and controllability of an aircraft and has resulted in catastrophic accidents. Since 1964, the airworthiness regulations addressing icing conditions have been contained in Appendix C of the FAA and EASA certification specifications for "large aeroplanes". Ice detection systems were installed to inform pilots and ice protection systems have been integrated to prevent or remove ice accretion on critical areas, on e.g. wing leading edges or engine intakes. Ideally, ice detection systems should cover all relevant icing conditions where pilot action is potentially required.

At the end of the 20th century it became apparent that icing conditions with Supercooled Large Droplets (SLD), not covered by Appendix C, still presented a hazard to aviation. SLD ice is mainly similar to clear ice but, because of its large droplet size, it extends to unprotected parts of the aircraft and presumably forms larger ice shapes. Moreover, SLD-ice may accrete much faster than ice caused by more common smaller droplet conditions due to bigger drops with more water mass. As shown in Figure 1, if an SLD is large enough, its mass will prevent the pressure wave traveling ahead of an airfoil from deflecting it. These droplets will impinge further aft than a typical cloud-sized droplet, possibly beyond the protected area.



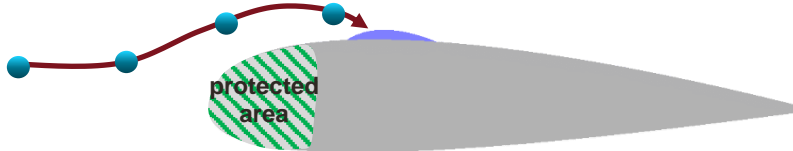


Figure 1: Impingement behind leading edge potentially affecting unprotected areas.

In 1994, SLD ice was a major factor in the accident of American Eagle Flight 4184 near Roselawn, Indiana [5]. This accident triggered investigation of authorities, industry and scientists into the effects of SLD exposure on aircraft and has led to the expansion of the airworthiness regulations (CS-25 [11] / 14 CFR Part 25 (formerly known as FAR 25) [12]) with Appendix O covering SLD icing conditions. App. O stipulates that an aircraft can safely exit icing conditions (including SLD) before ice accretion leads to accidents through a mixture of detection and protection systems. Up until now, no ice detection system exists which can reliably detect App. O conditions, inform pilots, trigger protection measures and consequently ensure timely and safe exiting. Until SENS4ICE, existing detection and protection technology is mostly insufficient to reliably and adequately address App. O SLD conditions.

Although these conditions are rare, due to the projected continuing growth of aviation in the next decades the number of SLD encounters will grow as well. With the objective of maintaining and improving the high aviation safety standards, action is needed. The EU-funded Horizon 2020 project SENS4ICE [13], [14] addressed this challenge [15] by researching a unique layered safety approach (see Figure 2) of:

- Supporting improved ice condition predictions before entering an area by providing data to enhance forecasting methods and a “nowcasting” based on satellite data and potentially also data from other aircraft that have flown in the same area. A better understanding of atmospheric conditions leading to SLD directly supports development of better prediction models. This assists in both timely avoidance of true icing threats and the prevention of unnecessary exits due to the false identification of an icing threat.
- A robust and hybrid ice detection system based on a range of sensors with different physical principles to reliably detect all icing conditions during both entry and flight through such an area. Besides direct measurement of atmospheric properties and ice accretion, indirect detection of ice accretion through changes of the aircraft characteristics was investigated. Doing so, pilots obtain a better situational awareness and ice protection systems could be activated only if a true icing hazard exists, reducing the overall energy consumption and emissions to ensure a greener aviation.
- Hybridisation: Various technologies and physical principles can be used to detect icing conditions, ice accretion, or the impact of the ice accretion on the aircraft behaviour. The hybrid system combines several individual technologies with the aim of providing a more robust and reliable system by combining their advantages and compensating for individual sensor limitations. Further details on these individual technologies and their hybridisation can be found below.
- Prevention of icing-induced loss of control events as a contingency to safely exit icing conditions. Complementary to the increased situational awareness on icing conditions, the new detection of the reduction in aircraft flight envelope provides the necessary information to alert the crew on the remaining aircraft capabilities if ice forms on the airframe.

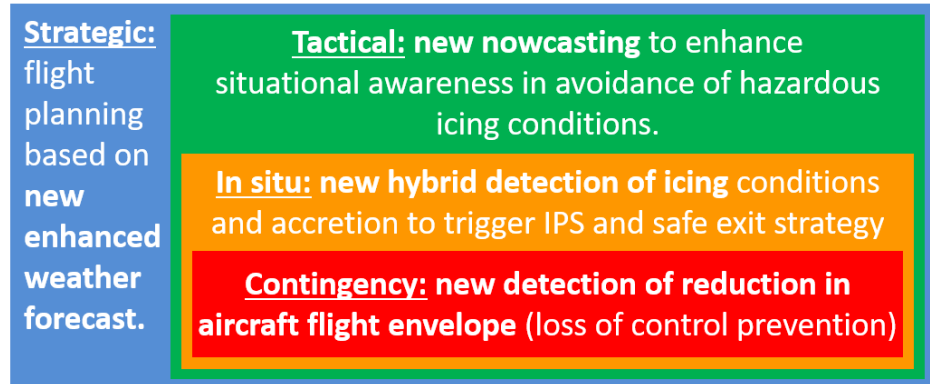


Figure 2: SENS4ICE layered safety concept for liquid water icing.

The consortium united European and international aircraft manufacturers, equipment suppliers and research/academia with a large variety of technologies that have emerged in recent years [16], the most promising and mature of which were selected for flight testing, while several other less mature but promising technologies were advanced in laboratory environment [17]. Since icing is a global hazard, SENS4ICE addressed this challenge with a global consortium including participants from Brazil, USA, and Canada (DLR, ATR, CIRA, CNRS/Safire, Embraer, Honeywell, INTA, Leonardo, L-up, ONERA, TUBS, Collins, SAFRAN, NRC). By aligning the EU-funded activity with nationally and privately funded programmes of those countries, a new direction for a harmonised global view on Acceptable Means of Compliance was shown, and technological progress was further advanced by ensuring complementarity and avoiding overlap.

2. SLD Ice Wind Tunnel Testing

The first project phase was mostly devoted to the development and maturation of icing detection technologies, with a focus on Appendix O conditions. The aim was to enhance icing wind tunnel (IWT) SLD capabilities and to test direct sensor technologies in IWT in order to perform a technology evaluation.

In order to test the direct sensors three IWT test facilities were involved:

- Collins Aerospace Icing Wind Tunnel,
- TUBS Braunschweig Icing Wind Tunnel (BIWT) [18],
- National Research Council (NRC): Altitude Icing Wind Tunnel (AIWT) [19].

While the NRC AIWT already provided the capability to achieve SLD in full bimodal freezing drizzle conditions, the other two icing wind tunnel facilities improved their capabilities to represent App. O conditions in the scope of the SENS4ICE project. These improvements mainly included adapting the spray nozzle setup and were aiming at freezing drizzle conditions, while testing freezing rain conditions was out of the scope for the SENS4ICE project.

The extension of the wind tunnel capabilities towards the Appendix O icing regime was accompanied by the effort to precisely characterize the generated droplet sprays. However, as of now, no standardized procedure for the measurement of Appendix O conditions exists, hence wind tunnel operators utilise a wide range of different instruments. This raised the question, to what extent the results of SENS4ICE sensors that measured in different wind tunnels are comparable. To ensure comparability between results obtained in the different IWTs, reference measurements with a common set of established airborne instruments were conducted in the three IWTs. Reference measurements of LWC were conducted in the three IWTs with a Nevzorov probe, which had been modified with a second total water content collector cone (with an increased diameter of 12 mm alongside the standard 8 mm cone). This has been found to be generally suitable for the collection of SLD [20]. In addition, at Collins and at the BIWT, a Cloud Combination Probe (CCP) was used for IWT reference measurements.

Dedicated reference measurement results are compared with specifications and IWT data for specific test points. Icing wind tunnel conditions and comparison are deemed fully sufficient for SENS4ICE project purposes of testing icing sensors as part of the sensor technology development and maturation process. From the icing wind tunnel perspective it is concluded that further collaborative efforts are needed for product development





and certification in standardised SLD conditions. International exchange and collaboration will be particularly useful to achieve this goal.

A standardized testing procedure and partly common test points between the different icing wind tunnels serve for adequate comparability of the results. Significant emphasis was put on the development of test matrices for each involved IWT facility following the guidelines of ED-103 [27]. As the setup and capabilities of each IWT facility vary, icing envelopes differ from one IWT facility to another with very limited overlap. This effect was leveraged by establishing a common test procedure and by selecting common test points between all or some of the facilities (Table 1). Test matrices for each IWT define details of the test points. Such details include air speed, MVD, LWC, required response time as per ED-103, and other relevant parameters. Test for different sensors and different test points were standardised to ensure comparability: 1) start data recording, 2) record data for 1 min in clean air, 3) start the icing cloud, 4) once an icing signal is detected, run for 1 min, 5) stop the icing cloud [28]. For a selected subset of the test points, 3 cycles of icing have been completed (to test repeatability to the extent possible with the available IWT time). In order to test sensor ability to maintain its functionality over an extended period, one Appendix C test point was selected for endurance. This test point was tested with the icing cloud turned on for a duration of 45 minutes.

Table 1: Common test points between IWT facilities TUBS, Collins and NRC.

IWT	App	C					App	O				
	Total Test Points	Common with 3 IWT	Common with 2 IWT	Only at 1 IWT	CM Test Points	IM Test Points	Total Test Points	Common with 3 IWT	Common with 2 IWT	Only at 1 IWT	Total Points [unimodal]	Total Points [bimodal]
TUBS	19	4	1	14	10	9	18	0	1	17	0	18
Collins	18	4	4	10	9	9	6	0	1	5	6	0
NRC	19	4	4	11	9	10	17	0	2	15	4	13

Apart from the reference instruments, eight technologies have provided testing results in different icing wind tunnels in App. C and O conditions. Due to the fact that the sensor technology AMPERA (ONERA) uses the aircraft as a sensor (measurement of aircraft electric potential), IWT testing is not feasible. Instead, flight test data from previous projects were assessed to investigate the correlation between the electrostatic field and the total water content [29]. IWT results were used towards sensor technology evaluation and down-selection with the support of the project Advisory Board. Table 2 gives a summary of the different technologies with respect to each IWT facility used and result of the SENS4ICE evaluation. For more information about SENS4ICE direct ice detection technologies see section 5 and [6].



Table 2: Grouping between sensors and IWT facilities as well summary result of SENS4ICE evaluation.

Sensor / Developer	Sensor Type	IWT Facility Used	Outcome of Evaluation supported by Advisory Board
AIP / AeroTex	Atmospheric	NRC	Pass
IDS / Collins	Atmospheric	Collins and NRC	Pass
LILD / DLR	Accretion	TUBS	Pass
SRP / Honeywell	Atmospheric	Collins and NRC	Pass
FOD / INTA	Accretion	NRC	Pass
AHDEL / ONERA	Atmospheric	TUBS	Stop developments with SENS4ICE
AMPERA / ONERA	Atmospheric	N/A	Pass
AOD / Safran	Atmospheric	Withdrawn	Stop developments with SENS4ICE
PFIDS / Safran	Accretion	TUBS	Pass
CM2D [BCPD] / DLR	Atmospheric	TUBS	Pass
CM2D [Nevzorov] /DLR	Atmospheric	TUBS	Pass

Sensor technologies performed generally very well in IWT tests and several sensors have correctly detected 100% of the test points for App. C and also for App. O, also within the required maximum response time as per ED-103. An overview of the detection rates (test cases successfully detected related to the total number of test cases) is shown in Figure 3, excluding DLR's CM2D scientific/reference sensor and SAFRAN's AOD that was withdrawn from IWT testing in the context of Covid-19 related delays.

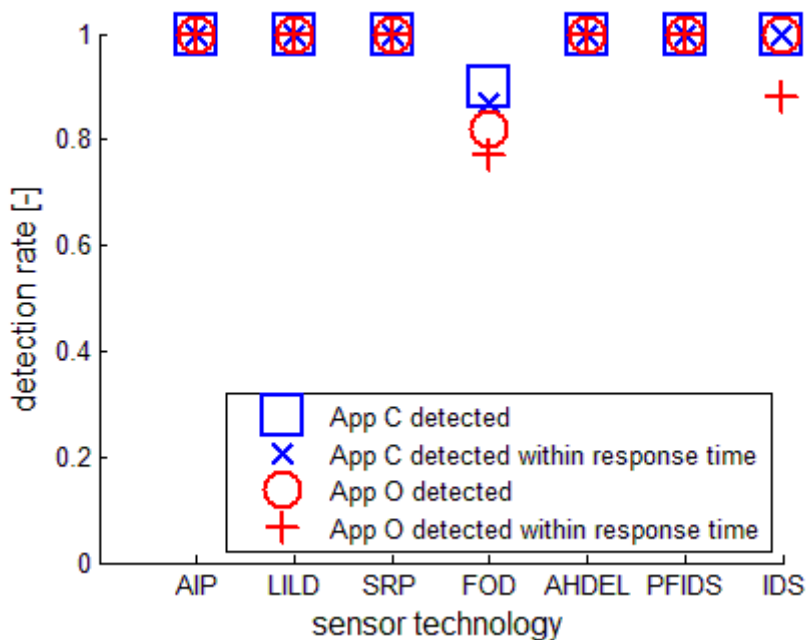


Figure 3: SENS4ICE sensor detection rates overview for App. C and O icing condition IWT test points for seven detection technologies.

A qualitative overview (anonymised) of measured sensor response times compared to required response times as per ED-103 is shown in Figure 4 (top) for App. C icing condition test points. In almost all cases the response times for the detection technologies are within the requirements. Measured sensor response times compared to required response times for detecting liquid water icing conditions for App. O IWT test points are shown in Figure 4 (bottom).

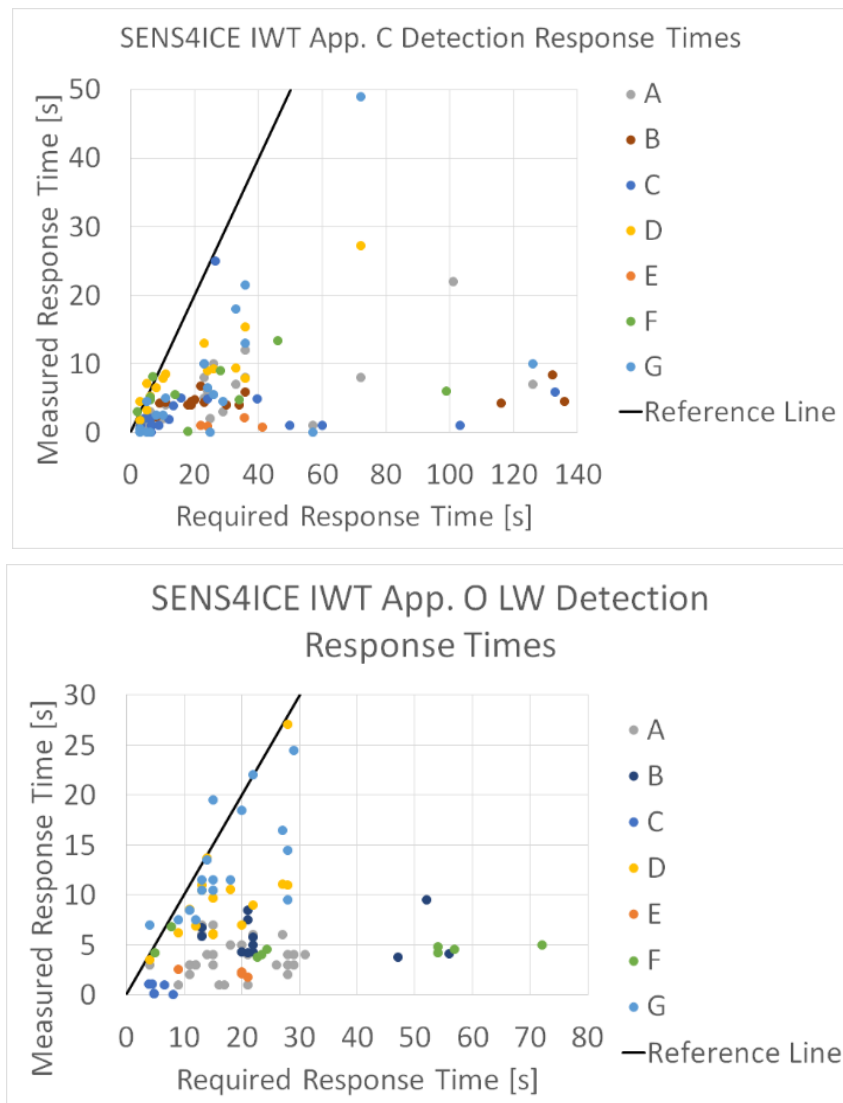


Figure 4: Measured sensor response times compared to required response times for App. C IWT test points (top) Measured sensor response times compared to required response times for detecting liquid water (LW) icing conditions for App. O IWT test points (bottom).

Measured sensor response times compared to required response times for differentiating App. C conditions from App. O conditions are shown in Figure 5. Note that not all sensor technologies have provided differentiation information for the IWT tests.

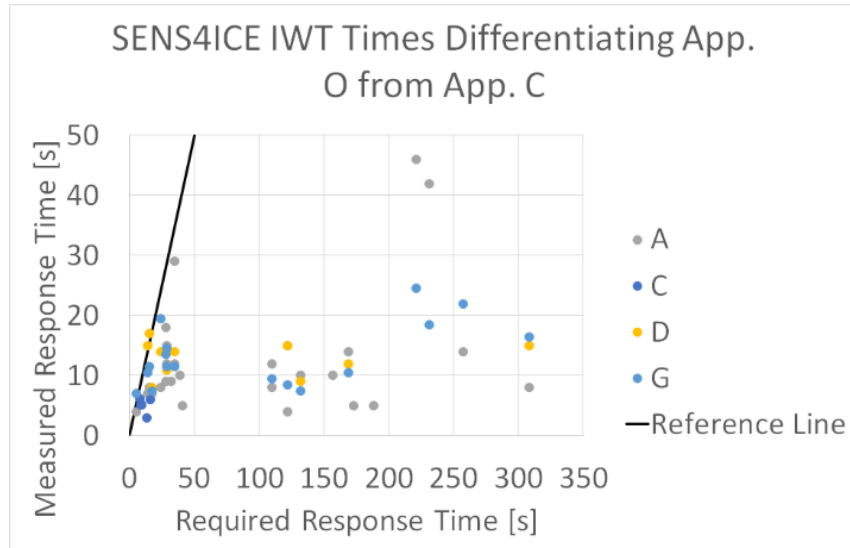


Figure 5: Measured sensor response times compared to required response times for differentiating App. C conditions from App. O conditions in IWT (for sensors providing differentiation information).

SENS4ICE sensor IWT testing provided valuable results for the sensor technology development and revealed that the technologies under development can be considered as promising. Furthermore, IWT test results established a profound basis for the project internal technology evaluation and selection process.

The primary goal of the SENS4ICE project is to develop a hybrid system for detecting liquid water icing including Appendix C and particularly Appendix O conditions. While the development of direct detection sensors is considered critical for this effort, the development of sensors for stand-alone applications is considered an important secondary goal.

Technology evaluation was greatly supported by the SENS4ICE Advisory Board composed of aviation certification authorities, aircraft manufacturers, pilot representatives and research institutions. A multi-stage evaluation process with dedicated technology evaluation criteria was developed [17], and additionally general comments including highlighting strengths and weaknesses have been received and perceived as very valuable for further technology development. No sensor technology received a very low overall Advisory Board rating. All sensor technologies have made substantial progress and are considered promising by the Advisory Board. As two sensors (AHDEL/ ONERA and AOD/ Safran) were withdrawn from flight testing due to low maturity, it was decided to select all other sensors for flight testing [17].

3. SLD Icing Flight Test Campaigns and Atmosphere Characterisation

This section gives an overview of the flights performed and the microphysical properties of the clouds encountered during the two airborne campaigns within the SENS4ICE project. The first SENS4ICE flight campaign took place between February 23 and March 10, 2023, based out of Alton, Illinois, USA. The second flight campaign took place between April 3 and April 27, 2023, based out of Toulouse, France. The campaigns are therefore referred to as the North American and the European flight test campaign, respectively [26].

This section first describes the measurement platforms and the reference instrumentation that were used to characterize the atmospheric conditions during the campaigns. Subsequently, the evaluation strategy of the instruments is explained. Thereafter, the campaign flights are briefly summarized and an overview of the icing conditions that were encountered is given.

Prior to the campaigns, different models and satellite observations on icing occurrence above Europe and North America were analysed to find the best region with the highest occurrence rate of icing in general and

SLD in particular, given the different safety constraints on the flight manoeuvres. The overview and conclusions of the analysis are summarized in [21].

The reference instruments for the characterization of microphysical properties of the clouds encountered were of highest importance for both flight campaigns. The American flight test campaign used an Embraer Phenom 300 aircraft as the measurement platform (see Figure 6). The Phenom carried a Cloud Combination Probe (CCP) [22],[23],[24], owned by Embraer and manufactured by Droplet Measurement Technologies for the measurement of particle size distributions. For the measurement of liquid water content (LWC) and total water content (TWC), the Phenom 300 also carried a SEA ice crystal detector (ICD) manufactured and operated by Science Engineering Associates (SEA) [25].



Figure 6: North American flight campaign Embraer Phenom 300 aircraft [copyright Embraer/ SENS4ICE project].

For the European flight campaign, an ATR 42 aircraft of the French facility for airborne research (SAFIRE) was used (see Figure 7). Figure 8 shows an example of ice accretion on the wing of the Embraer Phenom 300 and Figure 9 likewise for the SAFIRE ATR 42 horizontal tail with ice accretion. A large suite of reference instruments was installed on the plane, for more details see SENS4ICE deliverable D4.3 [8]. To maintain consistency with the American flight test campaign data, only measurements of the CCP and the Nevzorov probe were used for the European campaign data. In the future, more detailed microphysical analyses and instrument comparisons will also take into account the data from the other instruments.



Figure 7: European flight campaign SAFIRE ATR 42 environmental research aircraft [image DLR/ SENS4ICE project with SAFIRE permission].



Figure 8: Embraer Phenom 300 with ice accretion on wing [copyright Embraer].



Figure 9: SAFIRE ATR 42 horizontal tail with ice accretion [image DLR/ SENS4ICE project with SAFIRE permission].

The reference measurements of both campaigns can be grouped into particle size measurements and bulk LWC and TWC measurements. Particular processes were applied to derive reliable reference measurement results. Details of the evaluation steps necessary for both types of instruments are described in SENS4ICE deliverable D4.3 [8].

3.1. Flight Campaign North America

This subsection details the flights of the American flight test campaigns. In the campaign, four of the icing detection technologies under development in the SENS4ICE project were tested: AIP / AeroTex, IDS / Collins, SRP / Honeywell and PFIDS / Safran. 15 flights with a total of 25 flight hours (including ferry and check flights) were successfully conducted allowing to target natural liquid water icing conditions and in particular SLD conditions (Figure 10). Nine measurement flights were performed as part of the North American flight test campaign, which are listed in Table 3. A total of 4 hours and 23 minutes were spent in icing conditions, 50 minutes of which were in Appendix O icing conditions, based on the definitions in SENS4ICE deliverable D4.3. A detailed meteorological analysis of selected flights is available in [30].

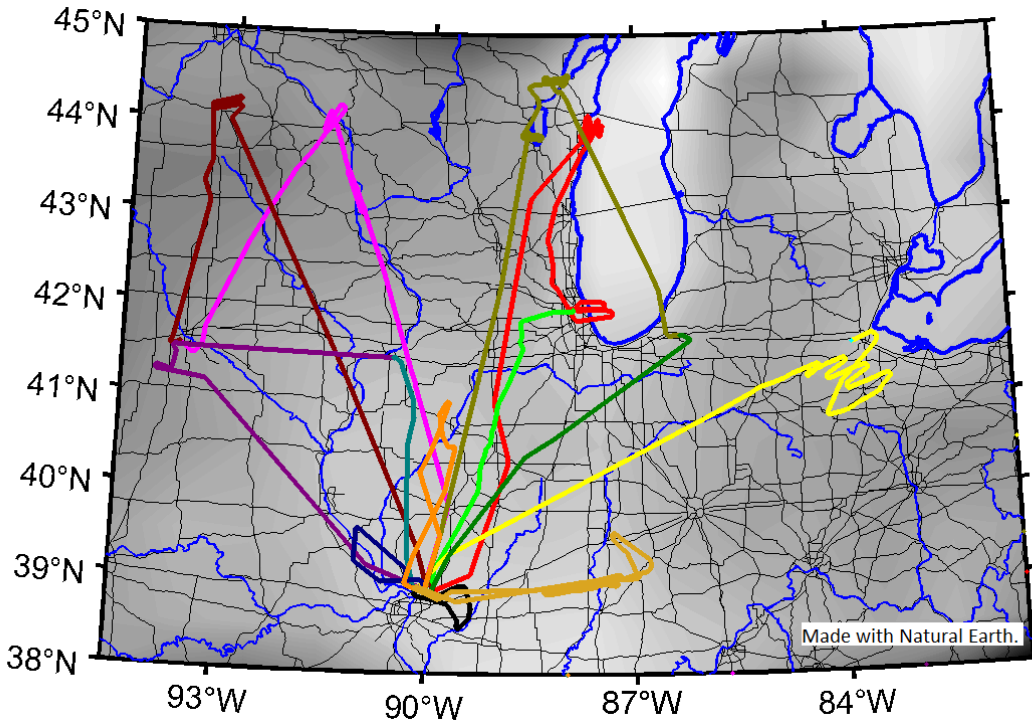


Figure 10: Ground tracks of the North American SENS4ICE campaign in February/March 2023 [credit DLR/SENS4ICE project made with Natural Earth].

Table 3: Flights of the North American SENS4ICE flight campaign.

Flight	Day	Flight time UTC	Time in Icing conditions [mm:ss]	Time in Appendix O conditions [mm:ss]
F1475-1	23/02/2023	11:43-14:29	20:18	9:03
F1475-2	23/02/2023	17:18-18:33	19:59	0:00
F1476	25/02/2023	11:38-13:43	38:47	22:24
F1477-1	01/03/2023	11:38-13:48	31:03	3:55
F1477-2	01/03/2023	16:56-18:34	14:30	7:31
F1478	06/03/2023	11:46-14:18	43:24	4:03
F1479	08/03/2023	Instrument failure	-	-
F1481	09/03/2023	12:01-13:13	15:51	2:46
F1482	10/03/2023	12:08-17:40	79:59	0:00

The following part of this section summarizes observations on the atmospheric parameters observed during the North American flight test campaign based on the full flight data set. Figure 11 shows a histogram of the LWCs encountered in Appendix C (left) and O (right) conditions in all flights. Appendix C conditions being defined as data points where the icing flag equals one but the Appendix O flag equals zero (for details see SENS4ICE deliverable D4.3 [8]). The LWC of Appendix C encounters is relatively equally distributed between 0 and 0.8 g/m³. The LWC is below 0.77 g/m³ in 90% of the cases. The values plotted for Appendix O conditions are technically TWC values, but because Appendix O conditions were only detected in the presence of very few or no ice crystals, LWC and TWC are assumed to be equivalent (see D4.3 for details). The majority of TWCs fall between 0.2 and 0.5 g/m³, with 10% of TWCs exceeding 0.65 g/m³. It should be noticed, that these LWCs and TWCs are based on 15s rolling averages, which were not averaged over a specific exposure distance, as is the case in [31]. Of relevance for Appendix O conditions is especially the LWC that is contained in SLD, as it causes the critical ice accretion. Therefore, Figure 12 shows a histogram of the LWC that was

contained in SLD during the North American flight test campaign. In the majority of cases, the LWC contained in SLDs is below 0.05 g/m^3 . But isolated cases exist, where SLD LWCs were larger than 0.075 g/m^3 . These measurements stem mostly from flights F1475-1 and F1481.

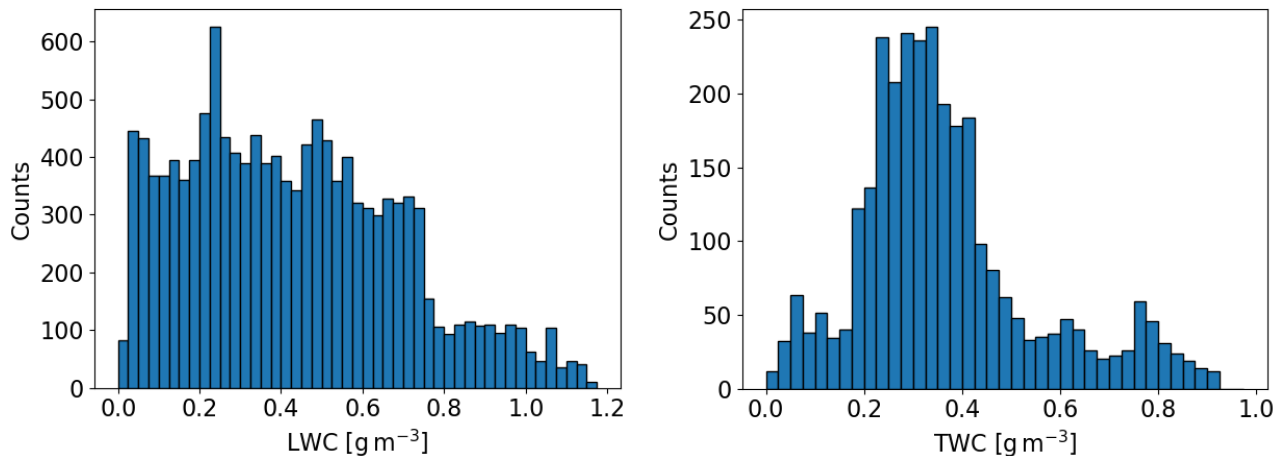


Figure 11: Distribution of ICD LWC measurements in Appendix C conditions (left) and ICD TWC measurements in Appendix O conditions (right) for North America flight campaign. The counts are based on 15 second rolling averages which were computed for each second. Because Appendix O conditions are only defined if very few ice crystals are present, the TWC is assumed to be equivalent to the LWC in these cases.

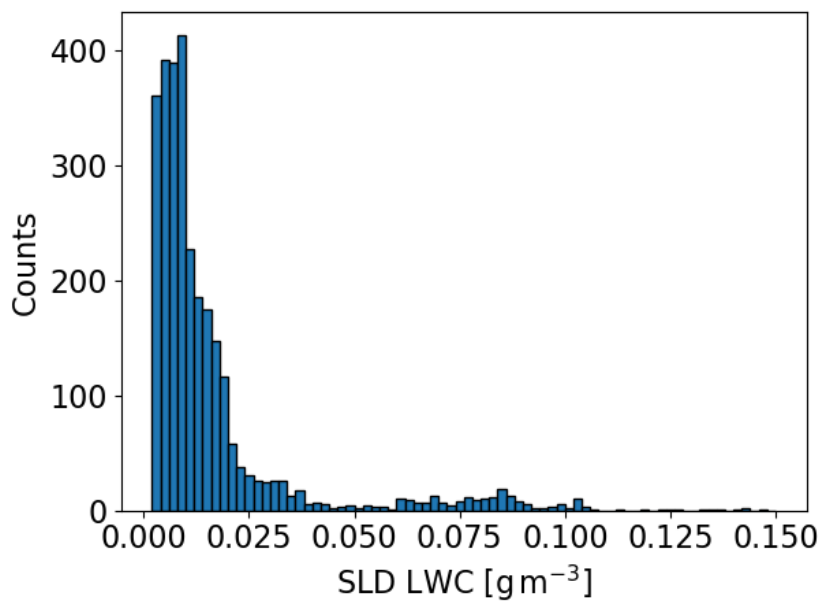


Figure 12: LWC contained in SLDs (i.e. all droplets with diameters larger than $100 \mu\text{m}$) during the North American flight campaign. The data are based on 15 second rolling averages.

Figure 13 provides a map of the LWC measurements along the flight track as observed during the North American flight test campaign. Blueish to black colours denote enhanced LWC while white shading symbolizes cloud free air. The grey colours give flight segments without any data (e.g. transfer flights).

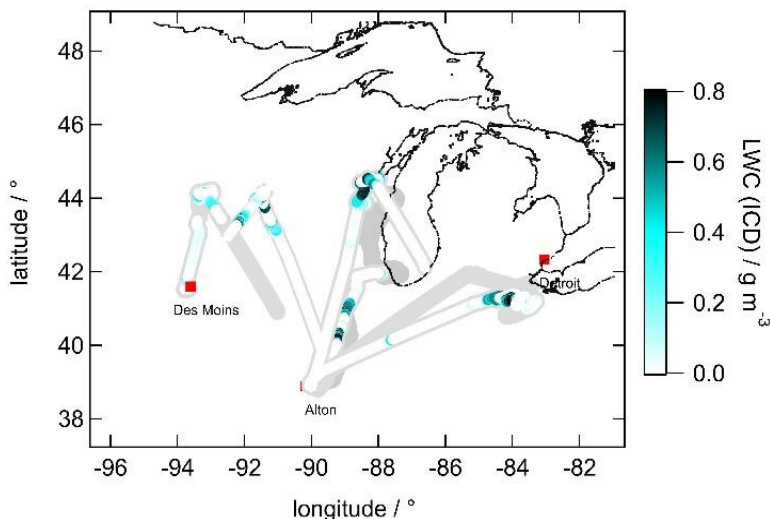


Figure 13: Map of selected flight paths from the North American campaign colour coded with the LWC measured by the ICD. Enhanced LWD shows region of icing encounters. Only flights F1475-1, F1475-2, F1476, F1477-1, F1477-2 are included in the plot. [21].

The time spent in Appendix C and Appendix O conditions for all flight data is provided in an altitude profile in Figure 14. The LWC data for this analysis are based on 15 second averages, i.e. they are not directly comparable to the data used for the Appendix O certification envelopes described by Cober and Isaac [31]. Icing conditions during the North American campaign were mostly encountered between 500 and 3000 m, with a maximum around 1500 m. Appendix O conditions were encountered much less often, of course and they were found between 1000 and 3000 m. Altitudes above 3000 m were mostly used for transfer and to deice. Therefore, the number of icing encounters is very small at higher altitudes. The mean LWC values of Appendix C and Appendix O conditions are mostly between 0.2 and 0.5 g/m³. For colder temperatures, the mean LWC decreases for both Appendix C and Appendix O conditions up to -14°C, below which no Appendix O conditions

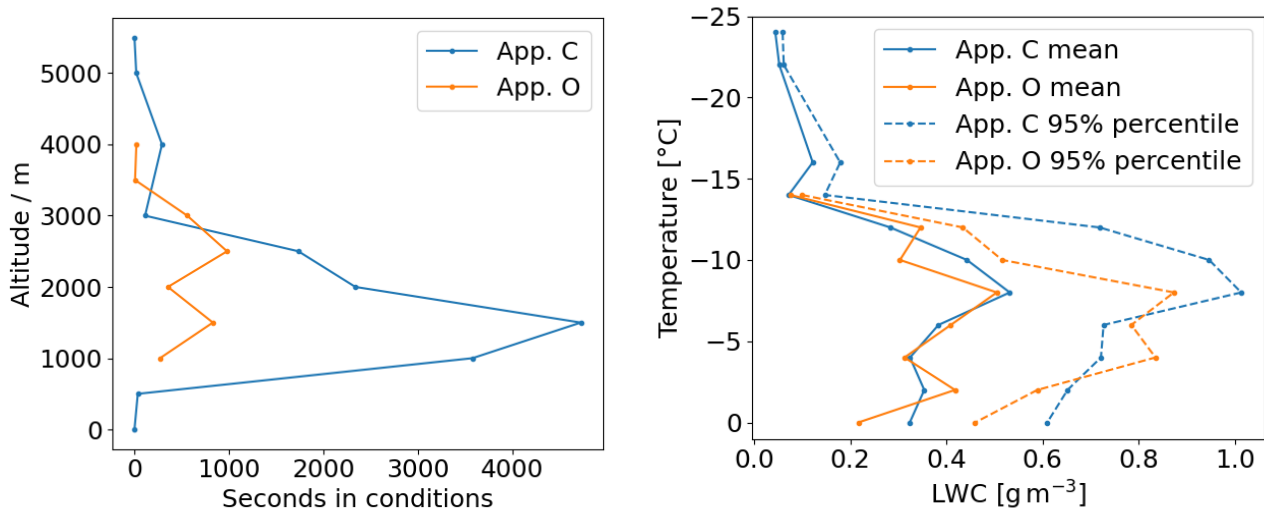


Figure 14: Altitude (left) and temperature (right) profile of the all icing encounters of the North American test campaign divided in App. C and App. O conditions as defined above. Shown are mean and 95 percentiles of the LWC contained in Appendix C and Appendix O classified clouds. LWC data are based on 15 second averages.

were encountered and also App. C conditions have only minimal LWCs. The 95 percentiles of the App. O LWC

peaks around values of 0.8 g/m^3 for temperatures between -4 and -8°C . Appendix C conditions reach significantly higher LWCs, which can exceed 1 g/m^3 .

The cumulative mass distributions of the SLD conditions that were encountered are shown in Figure 15. All but one of these distributions have more than 80% of LWC at diameters smaller than $100 \mu\text{m}$. Median volume diameters were on average at $23 \mu\text{m}$. Thus, mostly freezing drizzle conditions with $\text{MVD} < 40 \mu\text{m}$ were sampled. Freezing rain conditions were not targeted and not encountered.

Due to sampling strategies designed to maximize safety, it was necessary to conduct most of the Appendix O sampling near cloud top, where the small drop contribution to Appendix O clouds tends to be quite significant, frequently resulting in $\text{MVD} < 40 \mu\text{m}$. Appendix O clouds with $\text{MVD} > 40 \mu\text{m}$ tend to occur well below cloud top, often near or below cloud base, where the small drop contribution to the drop size spectrum is much smaller and drizzle has grown to larger sizes through collision coalescence

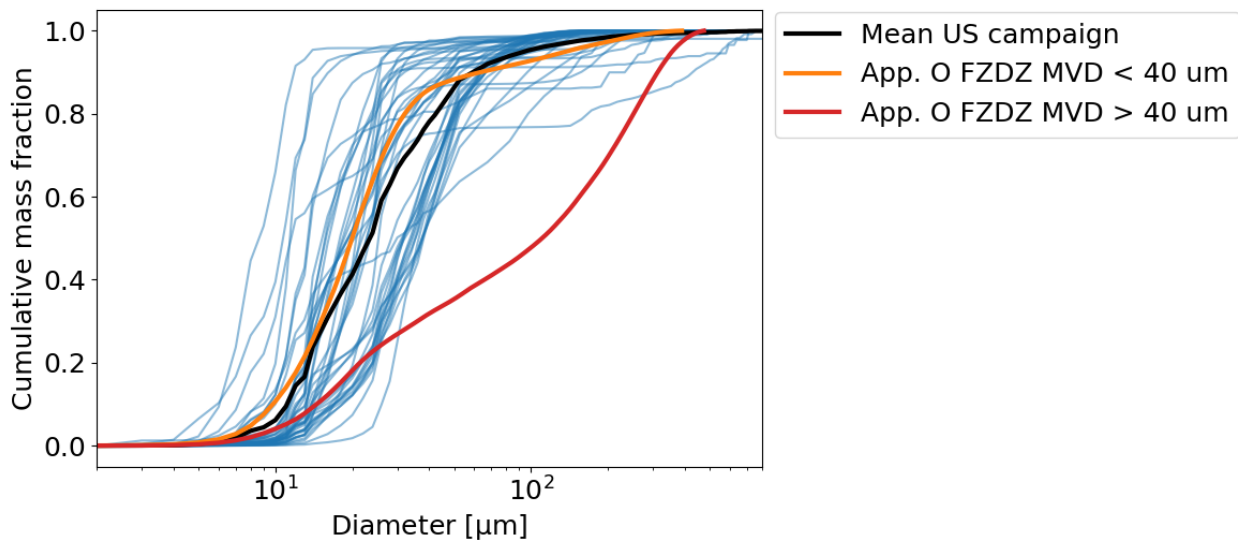


Figure 15: Cumulative mass distributions for each Appendix O encounter observed during the North American flight test campaign. MVDs were on average $23 \mu\text{m}$. The cumulative mass curves for freezing drizzle $\text{MVD} < 40 \mu\text{m}$ and $\text{MVD} > 40 \mu\text{m}$ from Cober and Isaac [31] are plotted in orange and red, respectively.

In Figure 11 (right) the TWC encountered in Appendix O conditions (which is assumed to be equivalent to the LWC, due to the criterion that an Appendix O encounter contains at most one ice crystal per liter) was plotted as a histogram. It is apparent that occasionally TWC values occur which exceed the maximum specified in the Appendix O envelopes [31]. However, it needs to be considered that the values that were used to create the envelopes were averages over 17.4 nautical miles. According to Cober and Isaac [31], if data with different encounter lengths are considered, a scaling factor needs to be applied to the LWC. For instance, the average LWC measured during an encounter with a horizontal extent of 3000 m needs to be multiplied by 0.82 before it is compared to the LWC envelopes of Appendix O. This scaling reflects the decreasing probability to encounter high LWC over long distances. The comparison of the LWC of the Appendix O encounters of the American SENS4ICE campaign and the certification envelopes can be seen in Figure 16. The appropriate scaling factors were applied to all encounters. Most of the encounters fall within the envelopes and, as mentioned earlier, there are no measurements in the portion of Appendix O which is at temperatures lower than -15°C . Two points clearly fall outside the envelope of FZDZ $\text{MVD} < 40 \mu\text{m}$, despite the scaling factor that has been applied. Also, of the just two encounters with $\text{MVDs} > 40 \mu\text{m}$, one falls outside the envelope. The highest LWC for Freezing Drizzle $\text{MVD} < 40 \mu\text{m}$ occurred during Flight 1477-1, it is the same encounter that was already pictured in Figure 16. The meteorological conditions of this encounter would be a suitable subject for further study in order to assess the likelihood that the LWC exceeds the envelope limits. The highest LWC in the FZDZ $\text{MVD} > 40 \mu\text{m}$ regime occurred during Flight 1481. The temperature during the encounter was relatively high and it did not result in ice accretion.

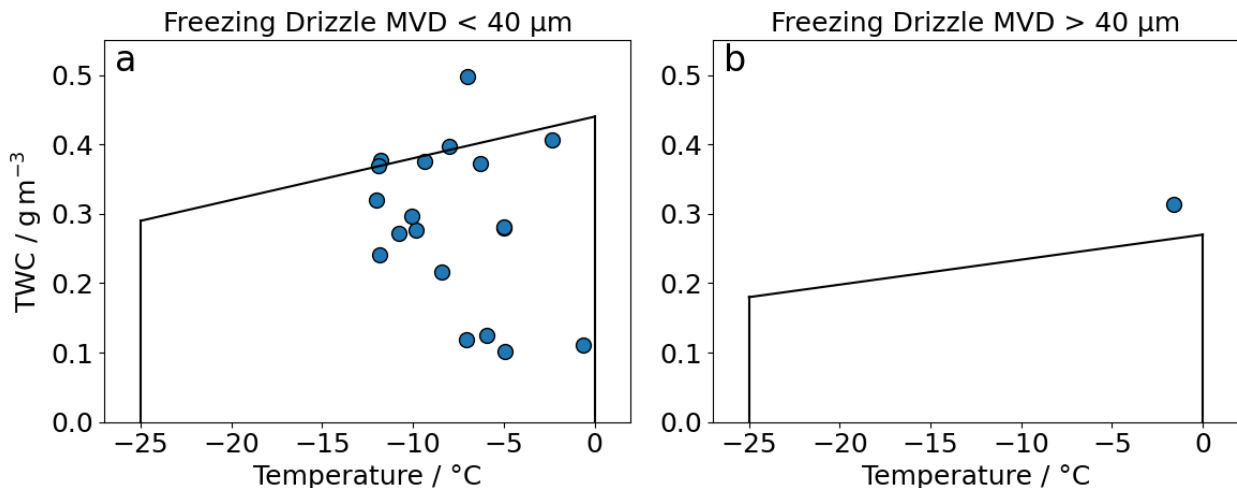


Figure 16: Nevezorov TWC of the Appendix O encounters during the North American SENS4ICE campaign in comparison to the LWC envelopes of Freezing Drizzle MVD < 40 μm (a) and Freezing Drizzle MVD > 40 μm (b). The Nevezorov TWC is assumed to be equivalent to the LWC in Appendix O conditions because Appendix O encounters were required to contain few ice crystals. Due to ambiguities that may exist in the detection of particles (see D4.3) and due to the chance of intermittent mixed-phase pockets the TWC measurement of the Nevezorov may be contaminated by ice and thus too high for some of the encounters shown. Only encounters longer than 30 seconds were used for this plot.

Appendix O also defines a temperature and altitude envelope in which freezing drizzle conditions occur. This is shown, in comparison to the data from the North American SENS4ICE campaign, in Figure 17. All test points lie well within the envelope. Regarding altitude and temperature, the Appendix O conditions were therefore normal.

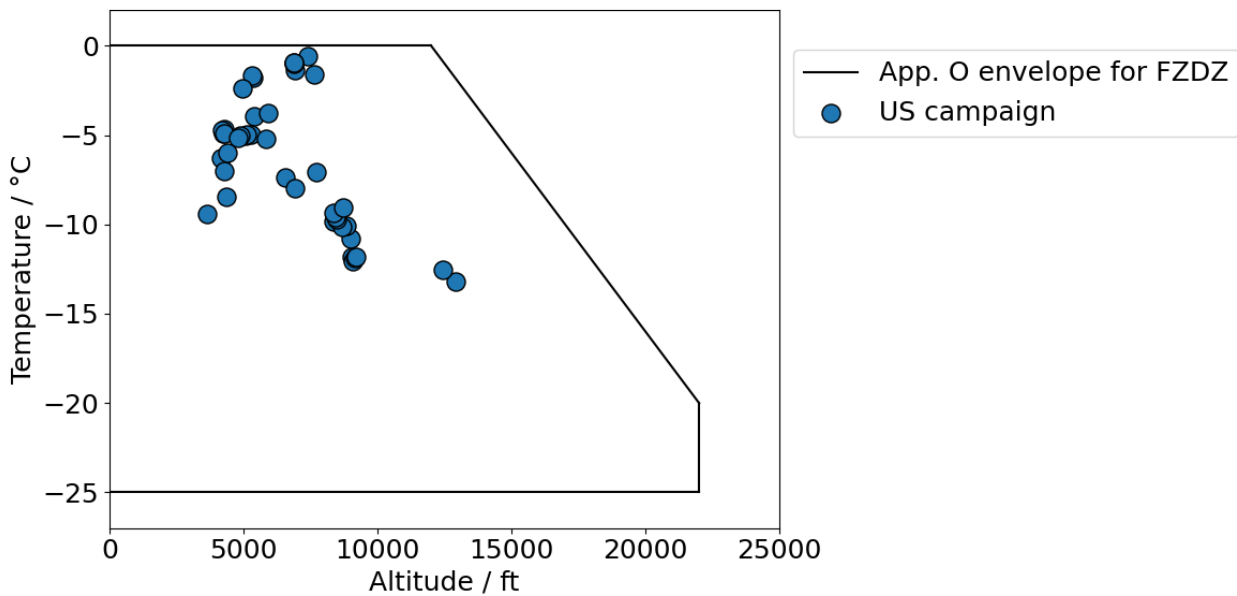


Figure 17 Pressure and altitude of Appendix O conditions encountered during the North American SENS4ICE campaign in comparison to the envelope for FZDZ from Appendix O.

Lastly, a short overview of the overall occurrence of different cloud conditions is given. We differentiate between small droplet icing (i.e. Appendix C conditions which contain almost no ice crystals), mixed-phase clouds (also Appendix C conditions, but with a significant number of ice crystals) and Appendix O conditions.

Glaciated conditions were not encountered. A plot of the frequency of occurrence of each of these conditions in each flight is shown in Figure 18.

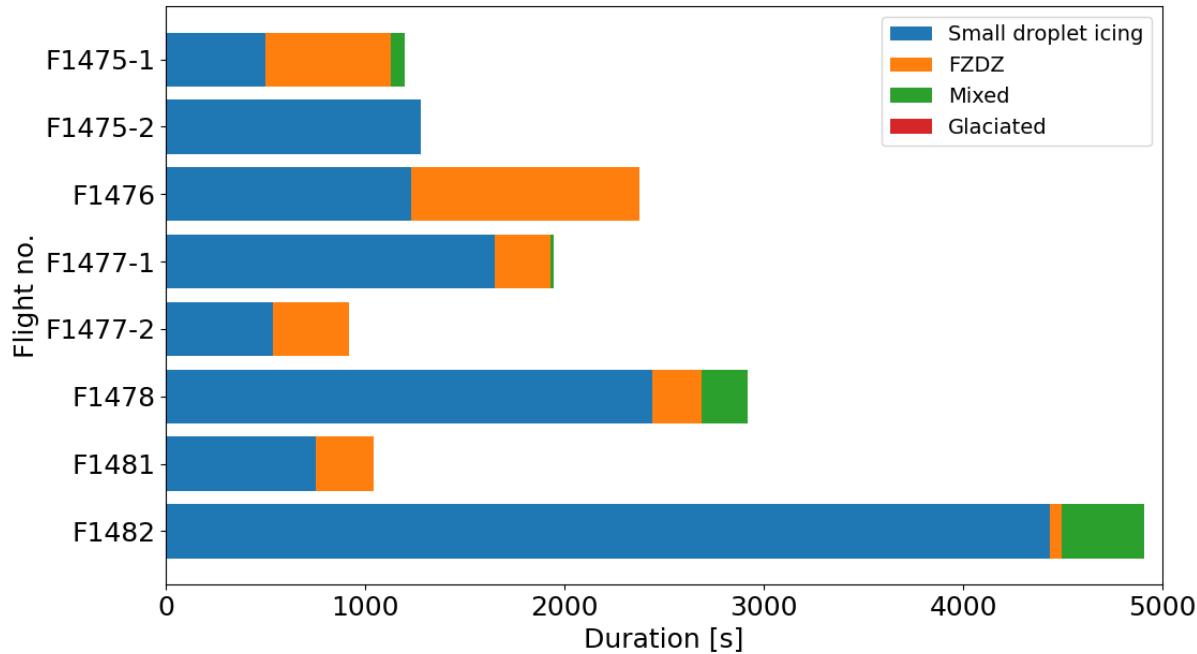


Figure 18: Frequency of occurrence of different cloud conditions during the North American SENS4ICE campaign.

Table 3 already listed the times in Appendix C and Appendix O conditions. Figure 18 shows that most of the Appendix C conditions contained hardly any ice crystals, just during few flights several minutes in mixed-phase conditions were encountered. During the campaign an effort was made to avoid conditions that are conducive to the formation of ice crystals, such as cloud top temperatures below -15°C and situations where ice clouds above could have seeded the cloud of interest. Furthermore, Appendix O conditions are often found above a significant stable layer that limits the potential for ice nucleating particles and cloud condensation nuclei from ascending into the cloud from the boundary layer.

3.2. Flight Campaign Europe

This section details the individual flights of the European flight test campaign and summarizes the atmospheric conditions that were encountered. The flights of the European flight test campaign were either performed as CER flights or as airways flights. CER (Contrôle Essais Réception / Dedicated ATC for tests & acceptance) refers to specifically designated areas that were reserved for the test aircraft. Flights in these areas were controlled by a dedicated controller, hence there was a lot of flexibility for adjusting the flight plan. However, CER zones only existed in the vicinity of Toulouse and towards the Atlantic coast near Bordeaux. If no suitable conditions were predicted for these regions, airways flights were performed. In contrast to CER flights, airways flights had essentially no flexibility to make changes in the flight path or even in altitude.

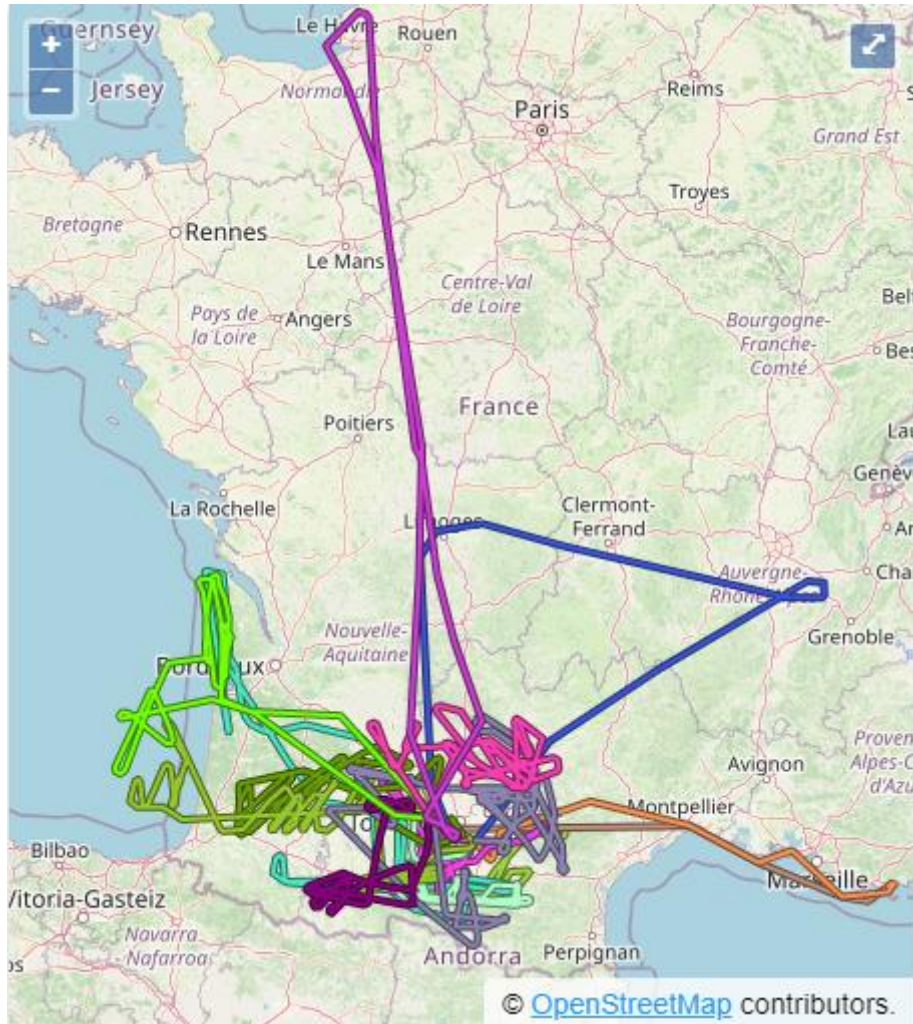


Figure 19: Flight campaign Europe April 2023 ground tracks [credit SAFIRE/ SENS4ICE project, Map data from OpenStreetMap].

Fifteen scientific flights were performed within the European flight test campaign. Additionally, one EMI flight and two test flights have been performed, which were not evaluated. Furthermore, aircraft and instrument issues were encountered during observational flights (OFs) 3 and 4, respectively so these flights were subsequently not evaluated. On flight OF1 to OF8 the Nevezorov data was considered unreliable and is hence not used. The LWC and derived parameters, such as icing flags, stem from the CCP for these flights. An overview of selected flights of the European flight campaign is given in the following.

DISCLAIMER: For Appendix C conditions the reference measurement results for MVD are only valid for a low concentration of large aspherical particles (parameter LAS N), see SENS4ICE deliverable D4.3 [8]. This was not necessarily the case particularly for the European flight campaign and is checked specifically for the analyses of individual icing encounters.



Table 4: Flights of the European flight test campaign.

Flight	SAFIRE flight number	Day	Flight time (UTC)	Time in Icing conditions [mm:ss]	Time in Appendix O conditions [mm:ss]
OF1	as230009	03/04/2023	05:47-09:35	90:13	1:28
OF2 pt1	as230010	04/04/2023	11:12-12:52	10:42	0:11
OF2 pt2	as230011	04/04/2023	13:05-14:29	12:14	1:48
OF3	as230012	06/04/2023	Aircraft problem	n/a	n/a
OF4	as230013	14/04/2023	Instrument failure	n/a	n/a
OF5	as230014	15/04/2023	05:24-08:11	40:37	12:40
OF6	as230015	18/04/2023	13:04-17:01	72:01	0:00
OF7	as230016	20/04/2023	09:43-13:17	2:38	0:00
OF8	as230017	22/04/2023	05:16-08:47	34:07	0:00
OF9	as230018	24/04/2023	12:24-16:47	90:57	59:48
OF10	as230019	25/04/2023	10:06-15:51	90:14	43:01
OF11	as230020	26/04/2023	05:56-08:52	13:42	0:00
OF12	as230021	26/04/2023	12:37-17:04	52:20	14:01
OF13	as230022	27/04/2023	05:50-09:57	62:42	6:14
OF14	as230023	27/04/2023	11:28-15:43	42:09	13:39

The following summarizes the atmospheric conditions in terms of microphysical cloud properties, temperature and altitudes observed during the European flight test campaign. The statistical analysis is based on 13 flights. In total, more than 10 hours were spent in icing conditions, and particularly in Appendix O conditions more than 2 hours. We note, that the uncertainties in LWC and TWC here are higher than during the American flight test campaign, due to discrepancies between optical and hotwire sensors (for details see SENS4ICE deliverable D4.3 [8]).



The temperature profile in Figure 20 shows median and 95 percentile LWC encountered during the SENS4ICE-

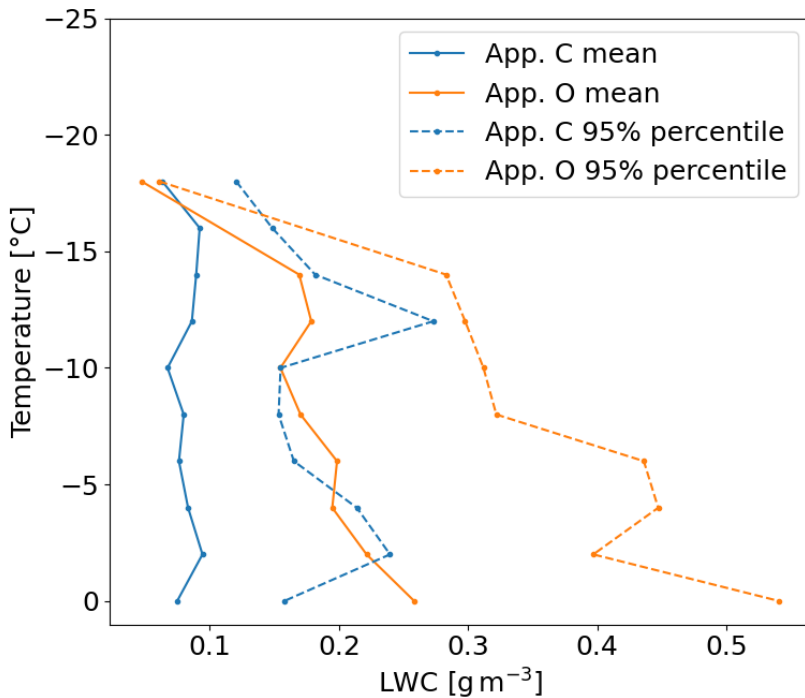


Figure 20: Mean and 95th percentile of the LWC in App. C and App. O conditions plotted against the temperature for the data of the European flight test campaign. The App. C values are based on the Nevzorov LWC sensor, the Appendix O values on the Nevzorov TWC sensor (see D4.3). Only flights where the Nevzorov worked are used for this plot. The data are based on 30 second averages.

European mission for Appendix C and Appendix O conditions. The highest frequency of measurements were obtained in the temperature range between -5 and -10°C. Mean LWCs were mostly between 0.05 and 0.10 for Appendix C conditions and between 0.15 and 0.25 g/m³ for Appendix O conditions. The 95th percentiles reach values of nearly 0.3 g/m³ in Appendix C and more than 0.5 g/m³ in Appendix O conditions. The data are based on the Nevzorov LWC sensor for Appendix C and on the Nevzorov TWC sensor for Appendix O. Median values and 95 percentiles were lower than during the North American flight campaign. As in the North American flight campaign, few icing conditions were sampled at temperatures less than -15°C, where they tend to occur less frequently in general. LWCs observed during flight in Appendix O conditions were slightly higher than those observed during flight in Appendix C conditions. That might be related to the presence of mixed-phase clouds, which were more dominant during the European campaign than during the American campaign. The ice crystals in mixed-phase clouds tend to deplete the available water vapor and thus decrease the overall LWC.

Figure 21 shows the TWC that was observed in Appendix C and Appendix O conditions for the European flight test campaign. In Appendix O conditions, which are defined such that hardly any ice crystals are present, the TWC can be considered to be equivalent to the LWC. Maximum LWC values observed during Appendix O encounters reached 0.6 g/m^3 , everything above that value is rare. Maximum TWC values (as opposed to the LWC values that were shown in Figure 22) observed during Appendix C encounters were as large as 1.2 g/m^3 .

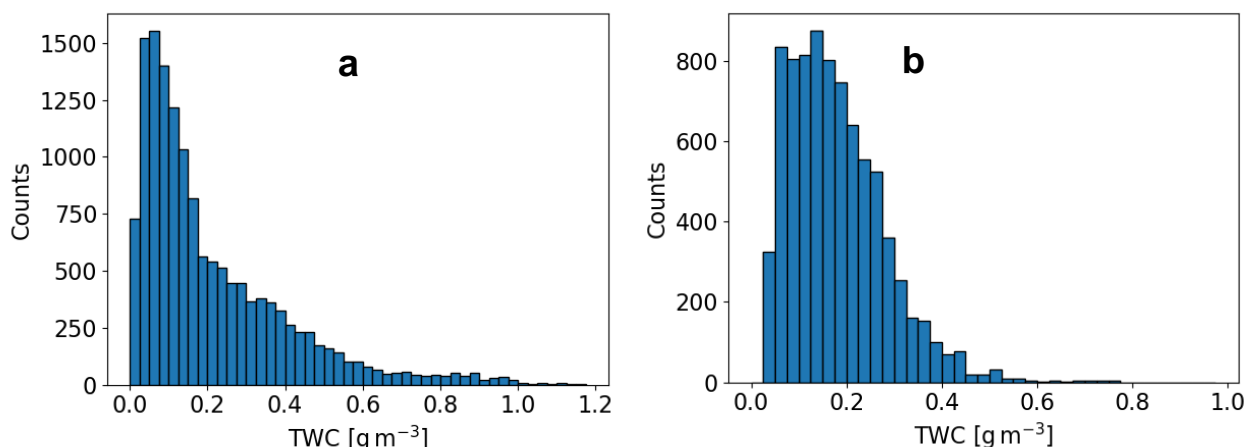


Figure 21: Distribution of Nevezorov TWC in Appendix C (a) and Appendix O (b) condition during the European Sens4Ice campaign. The counts are based on rolling 30 second averages that were evaluated computed for each second.

As for the North American campaign, also for the European campaign the LWC contained in SLD conditions is of great interest. A plot of the LWC contained in SLD can be seen in Figure 22. In comparison to the North American flight test campaign, we find a significant amount of clouds to have SLD LWC values between 0.025 and 0.05 g/m^3 during the European flight campaign. Also, the extreme values are larger, though these are very few and might be related to precipitation, which was very close, or, if slight inaccuracies exist in the temperature measurement, even above the melting point.

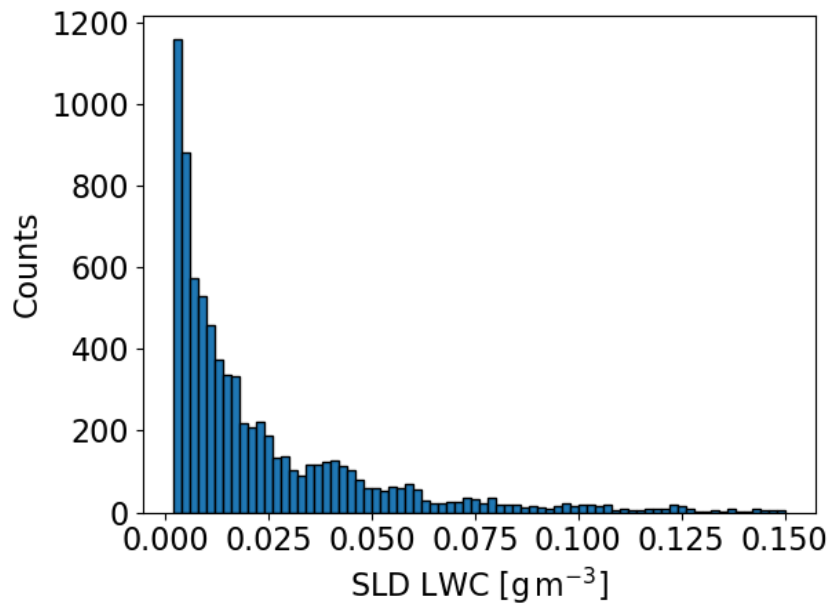


Figure 22: Histogram of LWC contained in SLDs (i.e. all droplets with diameters larger than 100 μm) during the European flight campaign. The counts are based on rolling 30 second averages that were evaluated computed for each second.

Furthermore, we present the cumulative mass distributions observed during the European flight test campaign. These can be seen in Figure 23. Many more Appendix O encounters were observed during the European flight campaign than during the North American campaign, in part due to the number of missions, but the Appendix O encounters during the European campaign were often of short duration (frequently well below one minute). The clouds were in general patchier. A comparison of the cumulative mass distributions of North American and European campaigns reveals, that the case of a cloud with an MVD around 23 μm , with few SLD embedded into the conditions, was hardly observed during the European campaign, while it was relatively common during the North American campaign. The European campaign data contains a lot of cumulative mass distribution curves with MVDs around 45 μm . The majority of MVDs observed during the North American campaign were smaller. Once again, differences in sampling strategy and the meteorological environments present (e.g. continental vs. maritime, month of the year, altitude, consistency) may have contributed significantly to the contrasts evident in the conditions observed during the two campaigns.

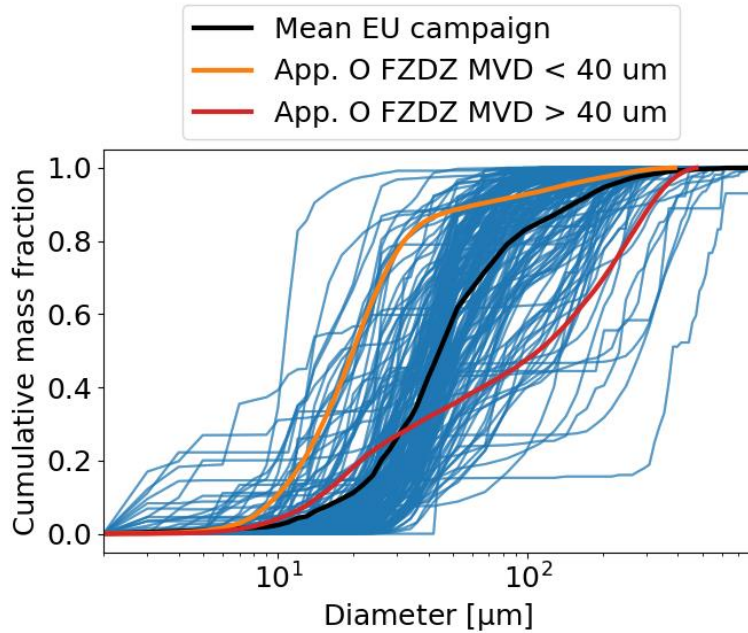


Figure 23: Cumulative mass distributions for each Appendix O encounter observed during the European flight campaign. The mean curve is plotted in black, the MVD of the mean curve is 45 μm . The cumulative mass curves for freezing drizzle MVD < 40 μm and MVD > 40 μm from Cober and Isaac [31] are plotted in orange and red, respectively.

Also for the European campaign, the liquid water content encountered in Appendix O conditions in comparison to the certification envelopes is of interest. The respective plot can be seen in Figure 24. Similar as for the North America campaign, the LWC was scaled to account for varying encounter lengths. It is apparent that especially for the regime FZDZ MVD > 40 μm several encounters exceed the maximum LWC specified in the envelopes. The encounters that exceeded the maximum LWCs originated from OF9, OF10 and OF14. All of these flights predominantly sampled mid-level clouds. Further studies should therefore be performed to assess if mid-level clouds frequently contain drizzle drops and have LWCs that exceed the Appendix O maxima.

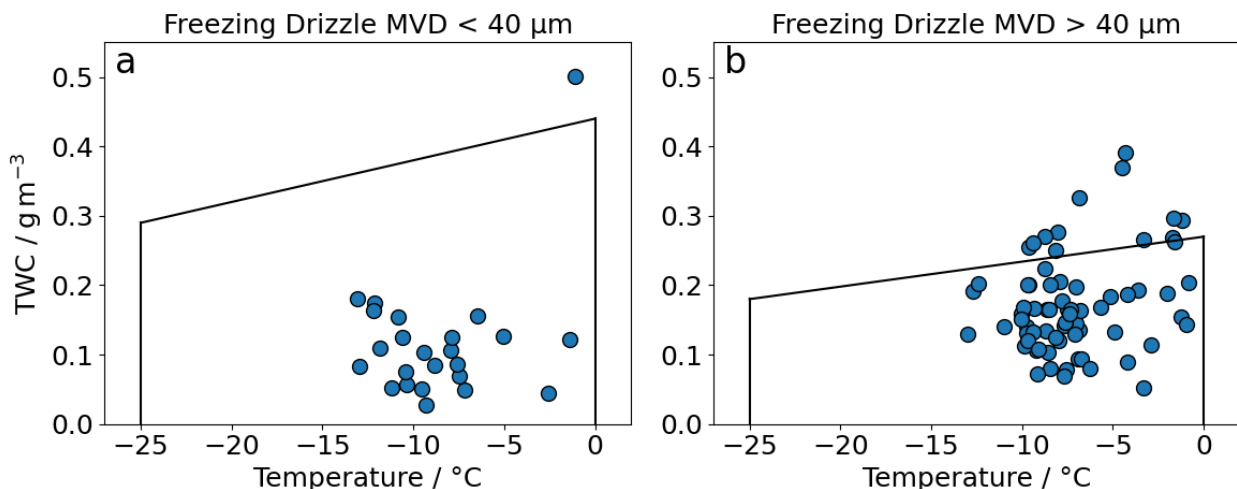


Figure 24: Nevezorov TWC of the Appendix O encounters during the European SENS4ICE campaign in comparison to the LWC envelopes of Freezing Drizzle MVD < 40 μm (a) and Freezing Drizzle MVD > 40 μm (b). The Nevezorov TWC is assumed to be equivalent to the LWC in Appendix O conditions because

Appendix O encounters were required to contain few ice crystals. Due to ambiguities that may exist in the detection of particles (see SENS4ICE deliverable D4.3 [8]) and due to the chance of intermittent mixed-phase pockets the TWC measurement of the Nevzorov may be contaminated by ice and thus too high for some of the encounters shown. Only encounters longer than 30 seconds were used for this plot.

As for the North American campaign also for the European campaign a comparison of the temperature and altitude range between the encountered conditions and the Appendix O certification envelopes was performed. This can be seen in Figure 25. Here, we see that the temperature decrease with increasing altitude follows very well the decrease in the envelope. No point exceeds the envelope. The temperature and altitude range were therefore characteristic for high altitude Appendix O conditions.

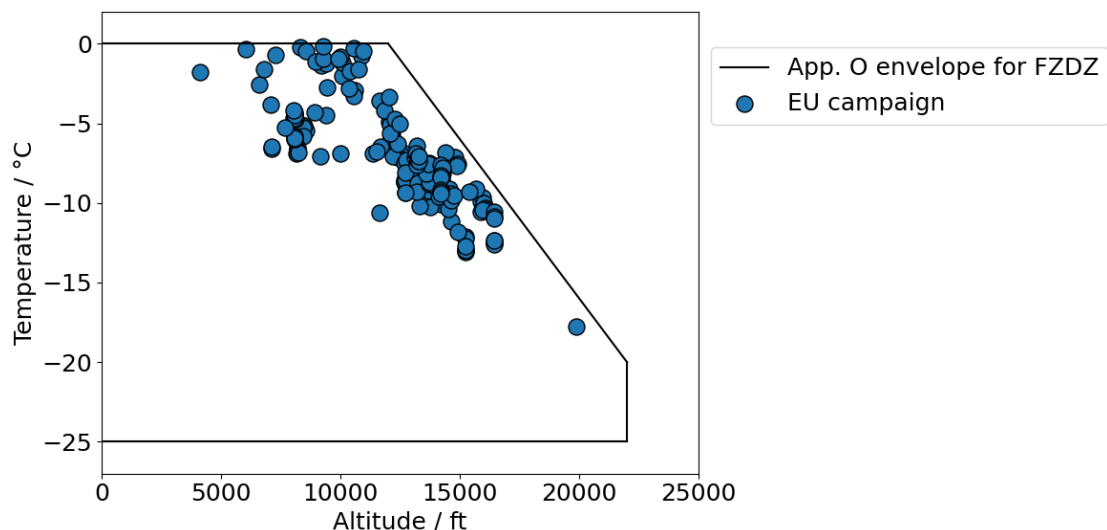


Figure 25: Pressure and altitude of Appendix O conditions encountered during the European SENS4ICE campaign in comparison to the envelope for FZDZ from Appendix O.

An overview of all flights with the absolute time spent in different conditions (purely supercooled small droplet icing ($D_{max} < 100 \text{ um}$; SM_DP_icng), FZDZ (see conditions described in section 3.3), mixed phase conditions and clear sky (clear) or clouds with positive temperatures (positive)) is shown in Figure 26. OF1, OF8, OF9, OF10, OF12, OF13 and OF14 had the highest rate of small droplet and FZDZ icing. For details on the data evaluation and the atmospheric conditions encountered see D4.3 [8].

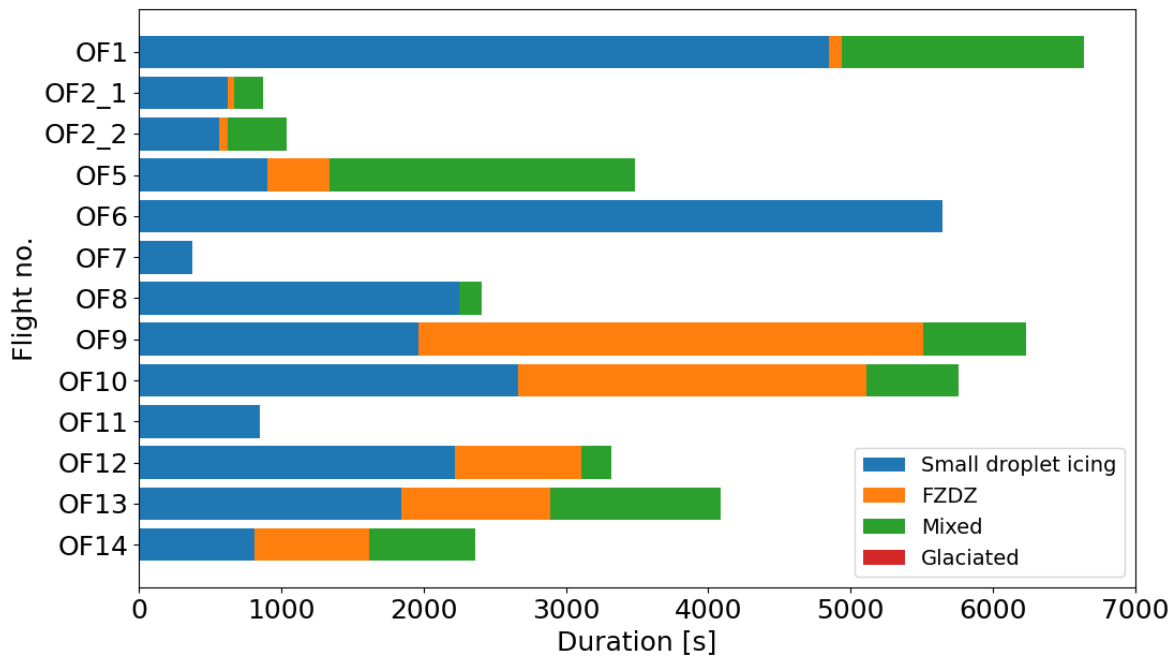


Figure 26: Overview of sampled time in different cloud conditions for all flights during the European campaign (except OF3 and OF4).

3.3. Comparison of flight campaign results with Appendix O envelopes

The comparison of the data sets from the two campaigns shows that significant differences existed in the altitudes where icing and Appendix O conditions were observed.

Both campaigns took place in similar latitudes, yet the North American campaign in more continental conditions and the European campaign with influence from the Atlantic Ocean. While the North American campaign was executed in February and March 2023, the European campaign was performed in April 2023. Further, considering the safety requirements of the two aircraft the altitude of measurements shifted to higher altitudes for the European campaign. De-icing for the European campaign was mostly done below 8000ft (~2.5 km) while during the North American campaign the de-icing was done above 3000 m. This resulted in different patterns how clouds were approached, i.e. from above or below. Such differences may have contributed significantly to the contrasts evident in the conditions found during the two campaigns, including the ranges and distributions of T, LWC, TWC, and drop size that were observed.

Appendix O conditions solely comprised FZDZ in both campaigns. FZDZ conditions encountered during the North American flight campaign tended to be bimodal and had mostly MVDs < 40 µm. FZDZ conditions during the European flight campaign were often unimodal (atypical for Appendix O conditions) and had MVDs which mostly ranged between 25 and 60 µm. For the North American flight campaign two Appendix O encounters exceeded Appendix O envelopes while for the European campaign several of the Appendix O conditions exceeded the LWC specified in the envelopes (Figure 27 and Figure 28).

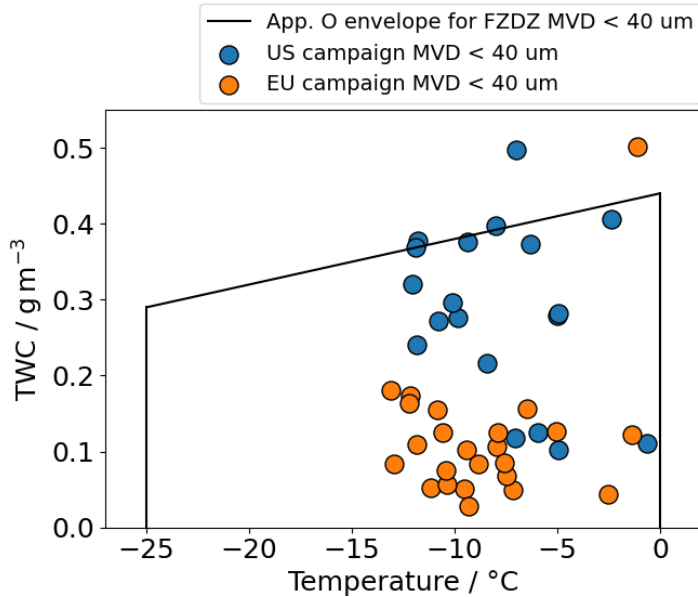


Figure 27: Comparison of the Nevzorov TWC measured during freezing drizzle encounters with MVD < 40 μm during both flight campaigns with the Appendix O envelope for freezing drizzle MVD < 40 μm . The Nevzorov TWC is assumed to be equivalent to the LWC in Appendix O conditions because Appendix O encounters were required to contain few ice crystals. Due to ambiguities that may exist in the detection of particles (see Section 3.3) and due to the chance of intermittent mixed-phase pockets the TWC measurement of the Nevzorov may be contaminated by ice and thus too high for some of the encounters shown. Only encounters longer than 30 seconds were used for this plot.

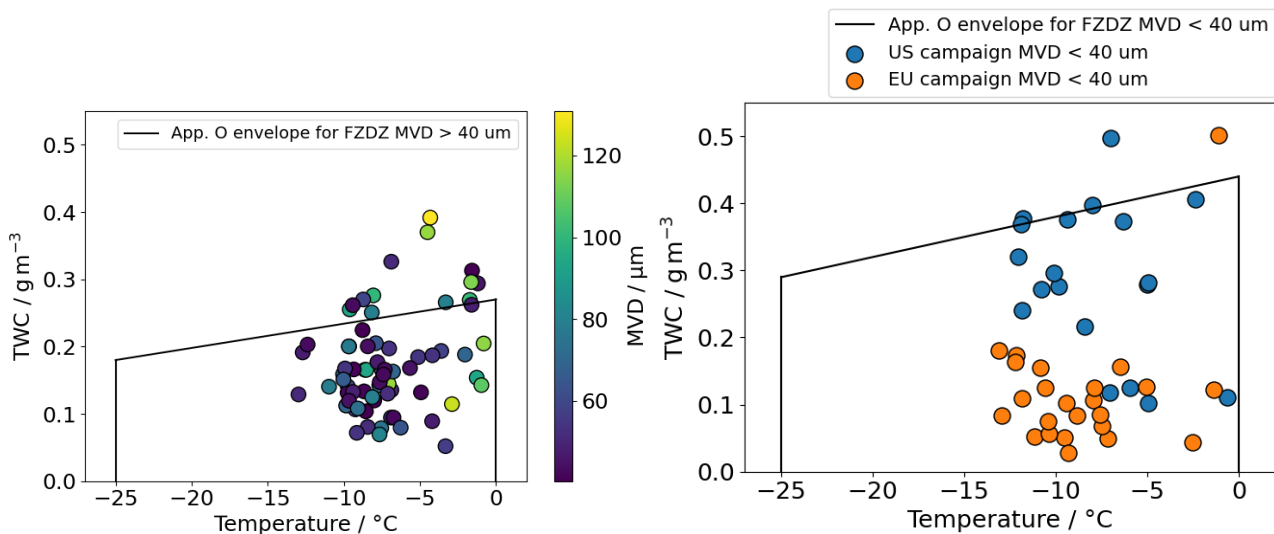


Figure 28: Comparison of the Nevzorov TWC measured during freezing drizzle encounters with MVD > 40 μm during both flight campaigns with the Appendix O envelope for freezing drizzle MVD > 40 μm (left: two different flight campaigns colour coded, right MVD colour coded). The Nevzorov TWC is assumed to be equivalent to the LWC in Appendix O conditions because Appendix O encounters were required to contain few ice crystals. Due to ambiguities that may exist in the detection of particles (see Section 3.3) and due to the chance of intermittent mixed-phase pockets the TWC measurement of the Nevzorov may be contaminated by ice and thus too high for some of the encounters shown. Only encounters longer than 30 seconds were used for this plot.

4. Satellite-based detection and nowcasting of icing conditions

One of the objectives of the SENS4ICE project was to increase pilot awareness of icing threats through the development of a remote detection technology. In the first phase of the project, the Meteorology Laboratory of CIRA developed a satellite-based tool for detection and nowcasting of icing conditions, which was tested during the European flight campaign. During the campaign, data on monitoring and nowcasting of icing conditions relying on the developed tools was provided via a Teamsite in pre-flight phase and updated in near-real time, i.e., with a delay of a few tens of minutes due to the time of receiving and processing satellite data.

In Figure 29 an example of the output of the icing detection tool is reported: it shows the areas potentially affected by in-flight icing hazard, giving an estimate of the severity of the phenomenon (light, moderate, severe) with indication of possible SLD conditions. An estimate of the minimum and maximum altitudes affected by the icing hazard is also available for each pixel of the map. The spatial and temporal resolutions of the product are respectively of about 3 km and 15 minutes, as the satellite data used in input. The implemented nowcasting tool is based on the extrapolation in time of the current weather condition, provided by the detection tool, to perform a forecast over a short period ahead. It provides in output the same kind of information of the detection tool on a reduced domain and at four different lead times: 15 minutes, 30 minutes, 45 minutes and 1 hour. A complete description of the detection and nowcasting tools developed by CIRA is reported in [10].

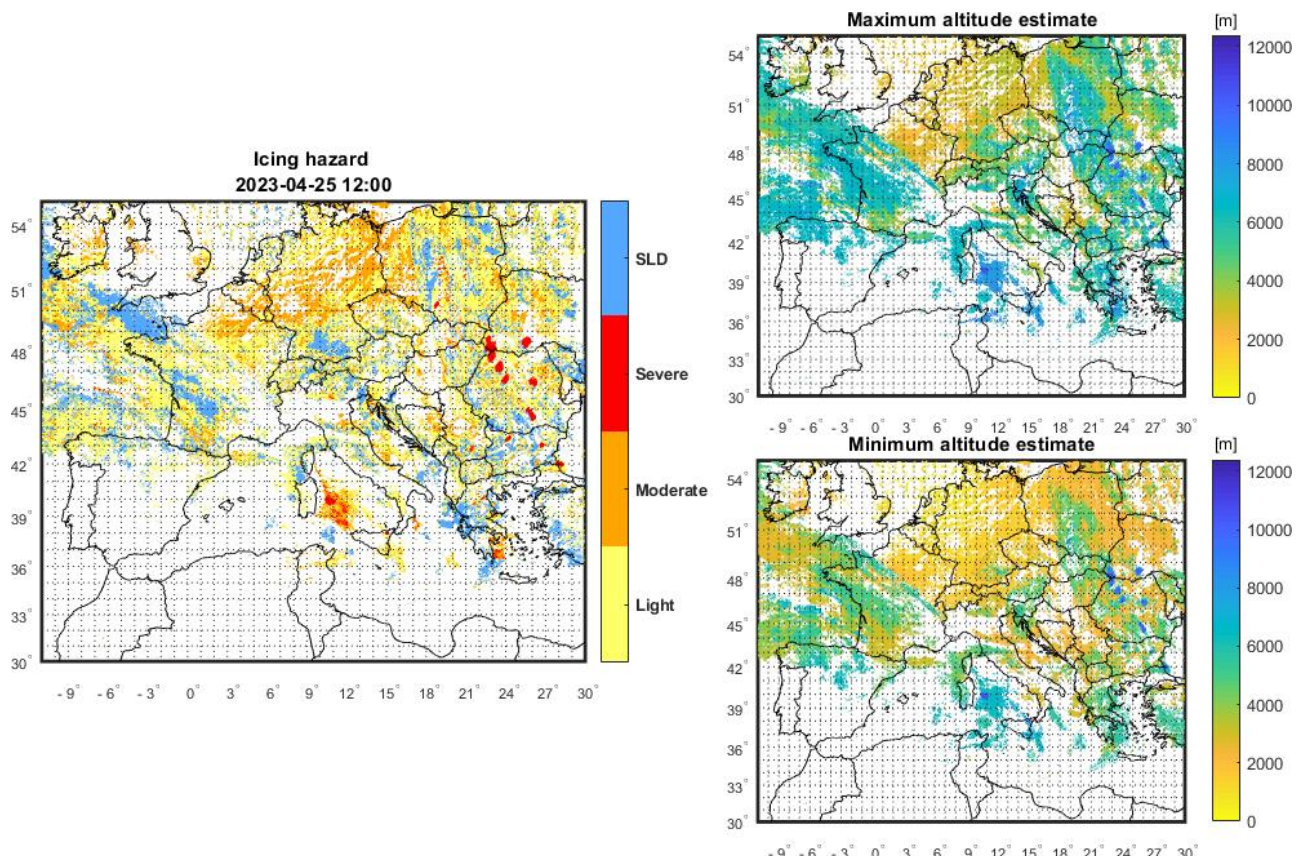


Figure 29: Example of the graphical output of the icing detection algorithm referred to 25 April 2023 at 12:00 UTC. The map on the left shows the icing hazard classified in light, moderate and severe plus an additional flag indicating possible SLD conditions. The two maps on the right report the corresponding minimum and maximum altitudes estimated by the algorithm.

Considering the challenge of validating such a kind of product, the SENS4ICE flight campaign represents an important chance to evaluate the performance of the tools in environmental icing conditions.

It is worth noting that data coming from the satellite detection tool have very different characteristics in terms of spatial and temporal resolution with respect to flight data. Concerning the spatial comparison, the nearest point to the position of the aircraft was considered from the satellite data. As for the temporal comparison, an updated satellite product was considered every 15 minutes (satellite data refresh rate) and each one was considered as representative of the time range of 15 minutes centred around its reference time.

An example of the methodology used to compare flight data and satellite data is shown in Figure 30. The panels in Figure 30 represent the progress of the aircraft along its route every 15 minutes. Specifically, each panel shows, on the left side, the map of the CIRA detection tool with the corresponding flight leg highlighted in blue, and, on the right side, the time series of the variables recorded during the flight. In particular, the time series of the top plot reports the flight altitude of the aircraft along with the minimum and maximum altitude estimated by the satellite detection tool for the icing field (if present). The second plot reports the reference icing flags evaluated by DLR relying on the microphysical cloud parameters measured in-situ and, finally, the third one reports the icing flags detected by the CIRA tool. In the first phase of the flight (Figure 30 (a)), no icing conditions were encountered by the aircraft, and this was correctly detected by the CIRA satellite tool. Then the aircraft entered an area affected by icing hazard (Figure 30 (b)), where the icing is indicated according to the icing flag from the DLR reference measurements. It is interesting to note the good timing of the satellite detection tool which correctly starts to indicate icing conditions. These conditions are detected also in the following leg of the flight (Figure 30 (c)), when the comparison is not possible as the aircraft was descending for landing and was outside the range of altitudes identified by the satellite tool (which refers to the cloud layer).

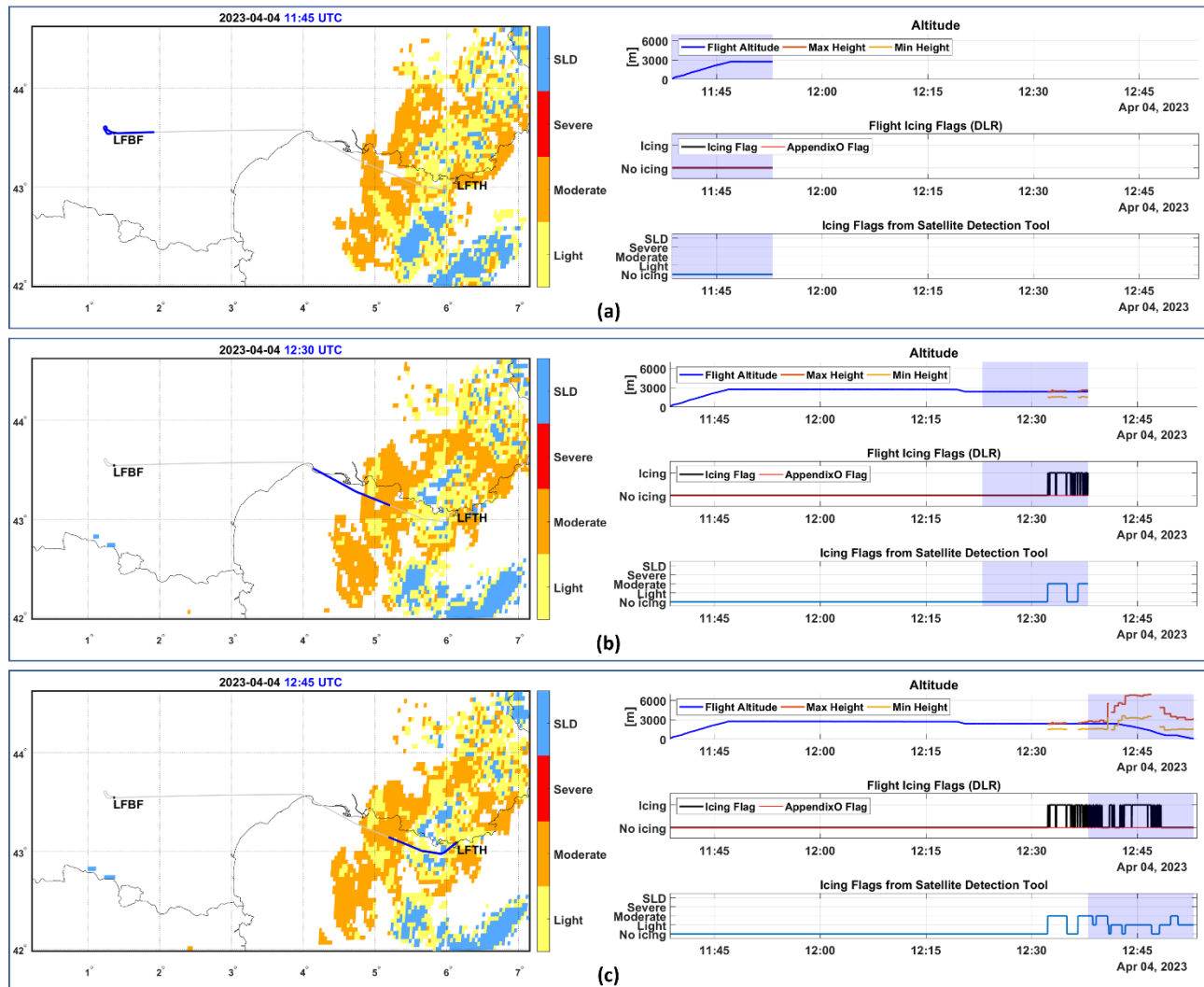


Figure 30: Example of the methodology used to compare flight data and satellite data. Each panel shows, on the left side, the map of the CIRA detection tool and, on the right side, the time series of the flight variables.

Another example of comparison between the time series of the CIRA tool output and the variables observed during the flight is shown in Figure 31. In Figure 31 the parts of the time series highlighted with a shaded blue area represent the flight legs characterized by static air temperature below 0°C and are the parts for which the comparison with satellite tool output can be made. Indeed, the remaining parts (with white background) are not comparable since they correspond to times in which the aircraft was descending in altitude for de-icing,

but clearly the satellite tool always refers to the cloud layer above. From the comparison between cloud drop diameters it seems that the two curves are very different, but it is worth noting that the greater differences occur inside or near the areas of the plot with white background, corresponding to the descent in altitude of the aircraft. These differences are due to the big droplet measured when the aircraft descended because it was raining below the clouds (as reported in the SAFIRE flight report). Excluding these parts of the time series, the order of magnitude of the two variables is similar, and this is a good result as the estimation of MED (Median Effective Diameter) from satellite is a difficult task. The two bottom plots of Figure 31 report the icing flag from the in-situ reference measurements of DLR and the icing flag remotely detected from satellite by CIRA. In particular, for this last one, the three severity levels (light, moderate and severe) were collapsed in a single icing flag (yes/no) in order to facilitate the comparison with observed conditions. The plots reveal that almost all the flight was conducted in icing conditions, and the satellite tool correctly detected icing. Furthermore, several encounters of App. O conditions occurred and they were detected also from the satellite tool. The matching is not punctual, but this is partly due to the different nature of the data compared, characterized by very different spatial and temporal resolutions.

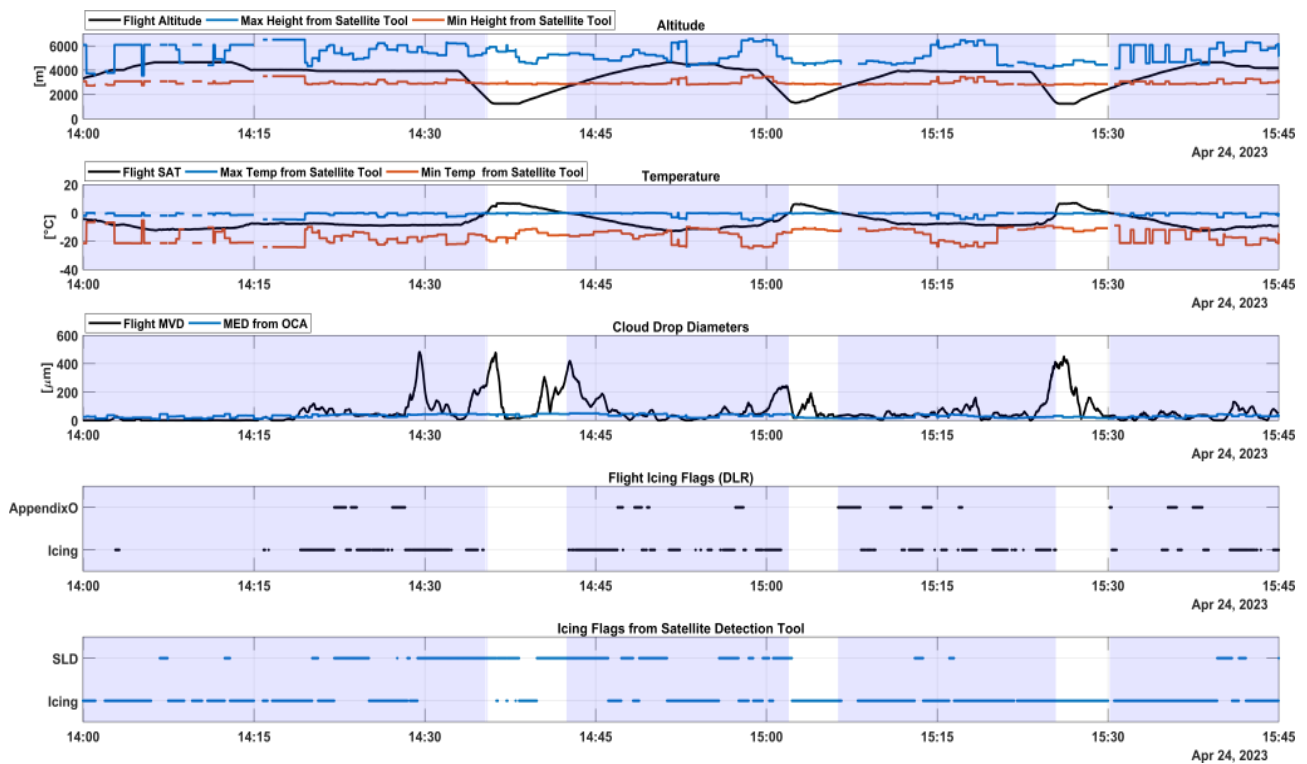


Figure 31: Comparison between the time series of the variables observed during the flight and the output of CIRA detection tool.

The described results regarding the evaluation of the detection tool in relevant icing conditions are promising, suggesting that this satellite-based approach, after further maturation, can be exploited for applications supporting aviation meteorology. Indeed, additional investigations are ongoing with the aim of performing a more detailed validation to identify the strengths and weaknesses of the tool and the needed steps for its future exploitation.



5. Direct Ice Detection Technologies Development, Maturation and Demonstration

SENS4ICE addressed development, testing (icing wind tunnel and in flight, in both cases with a focus on freezing drizzle and without addressing freezing rain conditions), validation, and maturation of different detection principles, as well as the final airborne demonstration of technology capabilities in relevant natural icing conditions. Hence ten different technologies with diverse physical principles for directly detecting icing conditions were developed and/or advanced. At the project beginning, the sensor technologies had different levels of technology readiness, some at very low levels and others having had already passed steps of technology testing. In the first phase of the project, all sensors reached the status to be ready for icing wind tunnel testing. Note that one particular technology, the DLR CM2D, combines a Nevzorov Probe and the Backscatter Cloud Probe with Polarization Detection (BCPD) with the aim to improve airborne scientific and reference measurements, with special focus on the SENS4ICE flight test campaigns. The other nine direct sensing technologies target applications for operational air transport. These sensor technologies can be clustered into two categories:

- atmospheric sensors, that measure the atmospheric conditions, and
- accretion sensors, that measure ice accretion on the aircraft.

Table 5 gives an overview of the icing sensor technologies under development in the SENS4ICE project.

Table 5: SENS4ICE sensor technologies overview, sensor types and principles.

Sensor	Developer	Sensor Type	Sensor Principle
AIP	AeroTex	Atmospheric	Isothermal with inertial separation at different sensors along aircraft
IDS	Collins	Atmospheric	Thermal response to heat impulse
LILD	DLR	Accretion	Ultrasonic wave attenuation / phase change
SRP	Honeywell	Atmospheric	Collecting backscattered light from particles
FOD	INTA	Accretion	Latent heat measured with fiber optic
AHDEL	ONERA	Atmospheric	Particle charging and subsequent measurement of the charge
AMPERA	ONERA	Atmospheric	Measurement of aircraft electric potential
AOD	Safran	Atmospheric	Shadowgraphy
PFIDS	Safran	Accretion	Optical reflection from accretion
CM2D [BCPD]	DLR	Atmospheric	Single particle optical backscatter
CM2D [Nevzorov]	DLR	Atmospheric	Isothermal measurement of water content

The following sections describe the development, maturation and demonstration of the SENS4ICE direct ice detection technologies. For further information and details please refer to SENS4ICE deliverable D4.1 section 3.



5.1. AeroTex AIP - Atmospheric Icing Patch

5.1.1. Technology Description

The AeroTex-AIP comprises of two key components; the **isothermal heater** unit and a data processing and control unit. The heater is a custom designed 20mm square patch that is installed on an insulated mount that prevents excess heat being drawn into the aircraft structure. An erosion shield is bonded on top of the heater and mount to provide protection for the heater. Two temperature sensors are integrated in the development unit to monitor and control any over-temperature of the system. The individual heater patches operate at high temperature (~120°C) but their small size means that they draw little power (<30W).

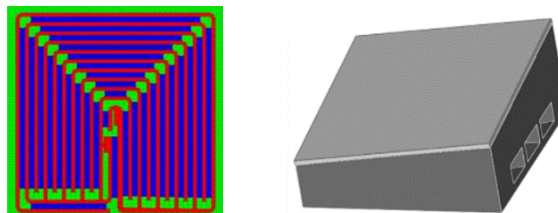


Figure 32: AIP heater (left) and an insulated mount (right).

The second unit part of the system is the data processor. The primary role of the data processor is to process atmospheric and operating condition data from the flight computer (speed, temperature, angle-of-attack etc.) and combine it with a **measurement of the power drawn by the heater units** to determine whether icing conditions exist. The data processor unit also provides a safety role as it monitors for weight-on-wheels, sensors overtemperatures and sensor open or closed circuits.

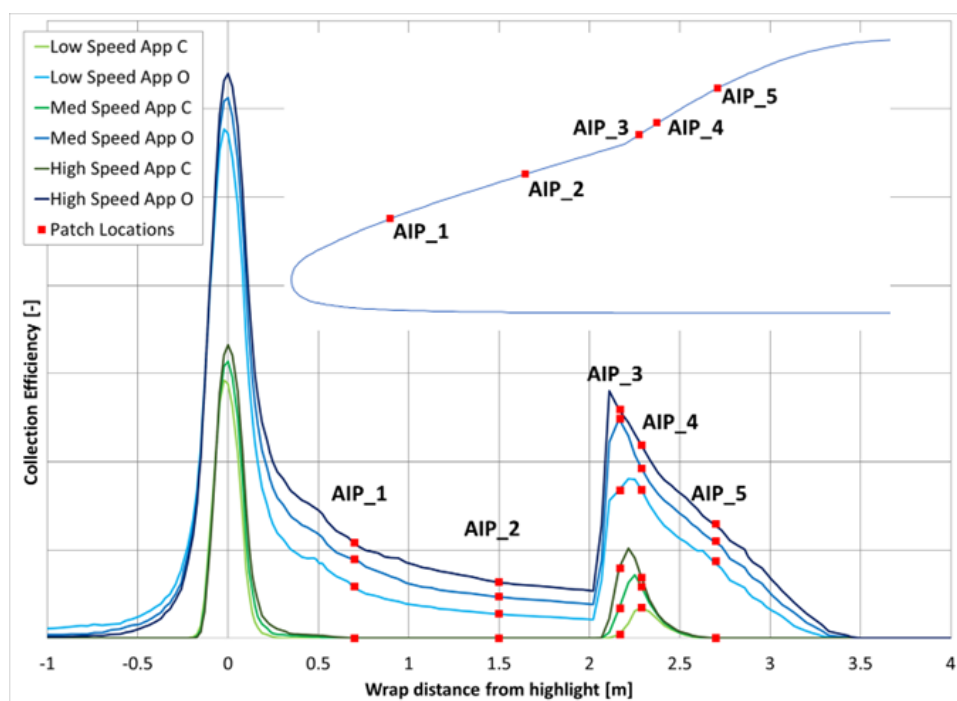


Figure 33: Example showing sensor locations on the forward fuselage.

A key aspect of the AIP system is the use of a network of sensors distributed over the forward fuselage which allows differentiation between small and large droplet icing to be differentiated. Figure 33 shows an example installation when the forward two sensors are only subject to impingement under large droplet icing conditions, as indicated by the blue/grey curves with the small droplet icing conditions indicated by green curves indicating zero impingement. The figure also shows that AIP_3 and AIP_4 sensors are subject to icing in both large droplet and small droplet icing conditions. Therefore, by monitoring the system response in these different positions, icing can be identified. Figure 34 shows an example response for a two-sensor system under large droplet icing with the large droplet sensor responding when the larger droplets are present.

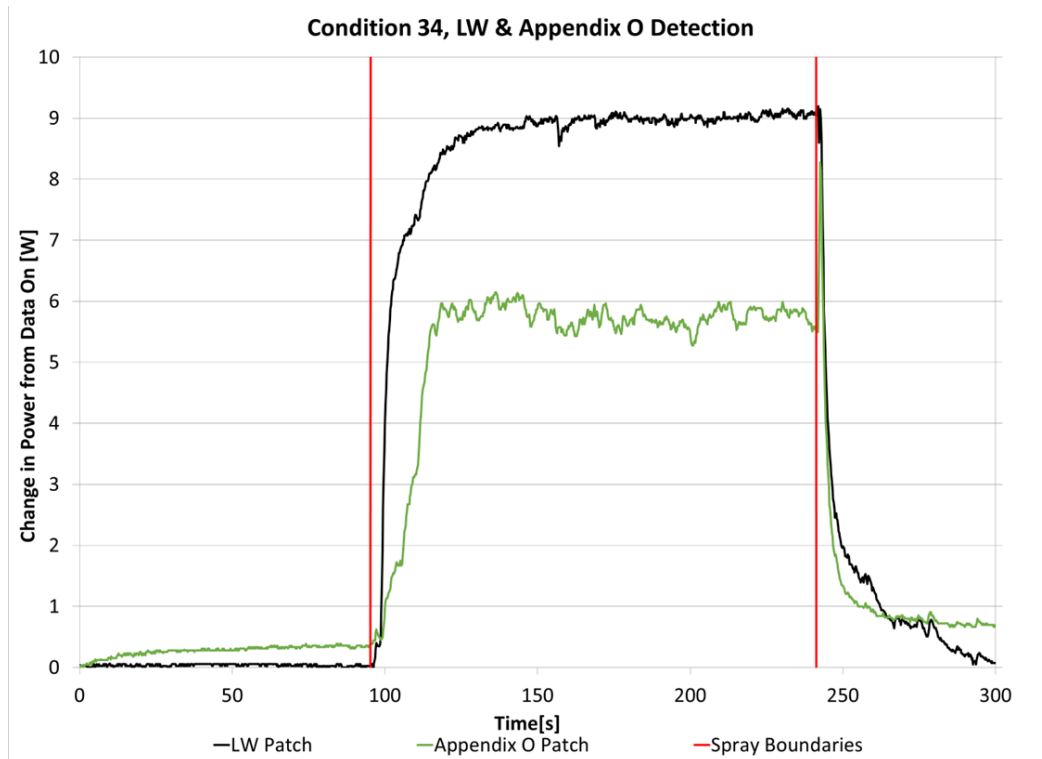


Figure 34: Example of sensor response for large droplet icing conditions (lower).

5.1.2. Technology status at project start

During the early 2010's, AeroTex tested a probe type detector that operated on the same principle as the AIP (see left hand side of Figure 35). Where the probe was maintained at isothermal conditions, and the presence of icing can be inferred from the power required to maintain the temperature and comparing this to a dry reference dataset. This test was an add-on to a main test programme and therefore had limited development associated with it. The fundamental technology and approach was successfully demonstrated to TRL2 but required significant further work and investment to mature the technology further.

5.1.3. Technical Work

During the first phase of the SENS4ICE programme a number of trade studies were performed to decide on the best configuration of sensor/sensors to detect icing and discriminate between small and large droplet icing conditions (Figure 35). The different concepts had to balance power, weight and costs against the technical driver of robust ice detection. The final concept, as shown in Figure 35 was defined after a number of iterations both in terms of design and heater technologies that were used.

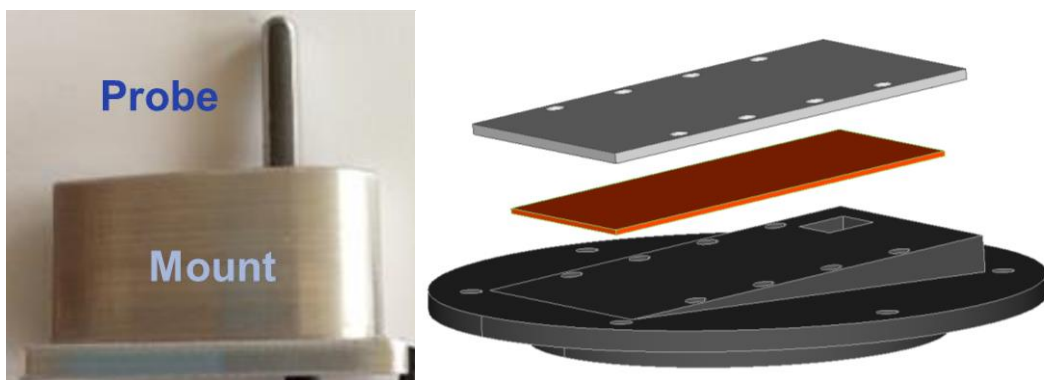


Figure 35: Candidate configurations for the AIP system.

Just as critical to the success of the AIP was the selection of the platform. Initial studies on the ATR 42 platform showed that the location available for sensor installation meant that the concept of a network of sensors could not be fully tested. Therefore, the Embraer Phenom 300, which had forward fuselage locations available for installation, was selected as the flight test platform.

In addition to the hardware development, the analysis software is key to the success of the programme. The main challenge for thermal systems is to correctly calculate the heat loss due to dry air flight such that any changes from this value can be identified as icing conditions. For SENS4ICE, this correlation is initially based on analysis data but during flight trials, dry phases of the flight were used to provide the correlation.

5.1.4. Flight Test

For the flight test an array of 5 AIP were located along the centreline of the Embraer Phenom 300 flight test platform. The locations for the installation were based on the locations shown in Figure 33 and are shown mounted on the aircraft in Figure 36. For this installation wire bundles were run along the outside of the aircraft and routed in through a ventilation pot into the forward luggage bay.



Figure 36: AIP sensors mounted along the centreline of the aircraft [image AeroTex with Embraer permission/ SENS4ICE project].

The AIP control and logging system was installed on an equipment rack inside the aircraft. The system consists of a main processor, logging and communication unit, a power regulator unit and two in-house manufactured electronics units used for power monitoring and controlling power to the patches and the control unit.

The flight tests were based in East Alton, Illinois and were performed between the 22nd February 2023 and the 10th March 2023.

The system showed good response during the initial flight tests and some initial results are shown in Figure 37. The black dots represent when the reference ice detector detected any form of icing and the green dots show the MVD measured by the reference ice detector. The yellow dots show when any form of icing was detected by the AIP system and the yellow dots show when SLD conditions were detected. The figure shows that the system performed well in detecting all icing conditions and differentiating between small droplet and large droplet icing conditions.

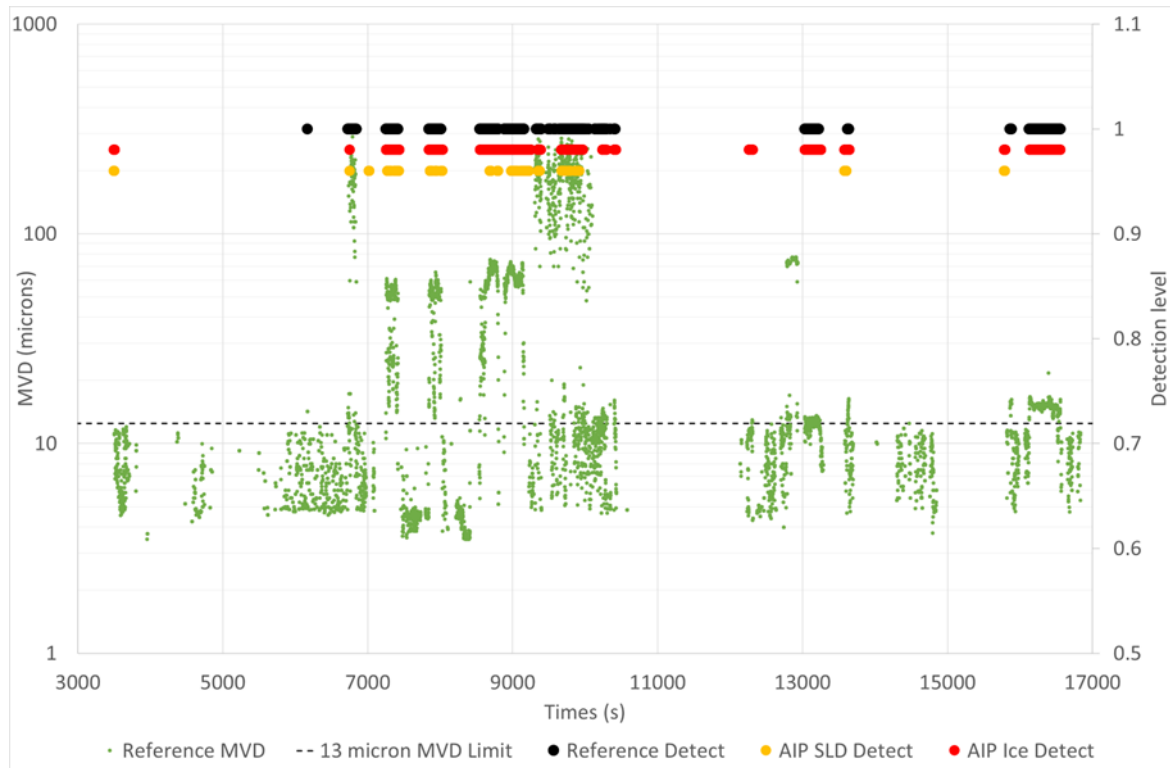


Figure 37: AIP system response for flight 1475, shown alongside data from the reference sensors.

Initial attempts at assessing the severity of the icing conditions were also made based on the response of the different sensors. This approach shows some promise but requires further maturation. During the tests the response of the AIP sensors degraded and the reason for this is currently under investigation.

5.1.5. Current TRL

The current TRL of the AIP is assessed as TRL5 for the sensor and signal processing aspect and TRL4 for the integration and robustness aspects.

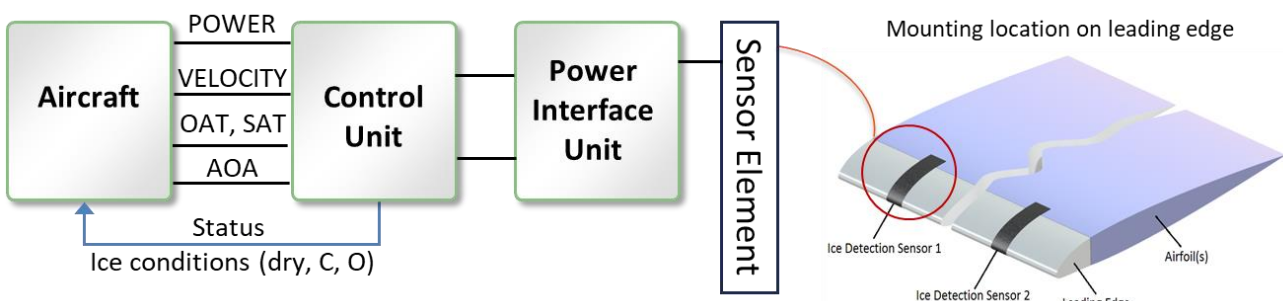
5.1.6. Short summary of further development, maturation and exploitation

Based on the success of the AIP sensor under the SENS4ICE project, AeroTex has secured further funding under an Innovate UK, NATEP programme funded by the UK government. This programme will investigate alternative materials used in the sensor, develop capabilities for ice crystal detection/differentiation and improve the estimation of icing severity. AeroTex have partnered with Printed Electronics Limited (<https://www.printedelectronics.com/>), to support the sensor development and Cranfield University to provide testing capabilities. In addition, discussions with aircraft manufacturers are advancing with initial implementation based on liquid water and SLD differentiation.

5.2. Collins – IDS

5.2.1. Technology Description

Collins-IDS is made of two components: (1) Sensing Element that uses a proven and certified construction made of high temperature composite, temperature sensors and metallic heater that measure heat flux distribution and communicate this to the power interface control unit. (2) Power Interface Control Unit (PICU) that provides the necessary power to the sensing element, analyses the measurements, and makes recommendation on icing conditions Dry or App. C or App. O. Detection and differentiation is done with a built-in detection algorithm within the PICU. The system is scalable to include one or multiple sensing elements positioned on sensitive areas of the airplane, powered individually, and controlled together by a master controller.



Collins-IDS Schematic



Collins-IDS components

Figure 38: Overview of Collins-IDS structure, possible mounting location, and communication with the aircraft [Phenom 300 aircraft image copyright Embraer].

Installation of Collins-IDS on the aircraft is flexible. It can be integrated on the leading edge by being installed inside of the leading edge and/or areas of the leading edge where no ice protection is installed, for example wing and/or tail tips, vertical fin and other. IWT and flight test results show very good performance for detection and differentiation within the required response time for installation on the leading edge. Further improvements can be achieved by installing the sensor in other more sensitive areas than the wing leading edge to ensure ice detection before wing or other aerodynamic surfaces. For easy maintenance and replacement, the sensor can be installed in a dedicated strip over the leading edge, under the leading edge or integrated in a recessed composite leading edge. This way Collins-IDS is replaceable without replacing the whole leading edge.

IWT and flight test results proved the sensor as a viable ice detector and differentiator of App. C and App. O icing conditions, by using one single sensing element. If necessary, further improvements can be done tailoring the heater strips with different power density along the sensor chord to improve performance.

Prior to flight test, further refinements of the power interface control unit was carried out reducing the sensor power requirement by over 62% from 800W to less than 300W and improving the accuracy of the detection algorithm. The sensor completed 220 hours of icing wind tunnels tests at Collins Aerospace and NRC test facilities as well as 25 hours of flight test in natural icing conditions.

The system achieved TRL6 in 2023 following a successful flight test with Embraer during the SENS4ICE North American flight test campaign.

5.2.2. Technology status at project start

The Collins-IDS is a concept developed by Collins Aerospace under self-funding. The system builds upon a patented ice detection technology based on thermal response on a heater that changes from dry to icing conditions. The system had only been used for basic ice detection and has not been flight tested. The detection principle is based on measuring the heat flux variation in different icing conditions using a heater. Advanced composite materials are increasingly used in aerospace applications due to superior stiffness, strength, fatigue, and corrosion resistance.

The Collins-IDS technology had been developed by Collins Aerospace prior to SENS4ICE project and was at TRL2. The sensor system can take direct measurement at areas of interest and offers multiple sensors capability.

5.2.3. Technical Work

Collins Aerospace continued the development of the Collins-IDS within SENS4ICE maturing the technology to TRL6. The technology components were designed and tested in simulation, IWT and flight test natural icing.

5.2.4. Flight Test

The Collins-IDS sensor was flight tested in the SENS4ICE North American flight test campaign in February/March 2023. Figure 39 shows a view of Collins-IDS installed on Embraer Phenom 300.

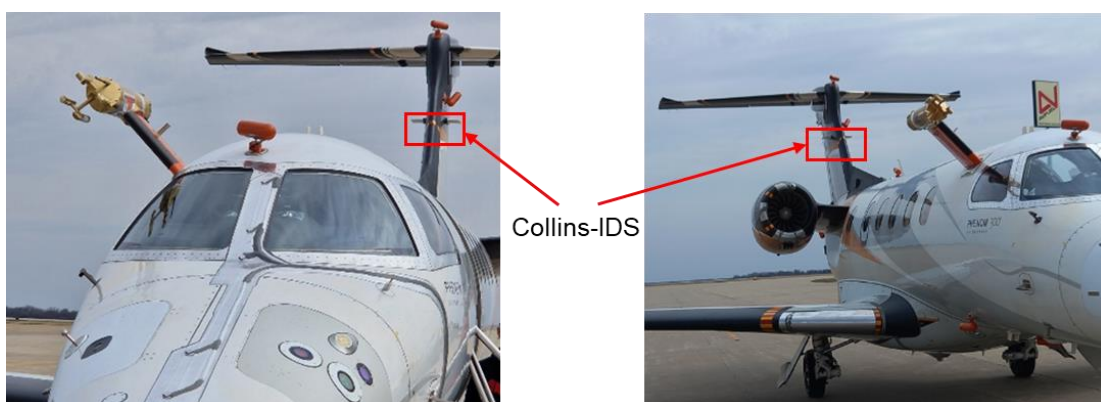


Figure 39: Collins-IDS sensors mounted on the vertical fin of the aircraft [image copyright Embraer/SENS4ICE project].

While during the IWT, the conditions were controlled both in terms of LWC and MVD, the conditions during the flight tests were more fluid; both the LWC and MVD were temporally variable. Both the control algorithm as well as the detectors were updated to perform better under non-experimental (uncontrolled) conditions. The class boundaries for the new combined differentiator are shown in Figure 40.

For the flight tests, the sensor can detect and differentiate icing conditions encountered by the aircraft, to a great degree of accuracy, and within a short time of conditions being encountered. The performance of the detector is shown in Table 6.

The confusion matrix was generated using class boundaries calculated using observed prior probabilities of conditions – this results in the best possible confusion matrix where every classification error has the same weight. The priors could instead be weighted according to the impact of misclassification, moving the boundaries slightly and resulting in a more practical classifier.

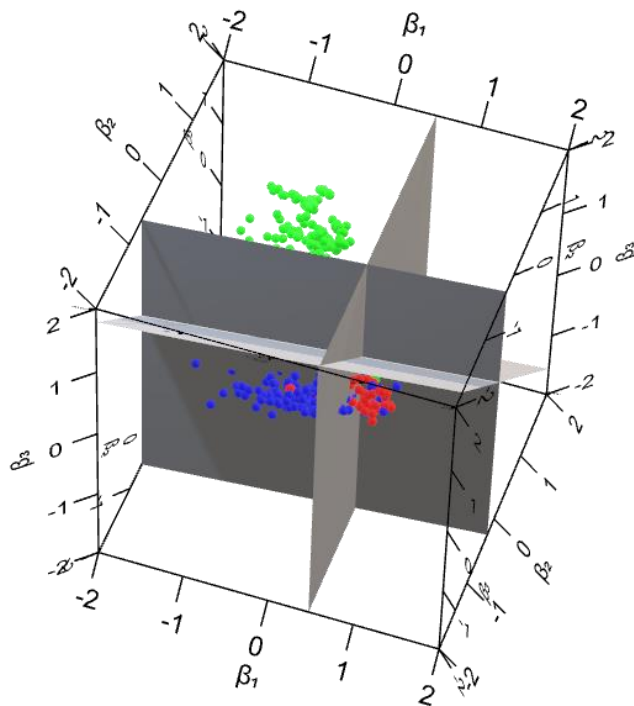


Figure 40: Classification boundaries for all three conditions. Dry conditions (green), App C conditions (blue), and App O (red).

Table 6: Confusion Matrix for Collins-IDS detection and differentiation algorithm.

		Predicted Class		
		Dry	App C	App O
True Class	Dry	97.17%	2.83%	0%
	App C	1.69%	91.53%	6.78%
	App O	2.44%	18.29%	79.27%

An example flight test campaign is shown in Figure 41. The raw outputs of the Collins-IDS are shown on the top graph, along with the areas denoting detected conditions: dry (green), App. C (blue), and App. O (red). For comparison, the graph on the bottom shows the reference measurements “ground truth” LWC and MVD, and the “ground truth” conditions are again depicted with areas of the same colours.

Flight test 1476 - 25 February 2023

During the North American flight test campaign, the flight 1476 encountered multiple significant icing events. Specifically, there were five instances where the aircraft experienced App. O icing conditions, which were denoted in red. Concurrently, App. C conditions were observed and marked in blue.



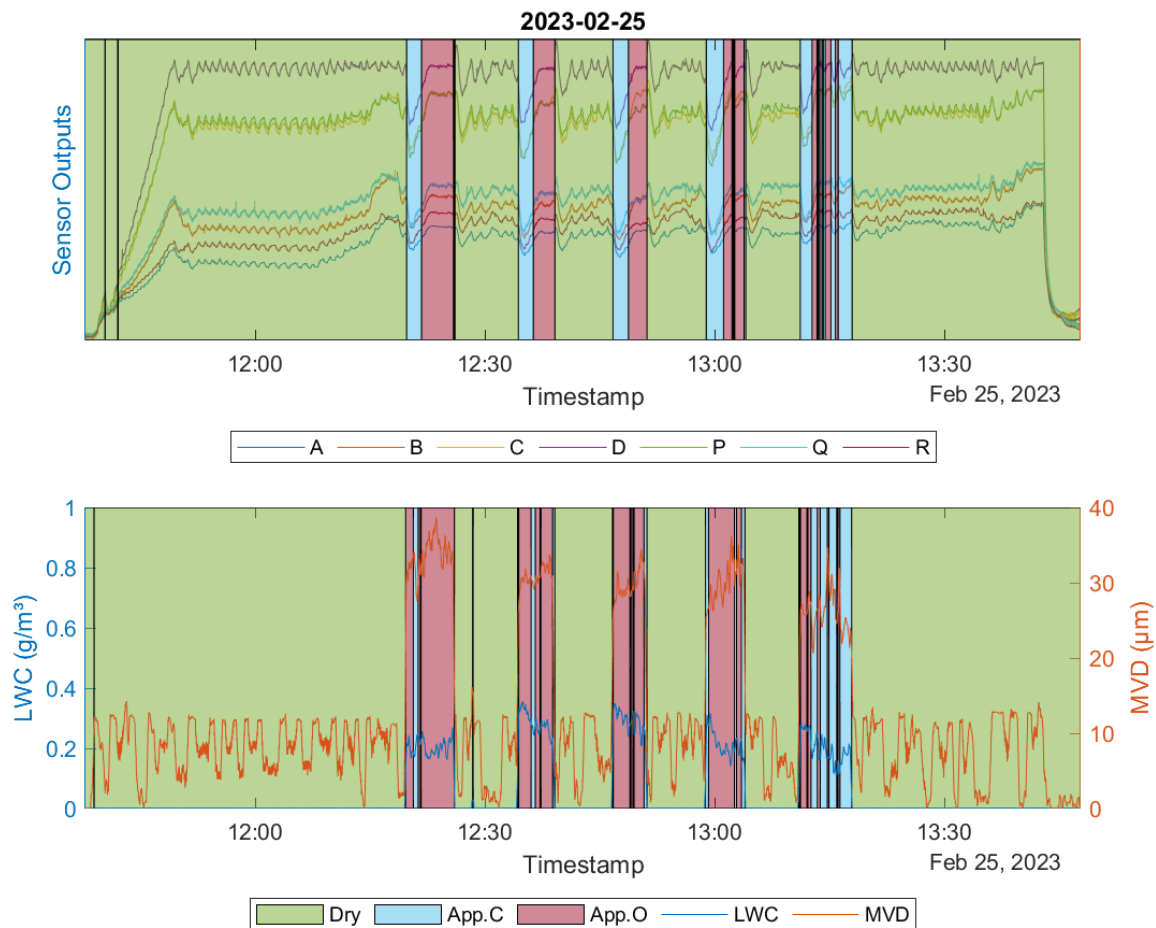


Figure 41: App. C and App. O encounters during flight test. Bottom figure is ground truth, top graph is Collins-IDS sensor and detector outputs.

5.2.5. Current TRL

Collins-IDS achieved TRL6 at the end of the project following successful IWT testing, over 220 hours over the course of the project at Collins IWT and NRC IWT, followed by successful flight test completing over 25 hours in natural icing conditions.

5.2.6. Short summary of further development, maturation, and exploitation

Collins-IDS successfully passed TRL6 and MRL6. Further development is needed to focus on a dedicated Power Interface Controller Unit for the SENS4ICE application. Additional flight test data are also needed covering wide range of App O conditions. IWT enhancements to cover App. envelope needed, which (1) will allow for the ice detection/differentiation algorithm to be refined further and (2) support the development and testing of the Collins-IDS for different aircraft applications.

The technology was transferred from R&D to applied technology for finalizing hardware industrialization processes.

5.3. DLR – LILD

5.3.1. Technology Description

The basic working principle of the LILD sensor consists in detecting ultrasonic lamb wave packets, which are transmitted through an icing prone aircraft structure as e.g. wing or tail leading edges. Therefore, a transmitter and a receiver are placed on this structure in order to obtain the wave propagation behaviour, see Figure 42 left. An ice accretion can be detected in a variation of the received signal amplitude and propagation time, since a layer of ice changes the mechanical parameters (stiffness, damping and mass) of the skin material. The sensor itself consists of an electronics box within the fuselage, which is used to generate the transmitter signals and to analyse and process the obtained receiver signals, and at least one transmitter and one receiver piezoelectric transducer, which have to be applied on the aircraft surface, where ice accretion has to be detected, see Figure 42 on the right.

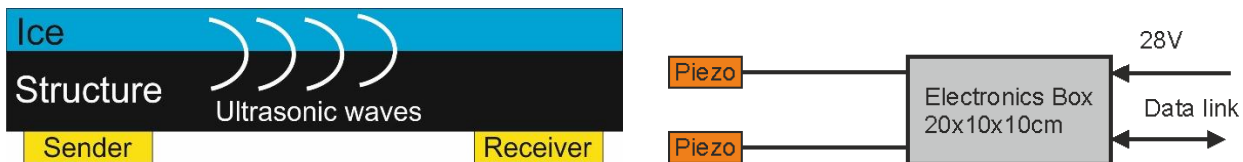


Figure 42: Sensor principle (left) and sensor setup (right).

Aircraft use and mounting

As already mentioned, the mounting location on aircraft is where an ice accretion needs to be detected, as e.g. leading edges as shown in Figure 43. An ice accretion can be sensed and the ice protection system can be activated instantly to remove the ice and prevent further accretion. In addition, the LILD sensor allows a success check of the ice protection system or in the case of electric ice protection systems a modulation of the heating power to prevent ice accretion without using too much excess power thus saving energy.

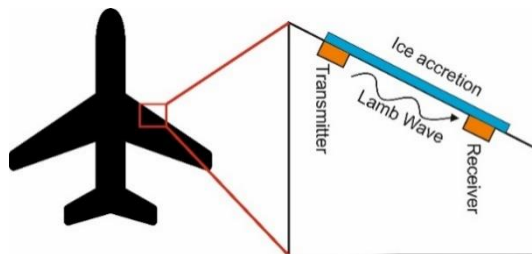


Figure 43: Mounting principle on aircraft.

5.3.2. Technology status at project start

Prior to the SENS4ICE project, the LILD sensor technology had been investigated using laboratory tests on different panel structures where ice was applied by freezing water on the surface. For a more realistic approach, also tests in a small icing wind tunnel have been undertaken on airfoil demonstrators. Both experiments were able to prove the influence of accreted ice layers on the lamb wave transmission behaviour of the tested structures.

For the experiments, standard laboratory hardware had been used, such as function generators for signal generation and computer-based oscilloscopes for signal acquisition. This was suited for feasibility tests of the sensor principle, but is not sufficient for flight testing or further development as an integrated sensor.

5.3.3. Technical Work

The development work in SENS4ICE can generally be grouped into three different main tasks:

1. Design and development of flight test ready sensor electronic hardware,
2. Icing wind tunnel testing and determination of ice induced deviations of wave guide behaviour of the structures,

3. Transfer of obtained wave guide behaviour of test structures into ice detection algorithm and implementation on flight test hardware.

Since lamb waves relevant for the LILD principle are operating within frequencies up to 1MHz, a special hardware has been designed using a combination of a microcontroller and a FPGA to achieve the required sampling speeds. Furthermore, power supply, transmitter amplifier, receiver amplifier and input filters were designed and developed. To analyse the sensor signals, a special algorithm was implemented, which is able to precisely detect amplitudes and travel times of signal pulses also for noisy signals. In a last step, icing wind tunnel tests were undertaken to gain a deeper insight into the wave transmission behaviour of a test structure with the presence and accretion of different ice types and thicknesses.

Prior to the flight test, the real flight test location of the sensor transducers was measured in an icing wind tunnel to investigate the lamb wave behaviour with different ice covers. The data acquired by this test were used to indicate the presence of ice on the test structure in the flight test. More details on the flight test setup can be seen in the flight test paragraph.

5.3.4. Flight Test

For the flight test, a final update of the electronic sensor hardware was done to ensure continued functionality and the operability without the need of an operator besides activation and deactivation of the system. For redundancy and since the space was available in the 19" rack, which was used in the flight test, two individual sensor hardware units were installed. Figure 44 shows the final hardware and the sensor box.



Figure 44: Flight test sensor hardware.

The transducers for the actual ice testing were installed on the right wing. There a pylon was added which carries all atmospheric probes as shown in Figure 45 on the upper left. At this pylon, the transducers are placed on the inside of its leading edge. In the lower part of Figure 45 a photo of the transducers in comparison to one Euro coin is given as well as a photo of the inside of the leading edge. At the places with the red tape, the transducers were mounted with a measurement distance of 30cm.

Due to the small size of the transducers, the sensitive part of the sensor can be placed even in quite tight locations.

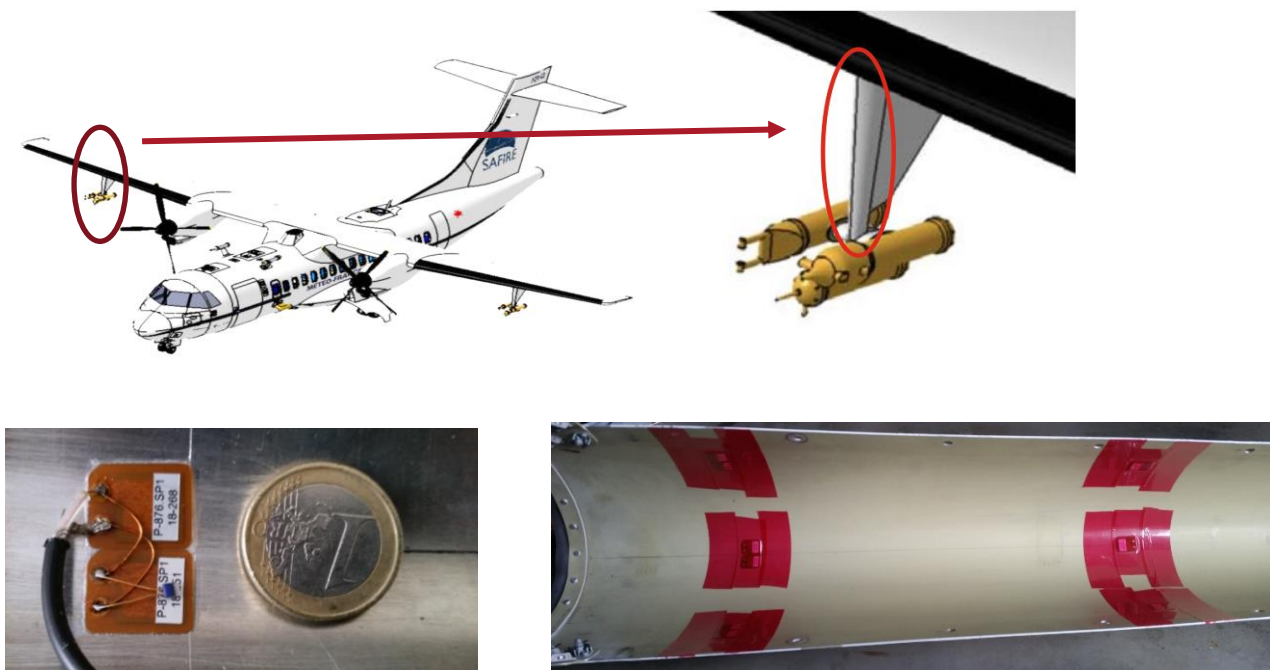


Figure 45: Transducer placement on test aircraft [aircraft image Safire].

During the flight test campaign, two clean air calibration flights and 15 actual test flights in icing conditions were performed. In the calibration tests it was observable, that an amplitude change was happening in clean air which triggered the ice detection. This was found to be a temperature effect of the mounting location of the transducers and could be compensated with the temperature sensors, that were installed in parallel at the transducer locations.

In the icing test flights, a wide variety of different icing conditions could be encountered ranging from very light to heavy. To detect the presence of ice on the aircraft structure, a combination of pulse lag time and pulse amplitude thresholds were used. If one of the thresholds is exceeded, ice is detected on the aircraft. Furthermore, a linear relation was used to calculate the ice thickness on the basis of a lag time increase. With the current state of data analysis, the following conclusions can be drawn:

- The LILD sensor was able to detect an ice accretion in all cases when the aircraft entered the icing conditions with a previously clean airfoil.
- With the current state of the sensor, the main output is the “ice present” signal, which is reset when the ice is removed (e.g. in the flight tests by descending into warm air to melt the accreted ice).
- Reaction time of LILD is very short. The sensitivity to even thin layers of ice, which is already known from the wind tunnel tests, could be confirmed.
- The ice thickness estimation based on the additional lag time is imprecise with the current data since the temperature and shape of the ice layer also have an influence.

As an example Figure 46 shows a diagram of one measurement with the LILD ice present flag together with the icing flag and the static air temperature <0 indication from DLR’s microphysics cloud probes. It can be seen, that LILD always indicates the presence of ice shortly after icing conditions are detected by the microphysics probes. Ice accretion from App C and App O conditions are both detected.

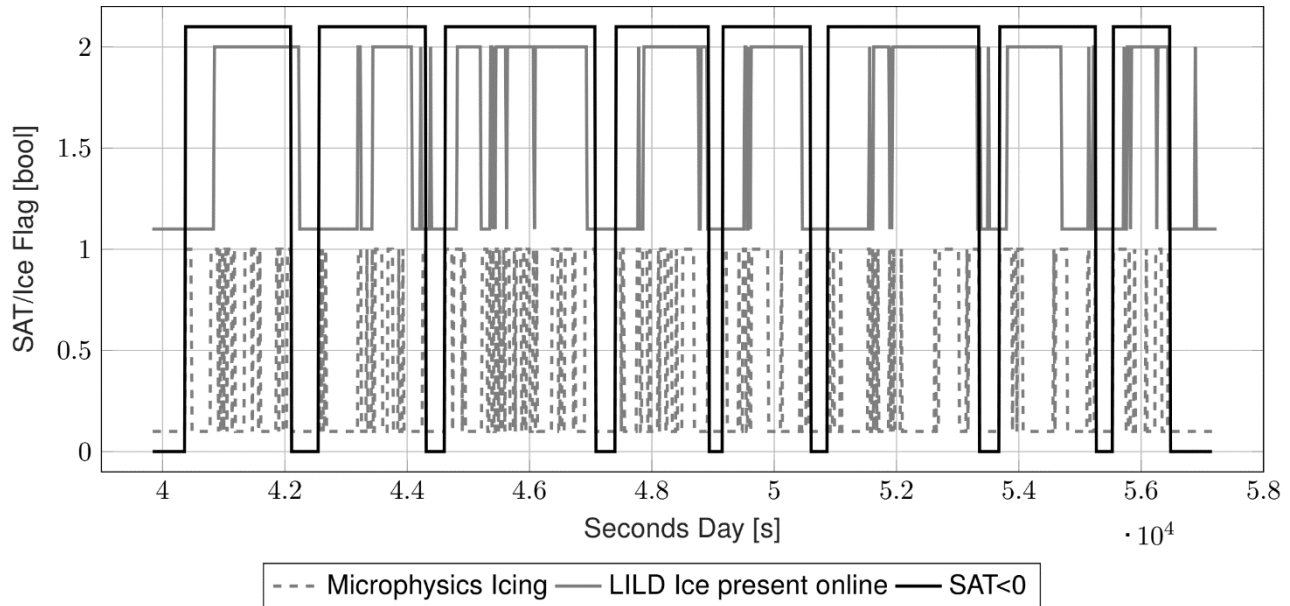


Figure 46: Ice flags of Microphysics (μ P) and LILD with static air temperature.

5.3.5. Current TRL

TRL6 for App. C and App. O ice detection. TRL3 for App C/O discrimination.

5.3.6. Short summary of further development, maturation, and exploitation

Further maturation of the sensor includes the improvement of the detection of the ice thickness foremost. Therefore, additional wind tunnel testing in different temperatures and LWC conditions is needed to create a database for the lamb wave behaviour in these conditions. This will be followed by more sophisticated analysis algorithms with the aim to derive the ice thickness and the accretion rate from the lamb wave data in icing conditions. This information allows an estimation of the LWC and the severity of icing conditions. Secondly, the sensor electronics need to be further miniaturized and improved for e.g. AI analysis, more data channels and faster signal acquisition as well as higher lamb wave signal amplitudes. As a last step, investigations in the simulation of the sensor signals are required to obtain the sensor signals for an application on aircraft without the need for calibration tests on the real structure in icing wind tunnel experiments.

5.4. DLR – CM2D

5.4.1. Technology Description

The CM2D is a combination of two scientific, flight-proven instruments. The CM2D is not developed for commercial aviation, but rather for scientific flights, development within SENS4ICE aimed to enhance the possibilities of precisely measuring SLD conditions.

The two instruments which constitute the CM2D are:

- Nevzorov Hot-Wire LWC/TWC probe,
- Backscatter Cloud probe with Polarization Detection (BCPD).

The Nevzorov probe [10, 12] itself consists of four sensors, two TWC collector cones, an LWC collector hotwire and a reference sensor (see Figure 32). The reference sensor is aerodynamically protected from the impinging droplets and is used to correct the measurements of the other sensors for dry air losses. The Nevzorov probe derives liquid water content from the power that is needed to maintain its sensors at a constant temperature.

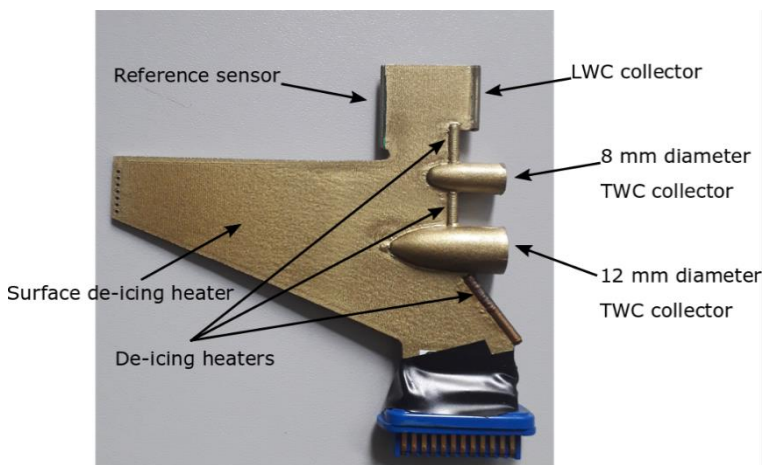


Figure 47: Sensor head of the Nevzorov probe.

The BCPD [11, 13] is a scattering instrument that measures droplet size from the intensity of backscattered light. It incorporates a polarization filter and is thus also able to determine the shape of the sampled particles. By doing so it is able to distinguish droplets from ice (spherical and non-spherical particles). The probe measures particles up to 42 µm.

5.4.2. Technology status at project start

The sensors that constitute the CM2D, the BCPD and the Nevzorov both were flight proven instrument at the start of the project. However, neither of them was able to serve the purpose of detecting and differentiating on its own, which necessitated the combination of the two instruments.

Furthermore, the versions of the instruments that we used for the SENS4ICE project are altered with respect to their precursors. The Nevzorov sensor head features a 12 mm cone that was added specifically for the collection of SLD. The BCPD is an enhancement of the Backscatter Cloud Probe (BCP) that is used in the IAGOS project. Compared to the BCP, the BCPD has the ability to differentiate between spherical and aspherical particles (between droplets and ice). These additional features of the BCPD and the Nevzorov probe had not been characterized at project start.

5.4.3. Technical Work

As both components of the CM2D, the BCPD and the Nevzorov, were already flight proven sensors, no mechanical additions were made to the instruments. However, data acquisition components were added to the Nevzorov system to digitize its outputs and software was developed that allowed live-monitoring of the measured liquid water content.

Further technical work on the sensor system therefore mostly consisted of instrument characterization and algorithm development. The basis of both activities were the wind tunnel measurements that we acquired during the SENS4ICE campaigns. For the Nevzorov, the main activity was the computation of the collision efficiency of the 12 mm cone and an assessment of how the different sensors behave in SLD conditions. Measurements of three different wind tunnels were used for this task and an extensive evaluation and comparison to other LWC instruments was carried out.

The work on the BCPD included theoretical calculations on the droplet sizing of the BCPD. The scattering cross sections for the parallel and the perpendicular components of the scattered light were computed, which allows us to define the polarization ratio of spherical particles (see Figure 48). Ice crystals exhibit scattering cross sections that deviate widely from the expected value for spherical droplets, allowing for a differentiation between ice and water.

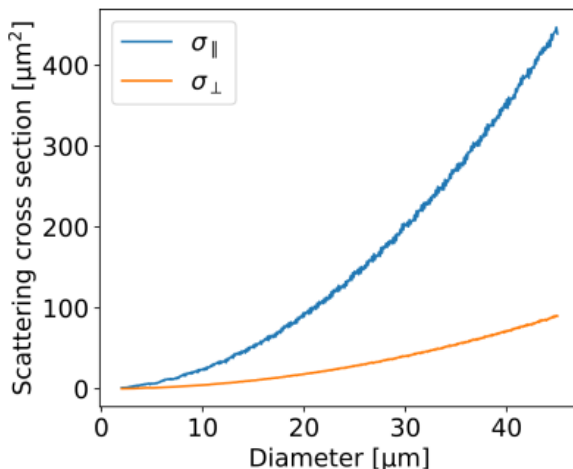


Figure 48: Scattering cross sections for the parallel and the perpendicular component of the backscattered light from droplets of a given diameter.

On the basis of these findings, an algorithm was developed, that allows us to estimate the number of spherical and aspherical particles detected by the BCPD. This algorithm allows us to assess the cloud conditions, i.e. whether the aircraft flies through a purely supercooled cloud, a mixed-phase cloud or a pure ice cloud.

Furthermore, our characterization of the BCPD also showed, that a correction for undersizing of particles that pass through the fringes of the sample area is required, due to an uneven distribution of the laser intensity across the sample area. We implemented such an algorithm and tested it in comparison to reference measurements from a Cloud Droplet Probe (CDP). Extensive testing was required to optimize the algorithm.

Lastly, from the output of Nevzorov and BCPD an algorithm was developed that to detect and differentiate between Appendix C and O. This algorithm is further explained in the following sections of this document.

5.4.4. Flight Test

DLR tested the CM2D and the individual components of the CM2D during several flight campaigns (see Table 7). During the Cirrus-HL campaign, just the BCPD component was integrated into a side window on DLR's HALO Gulfstream 550 aircraft. The campaign focused on high-latitude cirrus clouds, but we were also able to obtain some data in low level and mixed-phase clouds. In the high cirrus clouds, the response of the CM2D to ice particles could be established. App. O conditions were not encountered during Cirrus-HL.

Both components of the CM2D were flown during the HALO-AC [11] campaign on the Polar-6 aircraft of Alfred-Wegener Institute. The campaign focused on Arctic mixed-phase clouds. Numerous icing conditions were encountered, but no App. O conditions. The data from the campaign allowed us to develop the algorithm for estimating the number of liquid and ice particles. On the basis of that algorithm, we are able to distinguish, pure ice, mixed-phase and supercooled clouds. The differentiation between the three types of clouds is however somewhat fluid and depends on the definition of mixed-phase clouds (e.g. what is the minimum number of ice crystals that need to be present in a given volume for a cloud to be considered mixed-phase). For the CM2D, the minimum ice particle concentration that can be detected is approximately 0.01 g/m³.

Table 7: Flight testing of CM2D components.

Time	Campaign name	Location	Components tested
24.06.2021-30.07.2021	Cirrus-HL	Oberpfaffenhofen, Germany	BCPD
14.03.2022-13.04.2022	(AC) ³	Longyearbyen, Spitzbergen	Nevzorov + BCPD
03.04.2023-27.04.2023	SENS4ICE	Toulouse	Nevzorov + BCPD

Finally, the CM2D was tested during the European SENS4ICE campaign, where a large number of App. O conditions were measured. The installation of the two instruments on the aircraft can be seen in Figure 49. Both instruments were mounted on the side of the fuselage, several meters behind the aircraft nose. The position of the instruments was mostly dictated by availability. The DLR team would have preferred a position further towards the nose of the aircraft for the BCPD, in order to reduce the influence of the fuselage on the measurement, but no such position was available.



Figure 49: Nevzorov probe and BCPD integrated on the SAFIRE ATR-42 aircraft during the European SENS4ICE campaign [image DLR / SENS4ICE project].

We tested the algorithm from Section 5.4.3 on the flight data. However, it was observed that the BCPD sample area lay in a region close to the fuselage where the airflow was strongly altered. The MVD measurements of the BCPD were thus deemed to be unreliable. A reduced version of the algorithm that was developed for the HALO-AC³ campaign that relies solely on the ratio of the Nevzorov measurements was used to distinguish App. C and App. O conditions. App. C and O conditions can be distinguished with the CM2D, if a large number of large droplets is present and if the App. O conditions are relatively homogeneous. This can be seen from Figure 50. The three-minute long App. O encounter at approximately 14:33 is accurately detected by the CM2D. The shorter encounter at approximately 14:14 is missed, because the presence of ice crystals was detected. SLD and ice crystals both cause a decrease in the ratio between the LWC sensor and the TWC sensors of the Nevzorov probe. If ice crystals are present in the BCPD data, the decrease in the LWC sensor to TWC sensor ratio of the Nevzorov probe is assumed to be due to these ice crystals. Conditions where both SLD and ice crystals are present can therefore not be differentiated with the BCPD.

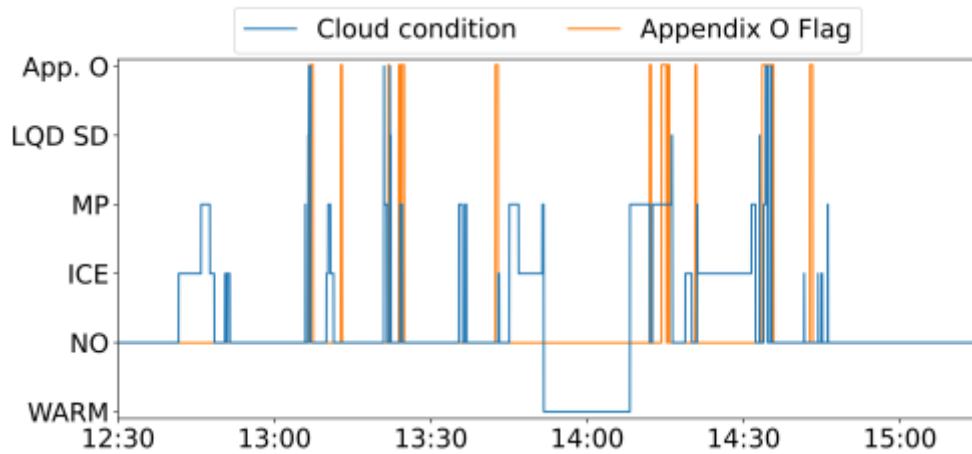


Figure 50: Cloud condition detected by the CM2D (blue) and App. O indication from the reference data (orange).

5.4.5. Current TRL

Both BCPD and Nevzorov probe are TRL5.

5.4.6. Short summary of further development, maturation, and exploitation

The CM2D is designed to serve as an indication for icing conditions on research aircraft. The advantages of the CM2D over classical underwing particle measurement probes is, that the combination is lighter and can be integrated directly into the fuselage. The maturation of the Nevzorov part of the CM2D can be considered as mature, as the collision efficiency of the 12 mm cone was assessed within SENS4ICE and the LWC sensor and the 8 mm sensor are already well characterized in the literature. For the BCPD component of the CM2D, further work after SENS4ICE is required. This work should focus on extending the sample area of the BCPD outwards and resolve remaining differences between the number concentration and MVD measured by the BCPD and reference instruments.

5.5. HONEYWELL – SRP

5.5.1. Technology Description

The SRP (Short Range Particulate) sensor is an optical sensor based on collecting backscattered light from individual particles in the environment directly outside of the aircraft skin as shown in Figure 51. Using this particle-by-particle measurement, the sensor measures the overall particle size distribution, which are then used to derive the total number concentration, liquid water content (LWC), and median volume diameter (MVD). Using the size distributions, the sensor will discriminate between App. C and App. O. In the current SENS4ICE design, the sensor will not be able to detect the entire App. C envelope.

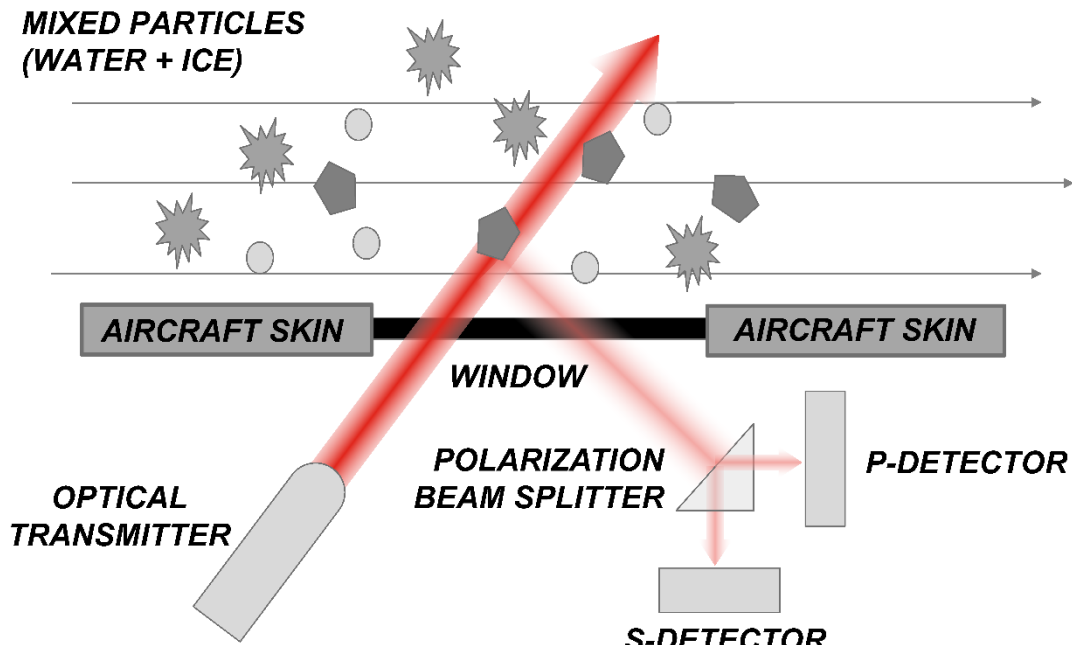


Figure 51: Flush mounted sensor optical design.

5.5.2. Technology status at project start

Honeywell will expand on its existing SRP sensing technology which was in TRL5 phase. This sensor currently detected App. C icing conditions and needed technology development in order to detect App. O icing conditions, particularly the larger end of size distribution. The existing sensor has been flight tested across several aircrafts in a wide range in flight conditions.

The SENS4ICE SRP sensor was in TRL3 phase. Some preliminary optical design and trade studies for detecting App. O conditions were completed in 2018 ahead of the SENS4ICE project. These studies were aimed at first to determine the appropriate sample area, laser power, and photodetector parameters to meet expected App. O conditions. Following this, a preliminary optical layout was designed and evaluated.

5.5.3. Technical Work

The preparation phases for each test (IWT, flight test) were split into development and integration phases.

IWT preparation phases were outlined as:

- A) **Development Phase** (2019): design and assembly of the SRP sensor. This phase is further split into:
 - a. **Preliminary Design** (3 months): system requirements and architecture definition, trade studies on main components, function definitions for software / firmware.
 - b. **Detailed Design** (5 months): opto-mechanical design, circuit schematic design and simulation, PCB layout, electronics housing design, firmware design, software prototype implemented.
 - c. **Manufacturing & Assembly** (6 months): manufacture of the sensor components (PCB, optical head, mechanical boxes), components functional check and assembly of sensor sub-systems.



- B) **Integration phase** (2020-2021): perform system integration, calibration, and testing of the SRP sensor. This phase is further split into:
- System Integration, Checkout, and Design Updates** (8 months): final system assembly and basic functionality checks. Issues identified and corrected with updated designs.
 - Sensor Calibration** (3 months): calibrate the system for size and particle density measurements.

IWT was carried out in Collins and NRC facilities with good results, however there were also several areas for improvement identified. Flight test preparation started after the IWT testing results were reviewed and all the ideas for improvement captured. In cooperation with the Embraer Flight Test department, requirements for aircraft installation were generated. Flight test requirements and IWT findings were condensed together resulting into following design changes:

- Electronics box
 - Decrease footprint to the half of the current size
 - Update temperature control for increased robustness
 - Update laser power control to enable automatic operation of the laser with flight conditions
- Optical head
 - Updates to the optical sensing parameters
 - Re-Calibration of the sensor
- Software
 - Live data processing and stand-alone functionality implementation
 - Communication with aircraft systems implementation
- Testing
 - Safety Of Flight testing - both Electrical (Power, Emissions) and Environmental (Temperature, Vibration) tests per DO-160G standard were required

After the implementation of all the hardware changes and integration tests, SRP prototype was tested for the set of DO-160G tests. All the test results were considered as pass and therefore SRP prototype was claimed to be safe for installation into the aircraft. After the bailment agreement contract was negotiated, the sensor was shipped to Brazil and integrated to the Embraer Phenom 300. Shakedown tests were performed by Embraer and then the aircraft was moved to Saint Louis Regional Airport (state Illinois, United States of America), where the icing flight test campaign took place. Except of SRP sensor, the aircraft carried ice detection sensors manufactured by other companies and Cloud Combination Probe which provided measurement of icing conditions reference data.

5.5.4. Flight Test

The flight test campaign took place from February 19 2023 to March 10 2023, thirteen flights were performed and for eight flights icing conditions were encountered while SRP sensor data and reference instrumentation data were successfully collected. The flights were performed in the airspace of the following states: Illinois, Indiana, Ohio, Michigan, Iowa and Wisconsin.

There were several App. C and App. O condition encounters during the icing campaign, which allowed us to evaluate performance of SRP sensor for various levels of LWC and various particle size distributions. After the icing campaign, DLR Institute of Atmospheric Physics performed reference data analysis and applied corrections to increase reference data measurement accuracy. The comparison of SRP sensor measurements with the reference probe measurements is shown in Figure 52 and Figure 53.

SRP sensor performance evaluation summary:

- The sensor successfully performed icing condition measurement over the whole flight campaign
 - Sensor optical parameters were not affected by the environmental conditions
- Sensor measurement accuracy
 - For events in which particulate MVD > 25 microns, there is very good correlation between SRP sensor LWC data and reference sensor LWC data
 - For events in which particulate MVD < 15-20 microns, the measurement accuracy is poor as the SRP sensor design developed under SENS4ICE does not cover the whole App C



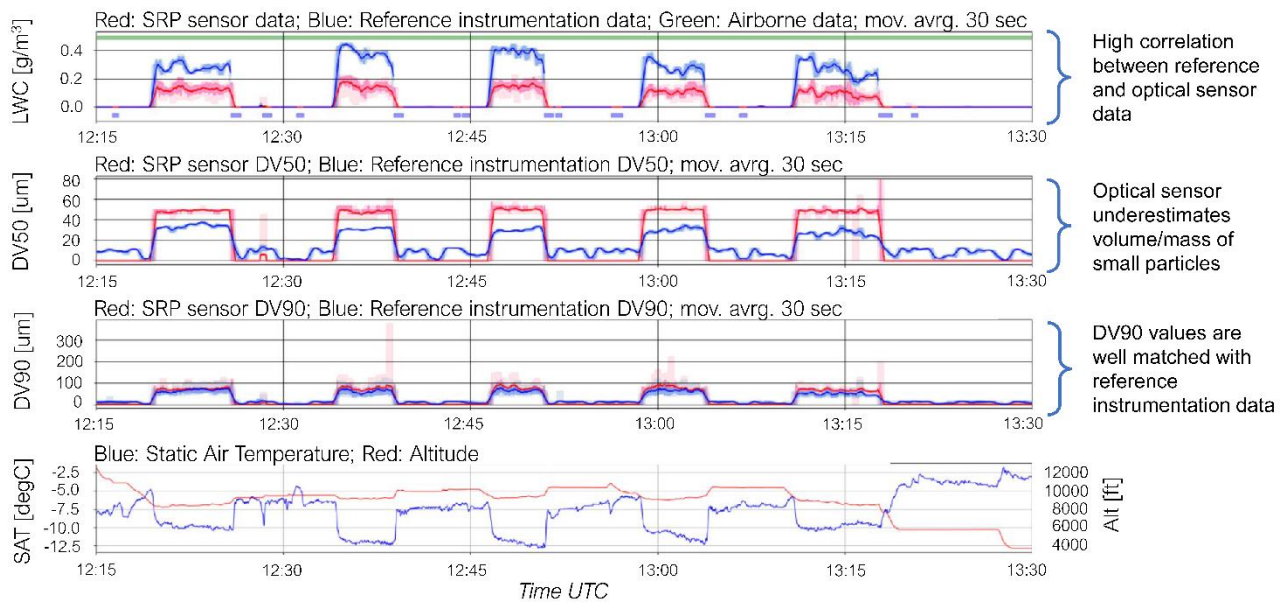


Figure 52: Optical sensor data analysis: Flight 1476.

(No collection efficiency corrections applied, sensor non-linearities corrections not applied, better results are expected)

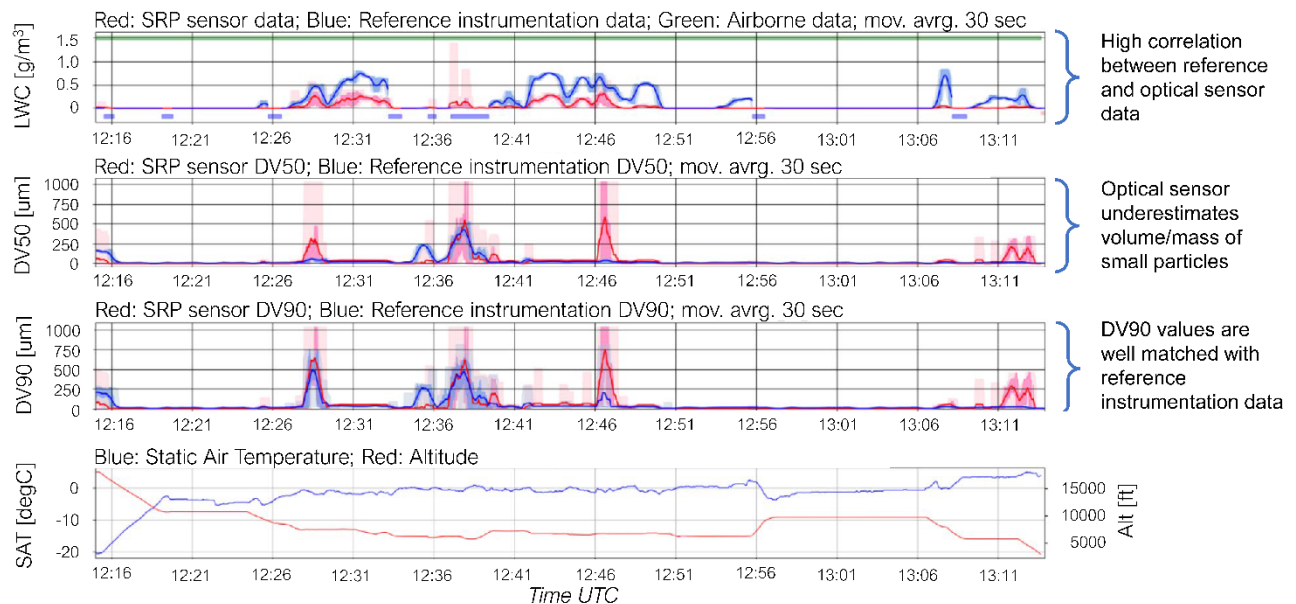


Figure 53: Optical sensor data analysis: Flight 1481.

(No collection efficiency corrections applied, sensor non-linearities corrections not applied, better results are expected)

5.5.5. Current TRL

The technology maturation goal was to leverage the App. O sensing technology to TRL6 which was confirmed by TRL assessment in the project internal document D6.3 Interim Catalogue of results and IP register after successful IWT testing.

5.5.6. Short summary of further development, maturation, and exploitation

Honeywell plans to develop the SRP sensor beyond SENS4ICE into a single commercially available sensor capable of detecting all forms of liquid water icing conditions (both Appendix C and O), as well as extending the measurement capabilities to ice crystals in order to cover all icing appendices (Appendix D/P). Currently, the expected entry into service date of such sensor would be in the 2028/ 2029 timeframe.



5.6. INTA – FOD

5.6.1. Technology Description

The Fiber Optic Detector (FOD) is a latent energy-based ice sensor. The latent energy released by the water during the phase change produces an abrupt temperature increase in the surface where ice is accreted. That temperature rising is a function of the icing cloud conditions, so the FOD can assess the ice severity in an approximate way.

The technology consists in an Optic Fiber embedded in a sensor surface. The fiber should be close to the sensor surface so the energy flux rate could be measured conveniently. The optic fiber has, all over its length, equispaced Bragg gratings with an eight millimetres separation, that back scatter the light in certain wavelengths. The wavelengths in which it backscatters the light are function of the temperature of the fiber. In a single fiber many temperature points could be measured. If the optic fiber is placed on the sensor surface, the temperature differences in several points on surface could be measured.

The sensor technology has two main capabilities:

- a. Ice detection: The ice detection is done measuring the temperature changing abruptness. The chosen temperature is the difference between a detection grating and a reference grating that is not exposed to liquid water. The sensor first detects ice and then, using the temperature data assessed if there are Appendix O conditions depending on the impingement limits.
- b. Ice severity assessment: The ice severity assessment relates the temperature rising of the sensor line and icing cloud conditions. First of all, a sensor is used for calculating the ice accretion rate in a reference sensor (located on the probe stagnation point) and the rest are used for calculating the accretion all over the chord. With the relationship with the stagnation point sensor and the rest the droplet size could be calculated. In order to do that process, a standard airfoil (NACA 0012) was used.

For more information see references (M. Gonzalez, 2022) (Miguel González del Val, 2021).

Thermal Model: Ice Assessment

In order to predict the external conditions a thermal model was used. The model solves a heat transfer equation of this type:

$$q_{lat}^{node} - q_{evap}^{node} \pm q_{sens}^{node} + q_k^{node} - q_{nc}^{node} = 0$$

Being the first term q_{lat}^{node} the latent flux energy flux, the second term q_{evap}^{node} the evaporate heat flux, the third term q_{sens}^{node} the sensible heat flux, the fourth term q_k^{node} the kinetic energy heat flux and the last term q_{nc}^{node} the net convective heat flux. In case of rime conditions and solving the last equation, the Ice Accretion $d\Delta/dt$ rate could be calculated. The App. O and App. C discrimination could be assessed with the differences between the icing accretion profiles as it can be seen in Figure 54.

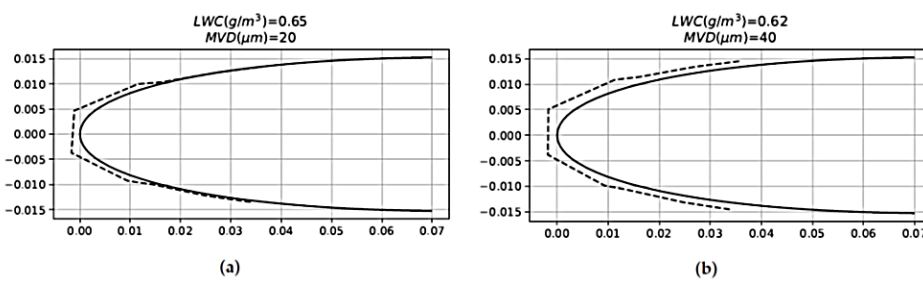


Figure 54: Sensor ice accretion profile predicted by the sensor.

Ice detection technology

At the beginning of the project, the icing detection technique used the temperature rising abruptness that was calculated from the first temporal derivative of the temperature difference between a reference sensor and the detection sensor. This method was seen to require a lot of computational time, because firstly a filter and then a finite difference method has to be used. Later, Discrete Wavelet Transforms (DWT) were implemented in the detection algorithm. DWT do the filtering and the ice detection simultaneously. For more information about the



algorithm, reference (M. Gonzalez, 2022) is recommended. Another advantage that presents the DWT is its capabilities to reduce the data size, so gives IAR and icing cloud parameters with logical sample rates (sampling time of 3 seconds).

The discrete coefficients above a certain threshold that is calculated from test data are considered ice. The threshold has to be function of external parameters like airspeed or total temperature, so it maximizes the sensibility of the sensor and minimizes its specificity.

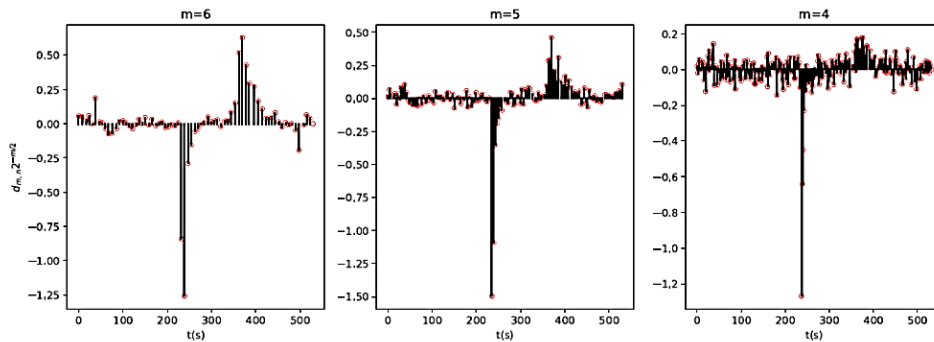


Figure 55: DWT coefficients of the sixth, fifth and fourth levels.

5.6.2. Technology status at project start

Before the project started a previous study was done, only in order to see if the FBGS detected a droplet supercooled water freezing. The wavelength of the water droplet freezing was recorded. For a droplet freezing, a temperature peak was seen. The process of a droplet freezing is very fast, and the energy release is discrete so this principle could not be applied for a water flux impinging an airfoil surface.

A very preliminary airfoil was prepared with a few layers of composite material and foam to give consistency to the geometry. This configuration was tested in the INTA IWT as well, seeing a certain pattern of signal. INTA IWT was not prepared for icing sensor tests. One of the things that was done was conditioning the Icing Wind Tunnel and the testing process in order to simulate realistic icing conditions. FOD is very influenced by the transitory conditions in the start of the icing cloud.

The results of the preliminary testing only detected ice without discriminating between Appendix C and O conditions. Additionally, the conditions could not be predicted neither. The main goal of those preliminary tests was only giving a very straightforward detection output (ice/no ice). Detection algorithms were not implemented previous to the project start.

5.6.3. Technical Work

The development of FOD during the project had six different steps. The first one was researching about the relationship between the physical thermal events and the sensor response. Then, a sensing probe was designed firstly for INTA IWT testing and then for NRC testing. Later, the software of the sensor was developed, in order to assess severity, discriminate between Appendix C and O and detect ice very fast for the NRC testing. The testing results of NRC IWT were studied and all the algorithms were adapted for all conditions that were tested. The performance of the NRC tests was studied and the detection parameters were optimized.

Lastly, all the work done in order to prepare the sensing probe for flight test. This includes the DO-160 testing, the communication design for flight tests, the software development in order to be adapted to the new conditions and the postprocess of the sensor data. A new detection algorithm was done in order to detect the real icing clouds with its instabilities.

5.6.4. Flight Test

For flight tests a new icing probe was designed, according to the DO-160G and with a different material and design than the previous one. The probe had a larger span than the previous one, so the bigger droplets can impact the probe surface. The used material was ULTEM® that is a very high resistance polymer and was fabricated with additive manufacturing, because it was considered the easiest solution for the proposed design. The used airfoil was the same than before, a shorten NACA 0012 with a better aerodynamic design in the tip.



After placing two fibers in the sensing probe, it was painted with a polyurethane painting. The sensing probe was previously tested in INTA IWT so it could be seen if all the system worked well, including detection algorithm, communication, and data acquisition.



Figure 56: INTA-FOD flight test direct sensing probe installed in the left side fuselage of the aircraft [images INTA/ SENS4ICE project].

In the case of flight tests, a different behaviour of the icing cloud was seen compared with IWT tests. In the IWT tests the icing cloud had a very good temporal stability, so it was easy to detect when the sensor entered the cloud and when it left it because inside the icing cloud there was only two temperature abrupt changes. In the case of inflight clouds, the LWC is quite unstable, so the previous assumptions cannot be made, due to the amount of temperature changes recorded in the FBGS when the aircraft goes in an icing cloud. This makes a noisier behaviour in the Discrete Wavelet Transform and in the FBGS signal. Other detection alternatives were considered. The first one is considering the standard deviation of the discrete detail coefficients during an interval of time (during fogging the amplitude of the DWT signal is higher but it has not a very big peak). Other solution is establishing a lower threshold and a lower DWT level and just considering the ice presence when there is a peak.

For IAR or LWC detection it was different. IAR values were postprocessed after the flights, but it is difficult to compare those values and check if they are right because ice thicknesses were not measured during the flight. Even though there are inaccuracies in the case of LWC measurement because the freezing fraction is unknown a priori, Liquid Water Content could be compared with other sensors data Nevzorov for example. The majority of the flights were done close to the 0°C isotherm, so glaze conditions, with freezing fraction different than one, were present, making more inaccurate the LWC results. In Figure 57 can be seen the LWC measured by the FOD and Nevzorov. It can be seen that even when there is LWC present if the total temperature is higher than 0°C FOD does not detect ice so, sometimes Nevzorov measures LWC while FOD LWC output is zero. Many times, there was LWC that was not supercooled, so the probe only detected a cooling effect without a latent energy release.

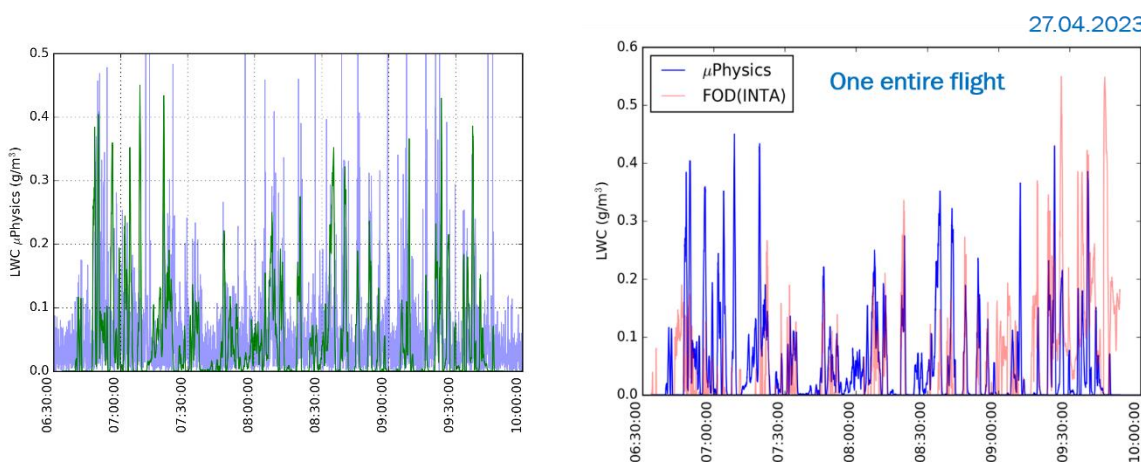


Figure 57: FOD measured LWC compared to Nevzorov.

The App. O and App. C discrimination is being studied comparing the microPhysics data and the temperature data along the chord. It has been seen that, according to microPhysics data, depending on the MVD, there are more or less sensors that accreted ice. There are other factors that affect the number of sensors that

experience a temperature rising in the sensors located downstream the leading edge, like angle of attack or true airspeed, so a more detailed study must be made.

Finally, it was seen that during the de-icing of the probe, there is an effect that can help to know if there is an ice layer accreted, and where the ice was formed. The ice is a good thermal insulator, so the temperatures in the sensors where the ice was not accreted change faster than the others. When the aircraft descents under the zero isotherm, the sensors without ice measure more than 0°C but the other ones measure temperatures much lower. In the moment when the ice layer is removed, the temperature rises drastically because the temperature of air is much higher than the surface temperature. That abrupt temperature rise is due to the convection heat that is proportional to the temperature difference between the surface and air. Previously that abrupt temperature rise, the temperature was stable in a value lower than 0°C that is the fusion temperature. That makes sense because when the ice is changing of state the temperature is constant. This physical effect could be used in systems that want to integrate a de-icing and sensing system in order to know when the ice layer is removed and stop the heating power.

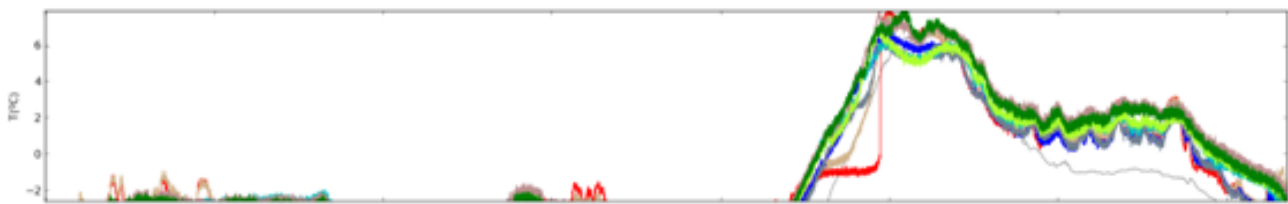


Figure 58: Probe de-icing (flight 27 April 2023).

5.6.5. Current TRL

The TRL depends on the type of detection that is considered. According to the TRL definitions in the SENS4ICE project:

- Appendix C detection: A prototype was built and tested in NRC IWT with more than 5 conditions. Additionally, environmental tests were carried out according to DO-160. Flight tests were executed so TRL6 was achieved.
- Appendix O FZDZ detection: Several conditions in FZDZ were tested in NRC IWT. The ice detection ratio was very high but the discrimination between FZDZ and Appendix C conditions was not enough in order to ensure a TRL6.

5.6.6. Short summary of further development, maturation and exploitation

The sensor needs some maturation in some aspects in the aerodynamic design. A further study that relates the collection efficiency with the sensor geometry must be done in order to maximize the performance. The optic fiber gratings distribution is not optimized either.

The sensor has a saturation ice thickness in which the sensor does not work. A de-icing system must be developed if it is wanted to measure ice constantly. Additionally, it can exist the possibility of a more feasible Appendix O discrimination if a de-icing system is used. Another aspect that must be done is the optimization of the de-icing cycles in order to maximize the sensor performance. The optical interrogator that was used in this project was of a very high quality and precision. A cheaper optical interrogator with lower size could be used.

For its exploitation, some companies in the aeronautical sector have been contacted. The sensor has been patented, and the advances and research have been published in scientific, technical journals and in conferences like SAE's International Conference on Icing of Aircraft, Engines, and Structures. The department of technology transfer in INTA is working in exploiting the technology in different fields like energy distribution, aeronautics, wind turbines or railway transport.

5.7. ONERA – AHDEL

5.7.1. Technology Description

The AHDEL sensor is based on the charging of the droplets by a corona discharge, followed by the detection and measurement of their electric charge, allowing the inference of the particle diameter. The sensor is composed of three main sub-systems: a droplet size discriminator, a droplet charging system and a droplet electric charge detector. Figure 59 illustrates the charging and the detection principles.

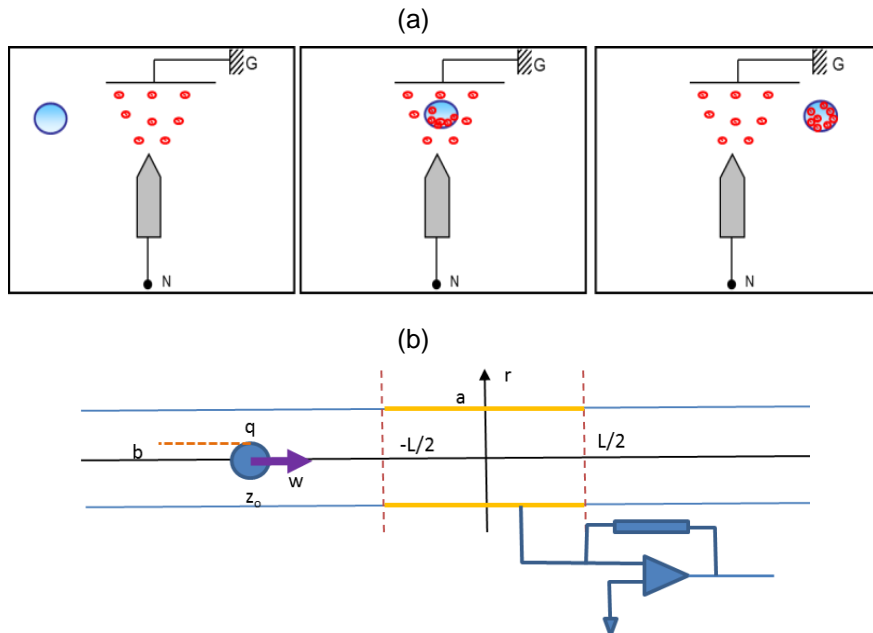


Figure 59: (a) Diagram of the electrical charging of a particle when crossing electric charges created between two electrodes (N and G). (b) Measurement of particle's electric charge (q) by an inductive ring of radius a and length L . This ring is connected to an electronic circuit that amplifies the inductive current.

The purpose of the charging system is to produce enough electric charges to charge the droplet to its saturation value, which is a direct function of the droplet surface (and consequently the droplet diameter squared). It consists of one high voltage electrode designated N and a grounded electrode G integrated in the sensor body. This subsystem generates a corona discharge between N and G, creating a cloud of electrical charges in the medium. When the droplets enter the region of corona discharge, they collect the electric charges drifting between N and G.

The detection system measures the droplet electric charge using one or several capacitive rings integrated in the sensor body. This subsystem generates electric signals that are function of the electric charge carried by the droplets. The shape of this signal is a function of the ring geometry and the particle speed, but its integral should be only function of the particle charge.

For the droplet size discriminator, two filters are evaluated, one based on inertial principle and other based on electrostatic principle. The inertial discriminator is located upstream of the charging chamber. Using the internal sensor geometry, it filters the small particles that are driven by the flow and keeps only large droplets. The latter reach the charging-detection zone. The electrostatic filtering takes place along the charging zone. In an axisymmetric corona discharge, charged droplets experience an outward radial force which increases near the corona wire. Heavier (larger) droplets will be less deflected than lighter (smaller) droplets. As a consequence, a collection electrode located near the detector axis only collects droplets which have not been significantly deflected. By changing either the intensity of the electrostatic force or the location of the detector, different classes of droplets can be detected and quantified.



5.7.2. Technology status at project start

The AHDEL sensor started the SENS4ICE project from a very low TRL (between 1 and 2). At the beginning of the project, we had just formulated the concept based on a few previous lab supporting experiments for the charging system and from the experience on the development of on-board sensors for atmospheric characterization in previous projects. The detection system, which is based on an induction ring, had already been designed to measure the electric charge carried by the droplets inside thundercloud. This system was installed on a Transall C-160 aircraft for thunderstorm and lightning characterization campaigns [Lalande *et al.* (1999), Laroche *et al.* (2012)].

5.7.3. Technical Work

During the SENS4ICE project, we realized an extensive work in the development and optimization of the sensor technology through numerous simulations and lab tests for the different sub-systems individually, leading to the design and implementation of two sensor versions. In the preparation of IWT tests, the prototypes were tested and calibrated in ONERA's lab using droplets up to 600 µm with velocities up to 25 m/s at room temperature. These preliminary tests helped to verify the efficiency of the discriminator system to filter the droplets and reduce the particle concentration in the detection zone. The two AHDEL versions were tested in IWT at TUBS in June 2021. In the IWT testing, we performed a few points of the SENS4ICE test matrix for low water density and we explored many additional academic points to a better evaluation of the sensor capabilities and limits.

5.7.4. Ice Wind Tunnel Tests

The IWT testing for AHDEL sensor was performed in the first week of June 2021. The two AHDEL versions, one based on electrostatic and other on inertial principle were tested in IWT at TUBS. We started the test campaign with the points of the SENS4ICE test matrix, both in App. C and App. O conditions, for points with low water density, respecting the SENS4ICE test procedure for IWT. We were able to test 4 points of App. C and 4 points of App. O. Once the water concentration increased ($LWC > 0.6 \text{ g/m}^3$) we had unexpected problems with water accumulation in the charging system that led to a short circuits. This rendered the charging system inoperative. In addition, in these higher densities conditions, we noticed ice accretion in some internal parts of the model. After a few minutes (3 to 5 minutes), the icing was enough to block the detector zone entrance, making this subsystem also inoperative. These were conditions (low temperature and a large water concentration) that we were not able to reproduce in our lab during the preliminary testing of the sensor.

However, we opted to conduct academic tests to gain a deeper understanding of the sensor's performance and limitations. To achieve this, we explored supplementary test parameters beyond those outlined in the SENS4ICE test matrix. We conducted a series of sweeps across various parameters, each lasting approximately 5 to 10 minutes. Throughout these testing runs, we executed multiple 30-second ON-spray cycles. Within each cycle, a single parameter—such as LWC, MVD, temperature, or flow speed—was altered. Through this parametric study, we examined approximately twenty additional data points. Figure 60 and Figure 61 display the graphs showcasing the sensor results, alongside comparisons highlighting the required response time and IWT values for LWC and MVD. Table 8 summarizes the results obtained from the tested points.



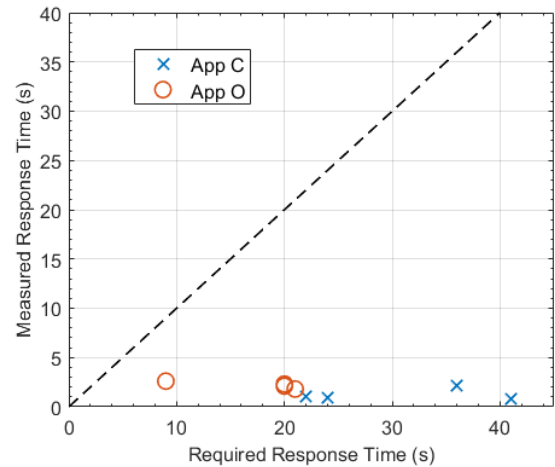


Figure 60: Graph showing measured vs required response time for all test in the SENS4ICE matrix (8 points). All the points below the black dashed line indicate a response time that met the requirements.

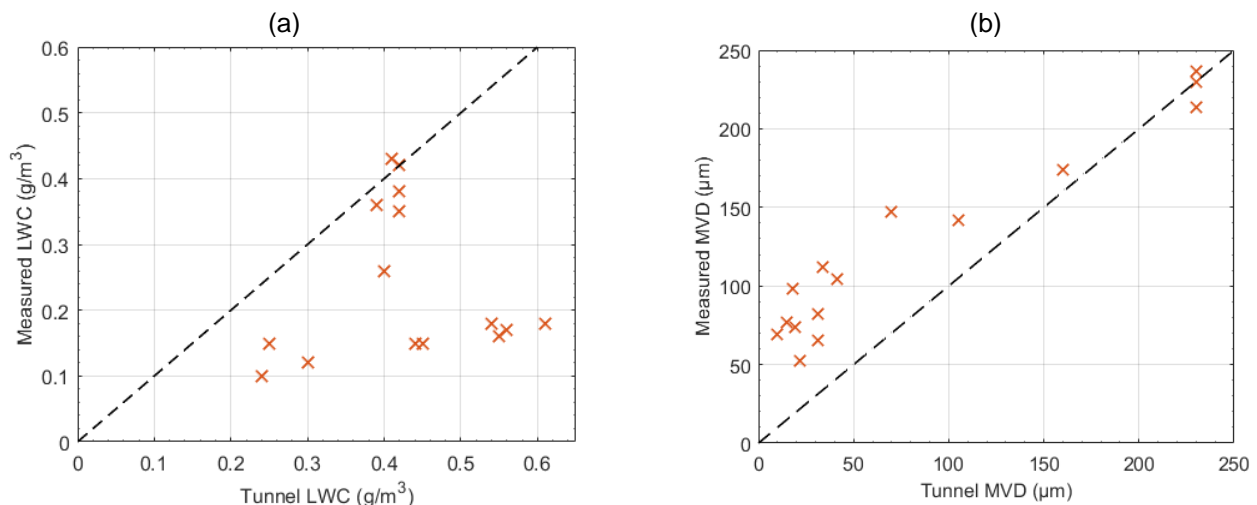


Figure 61: Graph showing measured vs tunnel LWC (a) and MVD (b) for the tested points concerning SENS4ICE matrix and academic runs. All the points below (above) the black dashed line indicate a measured LWC/MVD underestimating (overestimating) the calibrated tunnel values.



Table 8: Results summary table, including the standard and academic test points (AHDEL sensor).

Test	Percentage of Test Points Detected	Percentage of Test Points Within Required Response Time	Percentage of Test Points with MVD Measurement	Percentage of Test Points with LWC Measurement	Average MVD Error	Average LWC Error
App. C Test Points	100% ¹	100%	100%	100%	185%	59%
App. O Test Points	100% ²	100%	100%	100%	170%	70%
Academic runs	100% ³	100%	100%	100%	17% ⁴	27% ⁵

5.7.5. Flight Test

As the necessary modifications and improvements to perform a successful aircraft flight test were not compatible with the remaining time and resources in the SENS4ICE project, the ONERA team decided, by end of June 2021, to withdrawn AHDEL sensor from the SENS4ICE flight tests.

5.7.6. Current TRL

ONERA validated the different subsystems separately, and then integrated these into two different prototypes, based on two discrimination principles, which we tested in the TUBS IWT. The AHDEL sensor presented a good performance in terms of response time and LWC/MVD estimation, having a response time around 1 s for the entering and exit of the icing condition detection and within 20% error on MVD estimation for high MVD cases. We consider that the AHDEL technology has reached an intermediary TRL between 3 and 4.

5.7.7. Short summary of further development, maturation and exploitation

The feedback of the IWT campaign provided us several ideas and inputs for improvement of the AHDEL technology. In further activities, we expect to solve the different problems related to the insulation of charging system and on the anti-icing of internal part. In general, it includes the modification of the sensor systems, as well as the performing of new IWT testing to continue the development and maturation of AHDEL technology, having as main purpose the achievement of a reliable and robust on-board direct detector of App. O conditions and able to perform scientific flight campaigns in future projects.

¹ Only 4 out of 19 App. C test conditions were tested from the SENS4ICE test matrix. This is due to unexpected problems with water accumulation in the high-voltage when LWC >0.6 g/m³.

² Only 4 out of 18 App. O test conditions were tested from the SENS4ICE test matrix. This is due to unexpected problems with water accumulation in the high-voltage when LWC >0.6 g/m³.

³ Seven academic runs with calibrated tunnel conditions were realized.

⁴ Only points with MVD > 25 µm are considered in this average error.

⁵ Only points with MVD > 25 µm are considered in this average error.



5.8. ONERA – AMPERA

5.8.1. Technology Description

When an aircraft flies inside a cloud, atmospheric particles (droplets, ice crystals ...) run into the fuselage. The particle impacts lead to electric charge exchanges through a **triboelectric process** as illustrated in Figure 62. These electric charges on the aircraft fuselage produce an electrostatic field on the metallic part of the airframe.

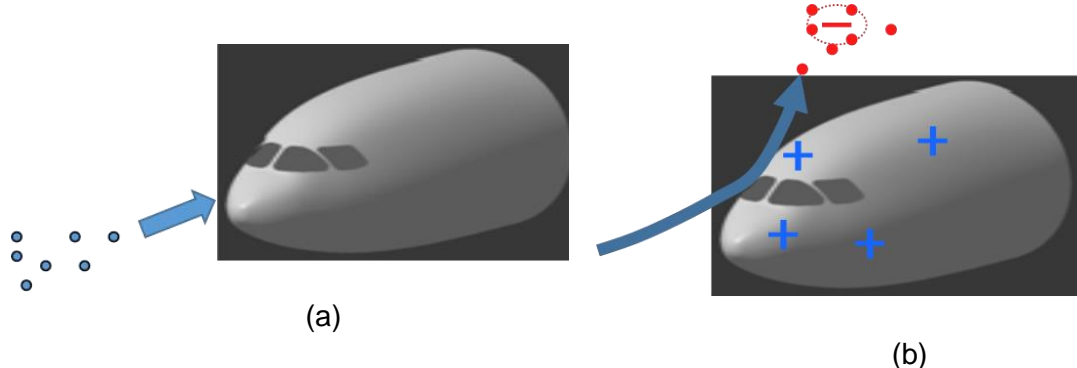


Figure 62: Illustration of the aircraft charging process due to particle impacts. (a) Before impacts and (b) after impacts.

AMPERA system is an electric field mill (EFM) network that **locally measures the electrostatic field at the surface of the aircraft fuselage**. The distribution and amplitude of the electrostatic field on the aircraft skin depends on the atmospheric electrostatic field around the aircraft and the net electric charge of the aircraft. This latter parameter depends on the balance between the triboelectric current due to the impact of the cloud particles on the aircraft fuselage, the current due to the charged particles emitted by the engines, and the corona current emitted by the aircraft through the static dischargers. In contrast to conventional TWC probes, which sample a local area of the atmosphere, the AMPERA system uses the entire aircraft as the sensitive part, providing an overall estimation of the net TWC exposure. Therefore, the sensor in its current version is not relevant for IWT tests.

Figure 63 shows a strong correlation between the time evolution of the aircraft electrostatic potential (net electric charge of the aircraft divided by the electric capacitance of the aircraft) and the time evolution of the TWC measured by the IKP2 probe during a flight of the HAIC campaign [14]. The results of this campaign showed that the sensor

could not discriminate the size of particles. All the particles of ice crystal or water droplets that impinge the aircraft generate triboelectric effects on the aircraft skin. One of the main advantages of this sensor is that it does not need to be located in an icing impingement area on the aircraft, but can be located everywhere in the airframe.

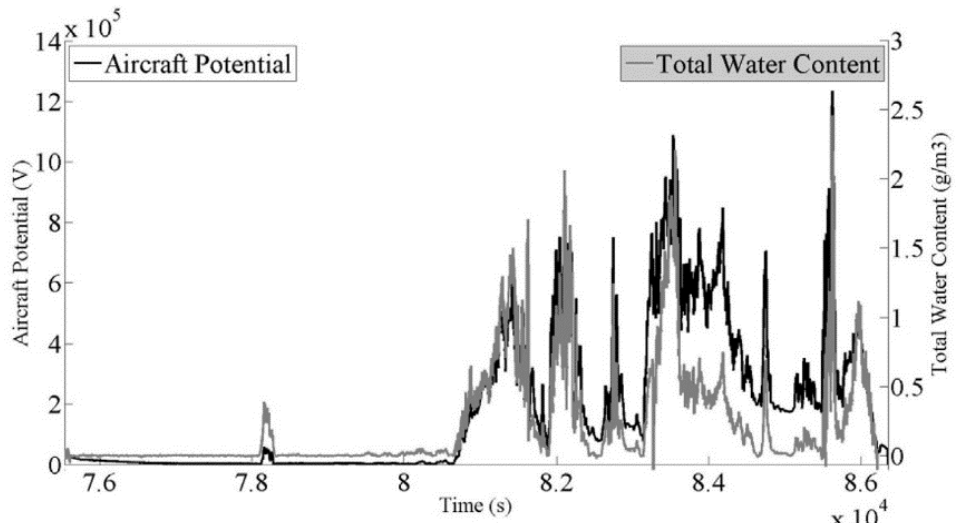


Figure 63: Time history of aircraft potential (black curve- units: V) deduced from AMPERA, and TWC (grey curve – units: g.m⁻³) from the IKP2 probe. Figure taken from reference [14].

5.8.2. Technology status at project start

Since the 1970's, ONERA has been involved in the understanding and characterization of the physical processes occurring during a lightning strike to the aircraft which has led to the development of on board sensors for atmospheric characterization. In the 1980's, a first EFM network had been designed to measure the electrostatic field inside thundercloud. The system was installed on a Convair CV580 (Collaboration between NASA and ONERA) and a Transall C160. A new version of this EFM network, called AMPERA, has been developed since 2010. It has been used on four flight test campaigns with a Falcon 20 and one with an Airbus A340.

In the framework of the HAIC European project, AMPERA was used to show the feasibility (TRL3) to retrieve in-flight the total water content (TWC) from the electric potential of the aircraft measured by the electric field mill network. The measurements performed during the flight campaigns Darwing and Cayenne show that there is a strong correlation between the TWC and the aircraft electric potential [Bouchard et al. 2020]. The sensor has never been tested in in-flight SLD icing conditions even if the principle of the sensor (triboelectric effect) should work with SLD. Due to that, at the starting of the SENS4ICE project the AMPERA system remained at a TRL of 3.

5.8.3. Technical Work

In the SENS4ICE project, the work performed on AMPERA was focused on the electrostatic simulation of the ATR42 aircraft platform to find the best position for integration of the EFM network, as well as the optimization of the AMPERA software to measure the TWC.

Based on the assumption of a uniform atmospheric electrostatic field around the aircraft, the electric field on the aircraft skin can be expressed by the following linear relationship:

$$E_i = \alpha_i E_x + \beta_i E_y + \gamma_i E_z + \lambda_i V_a$$

where E_i is the electrostatic field recorded by an individual field mill; E_x, E_y, E_z are the three components of the atmospheric electrostatic field in the aircraft reference; V is the aircraft potential. The aircraft's electric charge and the potential are linked by its electrical capacitance; $\alpha_i, \beta_i, \gamma_i, \lambda_i$ are constant coefficients. Note that these coefficients can be positive or negative except the λ_i coefficients which have all the same sign.

Figure 64 shows the electrostatic simulation on the SAFIRE ATR 42 platform. Each figure corresponds to the distribution of the coefficients of the above equation all over the aircraft skin. The two positions in the windows identified with a black cross are the best location for electrostatic measurement, as these have a moderate dependency on the V_a parameter (values around 220), but a very weak dependency on the electric field components (values near zero).

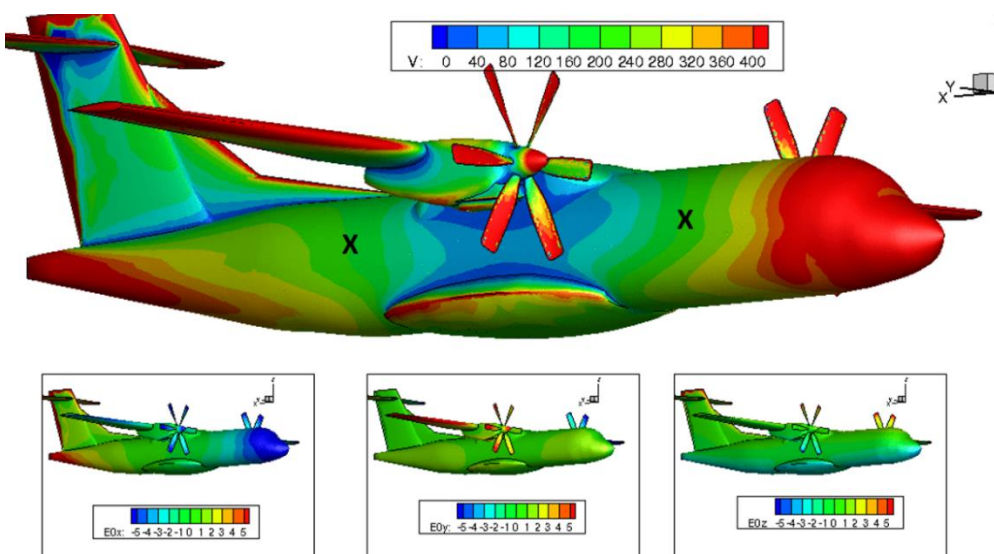


Figure 64: Electrostatic simulation on the SAFIRE ATR42 platform showing the distribution for the normal field coefficients V (upper), Ex (lower left), Ey (lower centre) and Ez (lower right).



Therefore, by using only one EFM placed in any of these positions and neglecting the terms with the electric field component in the above equation, we can directly determine the aircraft potential by $V_a = E/\lambda$. In order to enhance the accuracy of this measurement, it is possible to install a pair of EFM symmetrically along the fuselage axis. For the flight campaign, we chose to employ two pairs of EFM positioned in the rear windows of the ATR 42 platform, ensuring both accuracy and redundancy. Figure 65 presents an image of the SAFIRE ATR 42 indicating the two pairs of EFM installed in the rear windows.



Figure 65: SAFIRE ATR42 aircraft drawing with indication of the two right side windows where the EFM are installed, EFM2 and 4 (left, image Safire). Picture showing the two others mills, EFM1 and 3, installed symmetrically in the left side windows (right, image ONERA/ SENS4ICE project with Safire permission).

5.8.4. Flight Test

In April 2023, the European flight test campaign was conducted, consisting of 15 flights and more than 50 flight hours carried out under various icing conditions. Throughout the campaign, the AMPERA system demonstrated exceptional robustness, as no technical issues were observed with either the hardware nor software components. The real-time communication with the HIDS interface, to receive the aircraft data input (temperatures, velocities, altitude, etc.) and to send the AMPERA outputs (status, icing flag, TWC and trust level) worked well during all flights.

The first calibration flights in clear air were very useful to set the baseline for the aircraft electrostatic potential in different flight phases, including the take-off, landing, and during manoeuvres and engine power variation. At constant level and speed, V_A is around 300 V, and during high power engine phases, it can reach up to 3 kV. During the flight tests conducted under icing conditions, this measurement exhibited excellent sensitivity when encountering particles. The response time for entering and exiting a cloud with particles was approximately 1 second, and the electric potential inside the cloud exceeded 100 kV. This significant increase in potential clearly distinguishes it from a phase of clear air. Figure 66 shows the measurement during a flight with multiple cloud encounters.

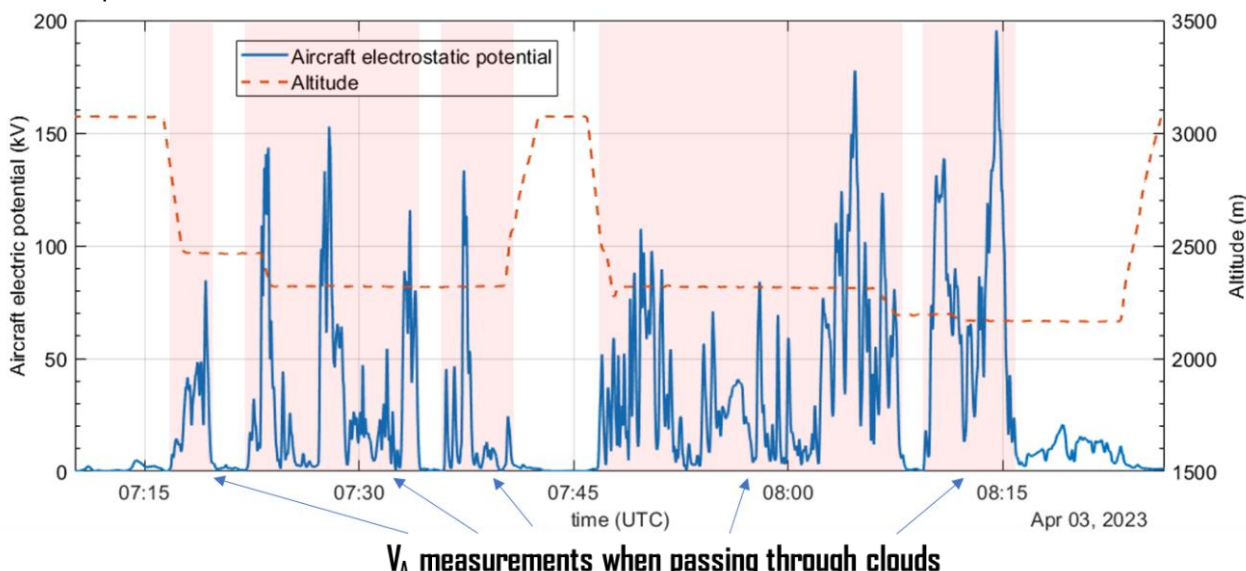


Figure 66: Aircraft electrostatic potential and altitude for the flight of April 3rd 2023, showing the excellent sensitivity of this measurement when passing through clouds.

The preliminary analysis and comparisons conducted with the reference probe have shown a strong correlation between the shape and variations of the measured LWC and the electrostatic potential. Figure 67 depicts the comparison between the AMPERA output and the Robust reference probe from SAFIRE, highlighting a significant agreement between the two signals.

In order to calculate a real-time atmospheric icing detection flag, we have proposed, during this campaign, a flag derived from three parameters: the aircraft potential (V_A) the static temperature (SAT), and dew point temperature (DEW). When comparing this flag with the airframe ice accretion flag obtained from the Rosemount Ice detector, we observe that the AMPERA flag demonstrates higher sensitivity. This is because the AMPERA flag considers the specific atmospheric conditions encountered by the aircraft during flight, while the Rosemount flag primarily accounts for ice accretion.

Further analysis with the reference microphysics measurements is necessary to extend our understanding of the physics behind the triboelectric process. Additionally, these measurements will help evaluate the AMPERA sensor's capability to differentiate between aircraft charging caused by water droplets and ice crystals.

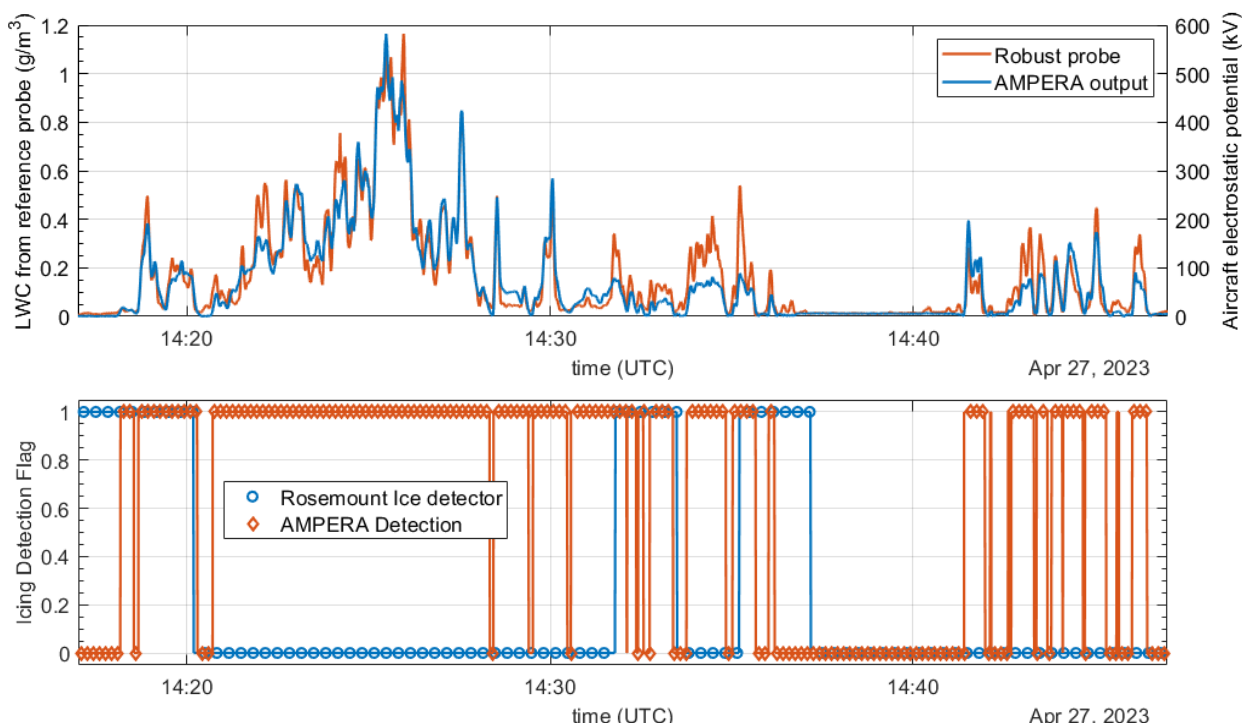


Figure 67: LWC and Aircraft electrostatic potential comparison (upper) and AMPERA atmospheric icing flag and Rosemount Ice accretion flag (lower).

5.8.5. Current TRL

Based on the feedback received from the flight test campaign and the analysis of the preliminary results, we have determined that the AMPERA system, used for icing detection application, achieved TRL 5-6 at the end of the project.

5.8.6. Short summary of further development, maturation and exploitation

ONERA's plan for future development involves ongoing enhancements and utilization of the AMPERA system for scientific in-flight campaigns. The goal is to expand its capabilities to detect various atmospheric hazards, including lightning, volcanic ashes, dust, and monitoring certain aspects of aircraft health through field mill signal processing. Furthermore, ONERA is considering applications such as atmospheric electrification and contrails characterization. In addition, the roadmap for sensor technology includes efforts to reduce the size of the system and adapt it for installation in Unmanned Aerial Vehicles (UAVs). This adaptation will open up new possibilities for utilizing the AMPERA system in UAV operations.



5.9. SAFRAN – AOD

5.9.1. Technology Description



The App. O Discriminator (AOD) aims to specifically detect icing conditions originating from the presence of Supercooled Large Droplets (SLD) of diameter larger than 100 µm in the atmosphere. It is an optical sensor based on imaging. It relies on shadowgraphy. This technique had been developed to obtain images of objects made of transparent material, such as droplets.

Short duration light pulses are emitted at high frequency. As they propagate in the atmosphere, they impinge the droplets and are deviated by refraction. A high-resolution camera equipped with an objective located in front of the light source grabs the images of the droplets. This configuration enables one to get very high contrast images.

Each frame is then processed for detecting the objects and counting them. The AOD can detect objects as small as 10 µm and can size them from 30 µm to 10 mm. Parameters of the droplet size distribution are derived to determine the nature and the severity of the icing conditions.

5.9.2. Technology status at project start

At the beginning of the project, this technology was at TRL1. The State-of-the-Art had been carried out and basic principles established.

5.9.3. Technical Work

During the SENS4ICE project, the main steps of the AOD development were:

- Defining the specifications from the MOPS ED-103,
- Dimensioning the optical, electronical and mechanical parts,
- Designing the optics: the imaging system was designed in order to ensure a resolution, sampling volume and a response time compliant with the ED-103 requirements - a constraint on the compactness of the shadowgraph configuration was also considered for improving the integration handiness but also reducing the de-icing need of the external part,
- Designing the electronics: an electronics circuit was developed for driving the LED, which generated pulses of 25 ns duration,
- Developing the image processing software: the image processing algorithm code was written in VHDL and Verilog - it was based on the Field-Programmable Gate Array (FPGA) technology to ensure real-time processing,
- Setting-up a breadboard experiment for testing the different parts,
- Fabricating a laboratory mock-up for assessing and validating the system architecture,
- Testing the sensor with calibration microspheres,
- Designing the sensor housing for the IWT test campaign.

This work enabled us to achieve the design of the sensor for the IWT test campaign shown on Figure 68. It contained an LED mounted on a PCB, a parabolic mirror for collimating the light, a telecentric objective mounted on a high speed and high-resolution camera, an electronics board driving the LED, two windows, some temperature probes and heating cartridges for de-icing.



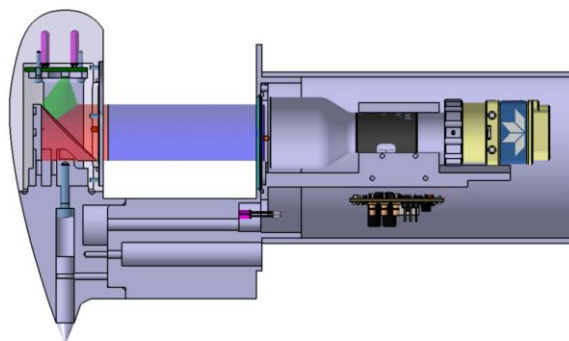


Figure 68: CAD of the AOD.

5.9.4. Laboratory Tests

The sensor design was mainly tested in laboratory. An AOD mock-up was set-up for lab testing. The tests consisted in using calibrated bead suspended in water in a cuvette. Indeed, the polystyrene beads behave similarly to water droplet for our sensor, are easy to handle, dilute and mix. Calibrated beads of 10, 30, 75, 90, 100 and 200 μm were used for testing our system. A picture obtained with our sensor can be seen in Figure 69.

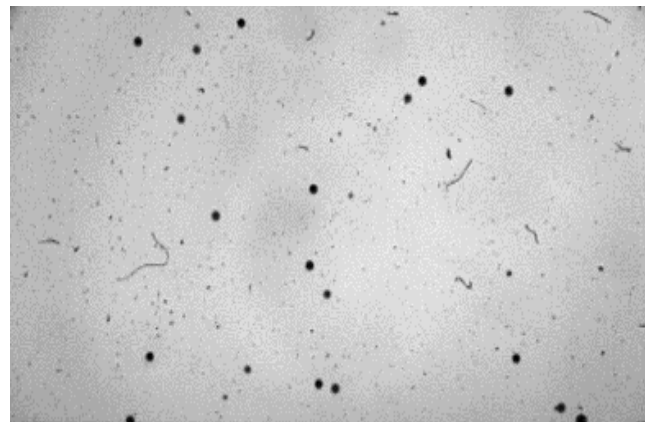
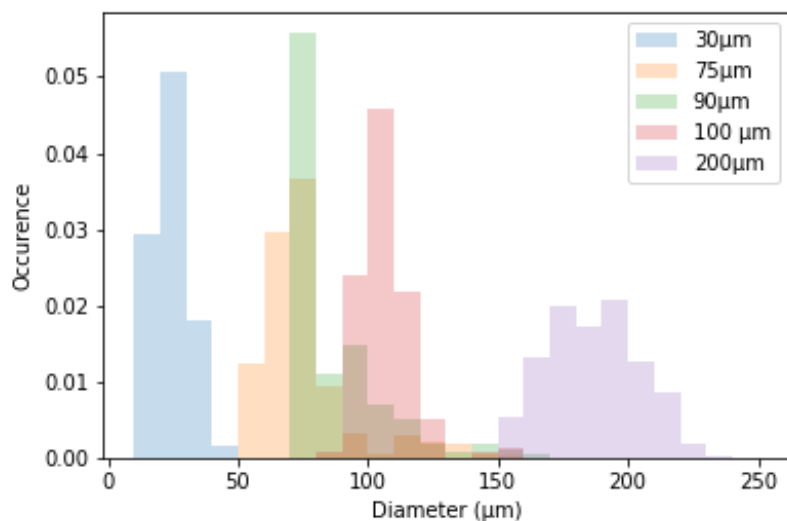
Figure 69: Picture of a cuvette filled with 200 μm diameter beads grabbed with the lab AOD.

Figure 70: Diameter measured by the AOD.

The beads size and number were measured from image acquisition followed by processing on an FPGA board. The results can be seen in the histogram in Figure 70. The diameter of the beads could be measured with a relatively high accuracy. Indeed, as it can be seen in Figure 71, the error on the MVD was less than 10% for all the diameters tested but the 30 µm. In this case, the error was slightly larger than the 20% recommended by the ED-103. However, it is out of the App. O droplets diameter.

The error on the maximum measured diameter noted D_{max} hereafter was much larger and reached up to 120% for 75 µm beads. This was mainly due to out-of-focus beads. However, it did not affect too significantly the App. O discrimination capabilities as Figure 72 shows. Indeed, this graph represents the proportion of beads detected as a bead, whose diameter is larger than 100 µm. In other words, it corresponds to the beads that could be counted as an App. O icing condition SLD. It varied from 9% for 75 µm to 21% for 90 µm and reaches almost 100% for 100 µm diameter beads. It can then be concluded that, by setting the appropriate threshold diameter to rise App. O alarm, only few false alarms could be triggered and almost all the App. O conditions would be detected.

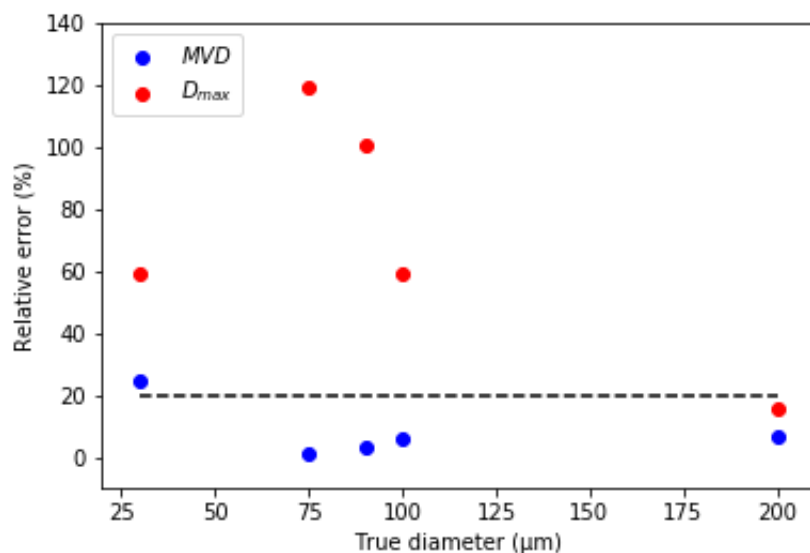


Figure 71: Relative error on the MVD and D_{max} measured with the AOD

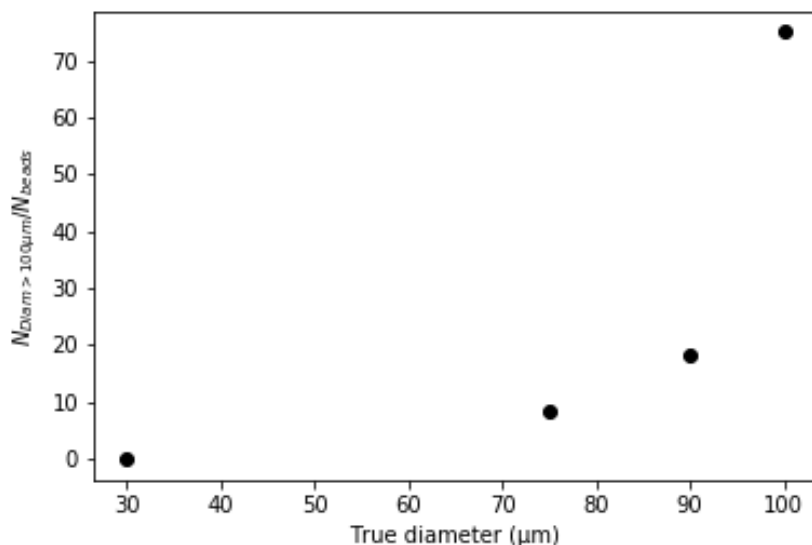


Figure 72: Number of beads detected as an SLD larger than 100 µm with regard to the bead diameter.



5.9.5. Ice Wind Tunnel Tests

Several issues related to the Covid crisis and the Safran healthcare policy led us to postpone the IWT. In addition, successive issues with our mechanical subcontractor increased our delay and planning deviation.

A careful analysis of the AOD sensors design revealed some strong drawbacks of this technology, which convinced us that it did not fit the market. It was then decided that this development would not be conducted any further. It was decided to cancel the IWT test campaign.

5.9.6. Current TRL

The AOD achieved TRL3 in January 2021.

5.9.7. Short summary of further development, maturation and exploitation

A careful analysis of the AOD sensors design revealed some strong drawbacks of this technology: a poor compactness, a large volume in the atmosphere leading to a high-power consumption for de-icing, a large drag coefficient and a cumbersome image processing need. This technology then, did not appear as the best candidate for Appendix O discriminator, which was confirmed by the technology assessment Made within SENS4ICE. It was then decided that this development would not be conducted any further.



5.10. SAFRAN – PFIDS

5.10.1. Technology Description

PFIDS is an optical ice accretion sensor able to measure Ice Accretion Rate. The PFIDS ice catch area, highlighted by a white circle in Figure 73, is illuminated by two wavelengths, λ_1 and λ_2 , and then a contrast is calculated by measuring the reflected light for both wavelengths. In order to determine the presence or not of ice, this contrast value is compared to a threshold, the “ice detection threshold”.

The contrast evolution, being proportional to the ice thickness accreted on the ice catch area, is used to evaluate the local Ice Accretion Rate, see Figure 62 where a classic example of PFIDS contrast signal is reported.

PFIDS can detect App. C, App. O and App. D/P mixed phases, but cannot discriminate between them.

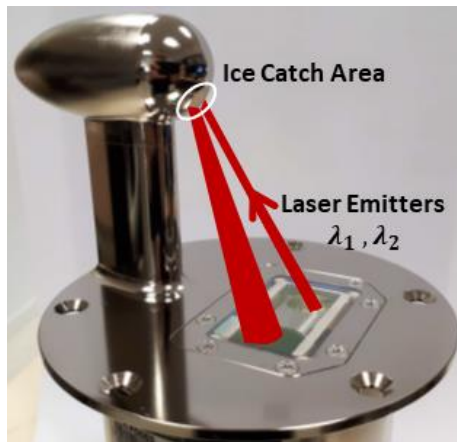


Figure 73: PFIDS working principle.

To avoid the Ludlam limit at temperature close to 0°C, PFIDS ice catch area is cooled down in order to increase the local freezing fraction, which tends to 1, and to force ice accretion.

After any ice detection, the PFIDS probe is heated thanks to a de-icing system in order to be ready to start a new detection cycle.

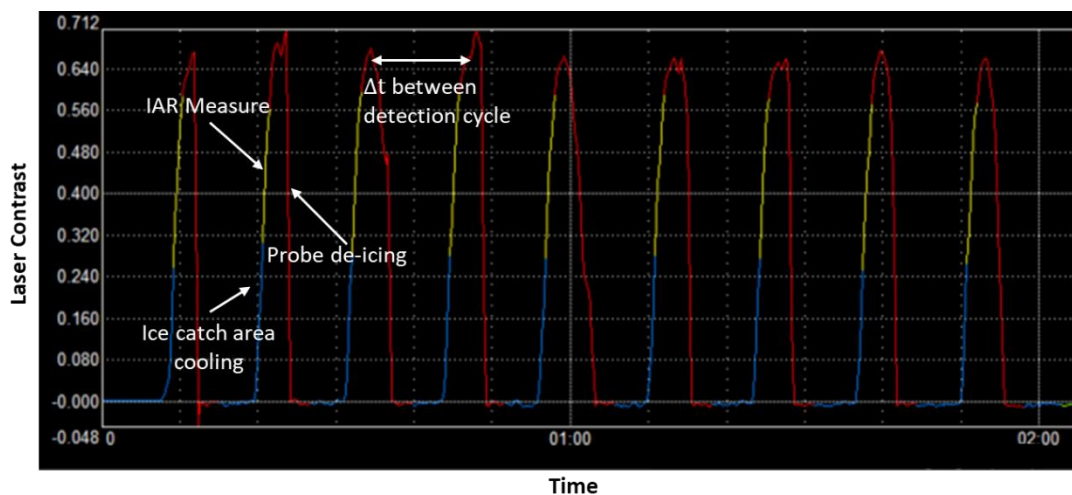


Figure 74: Typical PFIDS detection cycle.

5.10.2. Technology status at project start

PFIDS was already a TRL6 equipment at the beginning of the SENS4ICE project. Indeed, PFIDS provided excellent detection capabilities during previous icing wind tunnel tests and several flight tests campaigns.



5.10.3. Technical Work

In order to integrate PFIDS in HIDS a PFIDS Data Acquisition Unit was developed. It consists of a mini-computer able to convert the PFIDS CAN2.0 protocol to IENA protocol, the data protocol chosen for SENS4ICE flight tests. Moreover, the Data Acquisition Unit manages PFIDS Shop Mode (software update).

During the SENS4ICE project, a new algorithm aimed to improve the accuracy of PFIDS IAR measures, in particular for low IAR icing conditions, was developed as well. This new algorithm was used during both Ice Wind Tunnel tests and the flight test campaign.

5.10.4. Flight Test

PFIDS participated to the North American flight test campaign with Embraer. The detector was installed on the door of the right luggage rack of Phenom 300, see Figure 75.



Figure 75: Installation of PFIDS on Phenom 300 [images Embraer/ SENS4ICE project].

This position was suggested by the Embraer team, who realized collection efficiency analyses showing that, in this location, PFIDS would be able to detect both App. C and App. O conditions, see Figure 76.

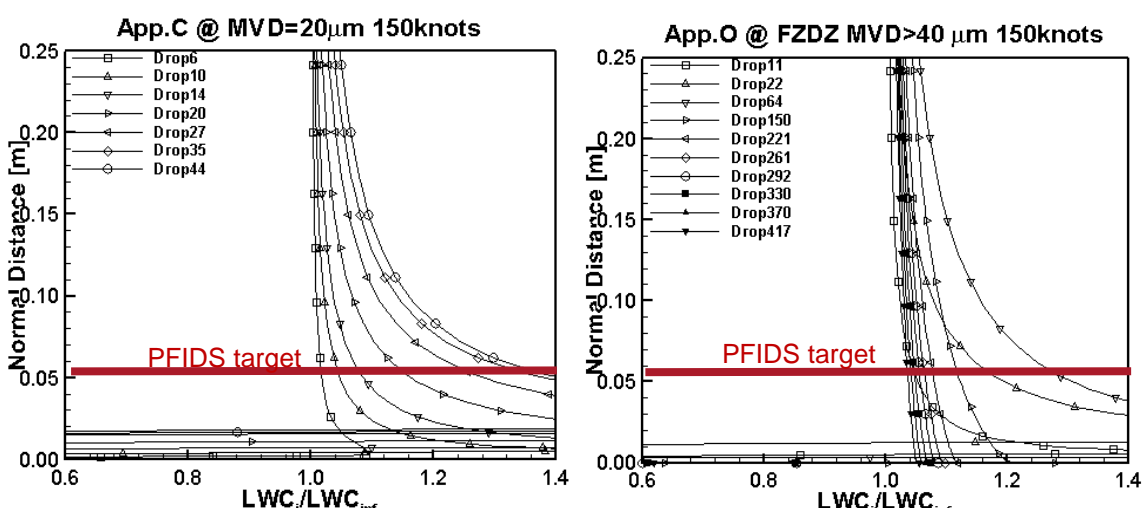


Figure 76: Example of water catch simulations results.

All the icing conditions encountered were detected by PFIDS.

The following figures show preliminary results of PFIDS for both App. C and App. O conditions.

In Figure 77, results of PFIDS detection for the flight 1475-leg 2 of the 23rd of February are illustrated. During this flight several App. C conditions were encountered, as demonstrated by both the MVD and LWC signals reported in the first two subplots of the figure. PFIDS was able to detect very fast (in less than 10s) all the conditions but the second one, since the SENS4ICE network was disconnected for about 20 minutes.

The IAR measured by PFIDS, the black curve in the last subplot, is well correlated to LWC. Actually, accurate comparisons are ongoing in order to properly consider the PFIDS installation factor.

Figure 78 displays PFIDS results for the flight 1476-leg 1 of the 25th of February. During this flight 5 App. O conditions were encountered, as shown by the blue curve of the first subplot representing the MVD of the droplets with a diameter greater than 100 μm . Even in SLD conditions, PFIDS was able to detect very fast (its response time is again of the order of 10s) and the IAR measures are always well correlated to the LWC ones.

Please note that at the time of writing of this report, the analyses of flight test data are still ongoing in order to evaluate the PFIDS installation factor (IF). Once this factor will be defined, it will be possible to obtain LWC measurements from PFIDS IAR since the aircraft speed is known:

$$LWC = IAR_{PFIDS} \cdot \frac{\rho_i}{TAS \cdot IF}$$

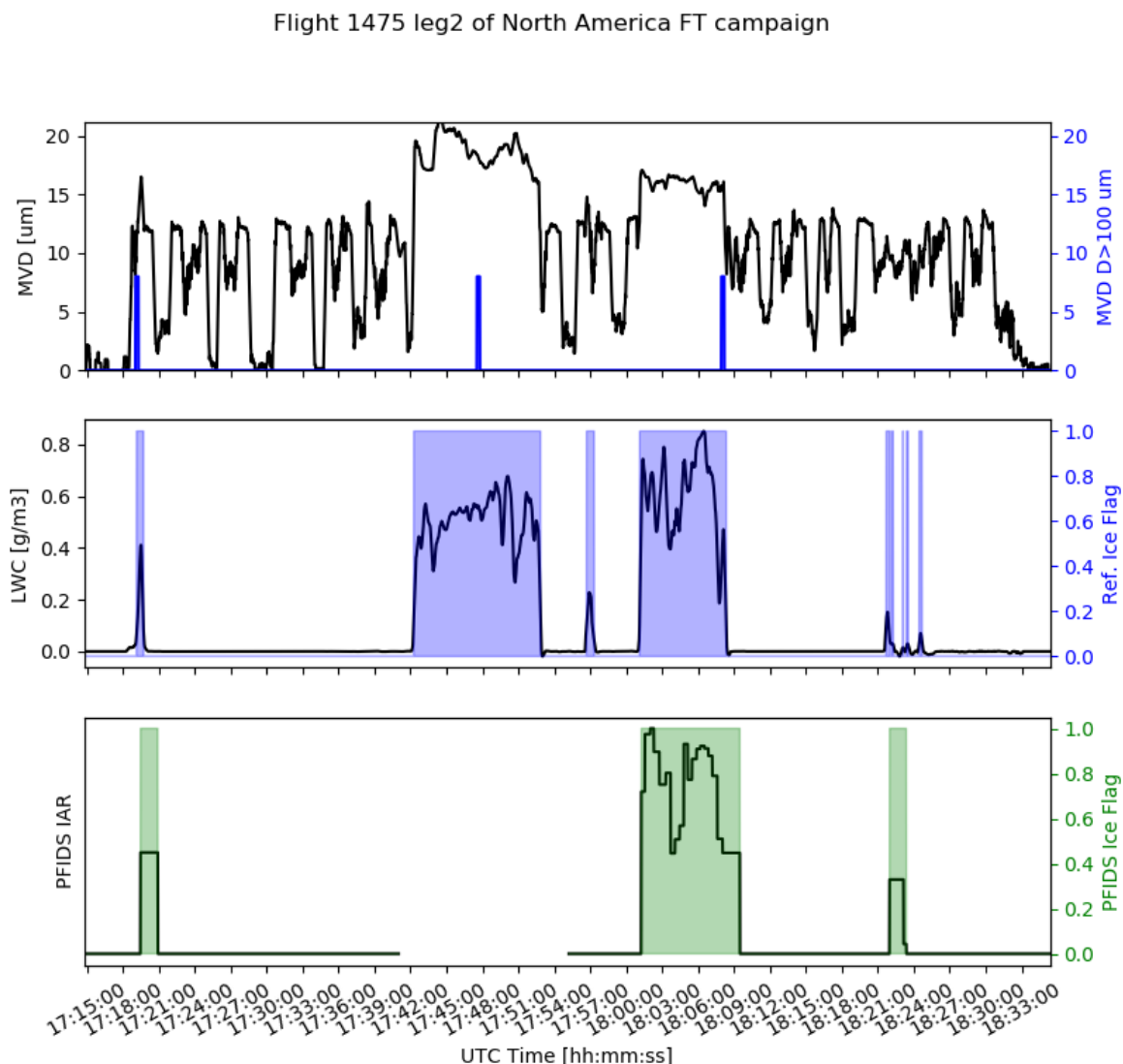


Figure 77: PFIDS detection results for the flight 1475-leg 2 of North America flight test campaign. In the first subplot is reported the MVD signal; in the second subplot is reported the LWC signal, in black, and the reference Ice Flag represented by the areas filled in blue; the third subplot displays PFIDS IAR measure, in black, and the PFIDS Ice Flag represented by the areas filled in green.

Flight 1476 leg1 of North America FT campaign

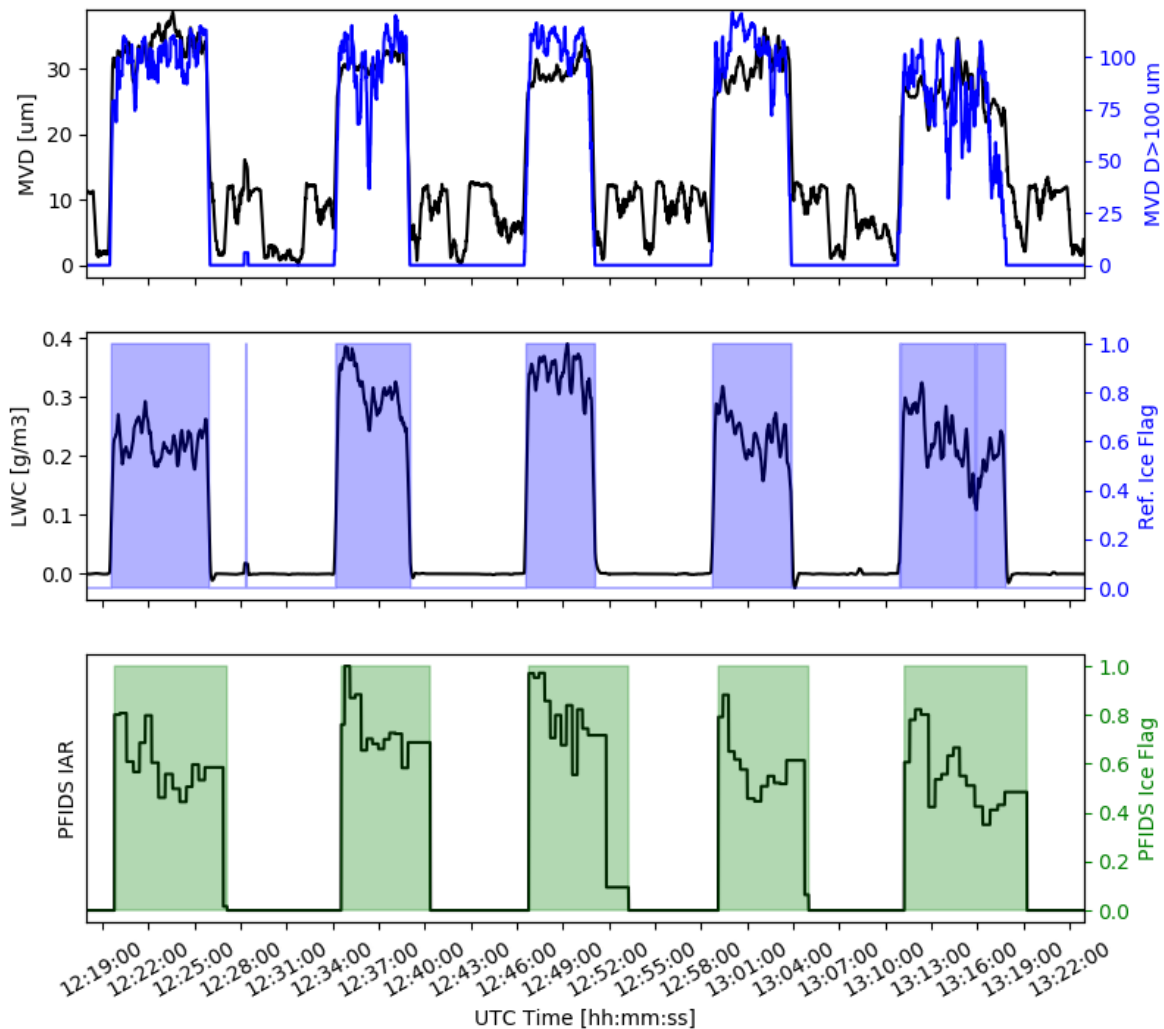


Figure 78: PFIDS detection results for the flight 1476-leg 1 of North America flight test campaign. In the first subplot is reported the MVD signal; in the second subplot is reported the LWC signal, in black, and the reference Ice Flag represented by the areas filled in blue; the third subplot displays PFIDS IAR measure, in black, and the PFIDS Ice Flag represented by the areas filled in green.

5.10.5. Current TRL

PFIDS is a TRL6 technology for liquid water icing condition detection and TRL3 for Appendix O discrimination.

5.10.6. Short summary of further development, maturation and exploitation

PFIDS was already a TRL6 detector at the beginning of the SENS4ICE project. Nevertheless, thanks to SENS4ICE, the performance of PFIDS, in particular in SLD conditions, was further tested and assessed.

The promising results obtained during both IWT test and the flight test campaign clear the way to further developments that will make PFIDS able to discriminate between Appendix C and Appendix O conditions, now a TRL3 function. In this way PFIDS will become even a better candidate for the hybrid detection approach, since indirect detection is not able yet to discriminate between conditions.

6. Hybrid Ice Detection Architecture including Indirect Ice detection

Within SENS4ICE a new hybrid ice detection approach was developed in order to combine the advantages of dissimilar ice detection technologies for more robust and reliable detection behaviour in App. C and App. O. Direct sensing technologies mostly cover only one specific part of the icing envelope or only allow to detect specific atmospheric parameters, but doing so in a very reliable manner. Hence, with in the SENS4ICE layered safety approach (Figure 2), the hybridisation is one goal to success. The indirect ice detection is part of the HIDS and allows with its specific implementation **detecting performance degradations** and therefore the ice accretion (see Figure 79). With this complementary information the HIDS is not only capable of responding very fast on encounters in icing conditions and ice formation on the sensor surfaces but also alert the flight crew on the limited aircraft capabilities if the flight performance is significantly degraded. Hence, the HIDS allows a next step to the loss-of-control prevention, which is the inner layer in Figure 2.

The HIDS implementation is designed to be applicable to both flight test benches used for SENS4ICE flight test campaigns, which are very different aircraft configurations: a light business jet aircraft (Embraer Phenom 300) and a regional class turbo-prop aircraft (ATR 42). This applicability is possible through the generic formulation of the detection methodology itself, not relying in specific information about the aircraft: the required aircraft-specific adaption of the detection is achieved by considering the aircraft-specific reference, which is an input to the algorithm and not part of the core implementation.

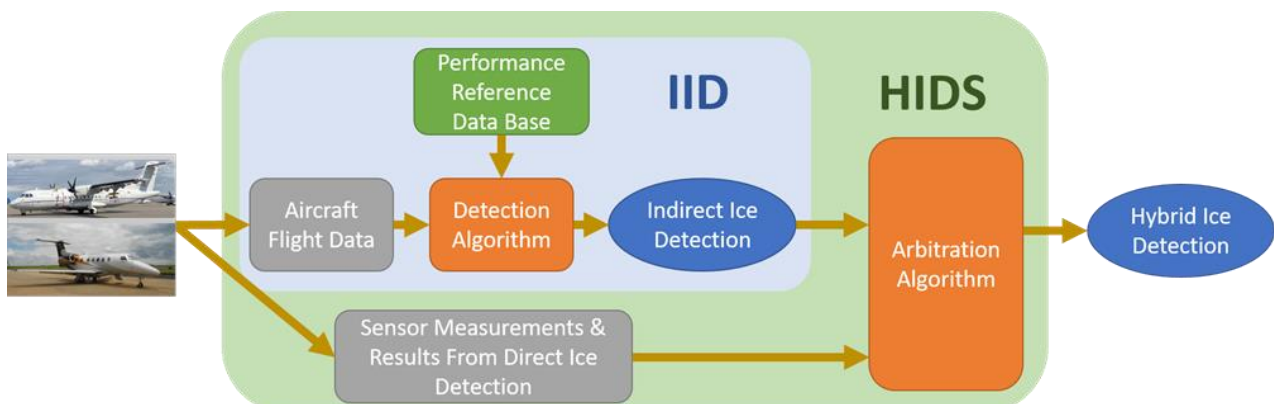


Figure 79: SENS4ICE Hybrid Ice Detection System overview (pictures credit DLR / Embraer / SAFIRE).

The following subsections provide an overview of the SENS4ICE hybrid and indirect ice detection approach. For a more detailed description please refer to SENS4ICE deliverable D4.2 “Final report on hybrid ice detection development” [7].

6.1. Short Summary

Through the analysis of flight test data, the advantages of the hybrid ice detection approach are undeniable: HIDS can guarantee an early ice detection, thanks to the fast and reliable direct ice detection technologies developed within the SENS4ICE project, together with a continuous monitoring of the aircraft performance during the icing conditions encounter and even after. Indeed, the indirect detection algorithm was able to detect aircraft performance degradation due to the presence of residual ice accretion on the airframe after leaving the icing clouds. These capabilities clear the way for the use of HIDS as a Primary Ice Detection system, since it is based on dissimilar ice detection sources and can provide an automatic control and monitoring of the aircraft Ice Protection Systems. Actually, the proven capability of IIDS to detect residual ice accretion on the whole airframe provides a direct measurement of ice protection efficiency. HIDS could even enable significant reduction in fuel consumption thanks to a more efficient use of IPS, thanks to the indirect detection, associated to the monitoring of remaining ice.

Thanks to the flight tests campaign and the promising results obtained, the hybrid ice detection approach has been validated during real icing conditions and may be consequentially considered TRL5, according to the Horizon 2020 TRL definitions.



With regards to the capabilities of DIDS and HIDS in Appendix O icing conditions, it can be pointed out that only a small part of the envelope was encountered during the flight test campaign, mainly FZDZ. Covering the whole Appendix O, including the rare FZRA, to properly assess the performance of the SENS4ICE technologies, can hardly be met in a single flight campaign.

Additional research is thus necessary in order to further mature the hybrid approach in Appendix O conditions, as well as, to improve such technology on a system level. Indeed, all the aspects linked to safety issues, implementation of the IIDS/HIDS algorithm within aircraft avionics, etc., were out of the scope of SENS4ICE project. Nevertheless, all these subjects will be crucial to address HIDS airworthiness.

6.2. General Description of the HIDS

HIDS allows to combine the direct ice detection, provided by the DIDSs installed outside the aircraft, which measures directly the local air flow characteristics and/or the ice accretion on a specific surface, and the indirect detection, provided by the IID, which evaluates the effect of ice accretion on aircraft flight performance.

During the flight test, the HIDS main functions were:

1. To initialize IID with some data not available through the A/C network, i.e. A/C weight, CG position, Fuel weight, before the take-off;
2. to collect in real time all the aircraft data transferred through the FTI network in order to feed the IID algorithm;
3. to collect DIDS outputs, standardize each data format,
4. to run the IID algorithm,
5. to combine **direct and indirect detection**, via an internal function called *Arbitration*, in order to provide a synthetic and optimized ice detection information.

HIDS Arbitration function aims to extract a single, consistent output by coupling Indirect Detection with each Direct detector. As displayed in Figure 80, this function takes as input Direct and Indirect detection outputs, defines the validity on these two signals by considering the status of the detection sources, checks for inconsistencies, and combines them by considering A/C characteristics in icing conditions.

The Arbitration function, indeed, will raise an Ice Flag, only if $TAT \leq TAT_{cr}$, where TAT_{cr} is the maximum TAT at which ice accretion is possible on the airframe (for SENS4ICE FT, $TAT_{cr} = 5^\circ\text{C}$ for Embraer and $TAT_{cr} = 10^\circ\text{C}$ for ATR/SAFIRE), and thanks to direct detection IAR or LWC measurements, can provide an ICE SEVERITY signal based on specific thresholds provides by the A/C manufacturer. For SENS4ICE tests, standard thresholds were used:

- SEVERE ICE if $IAR_{DIDS} > 7.5 \text{ cm/h} (=1.25 \text{ mm/min})$
- SEVERE ICE if $LWC_{DIDS} > 1.2 \text{ g/m}^3$

Since direct detection shall guarantee an early detection, while indirect detection needs a certain ice accretion on the airframe, the Arbitration function can provide the detection outputs after a certain delay, Δt , in order to wait for IID detection confirmation. This could reduce direct detection false alarms and warn the pilot only if a performance degradation that could put in danger the A/C safety is detected. This Δt can be a fixed value, or can be evaluated automatically by the HIDS if the DIDS can provide an accurate measure of the IAR and the maximum admissible ice thickness on the airframe, τ_{MAX} , is known:

$$\Delta t = \frac{(\tau_{MAX} - X\% \tau_{MAX})}{IAR_{DIDS}}.$$

Note that during the SENS4ICE flight test campaigns, the arbitration function combined separately each DIDS installed on the A/C with IID.



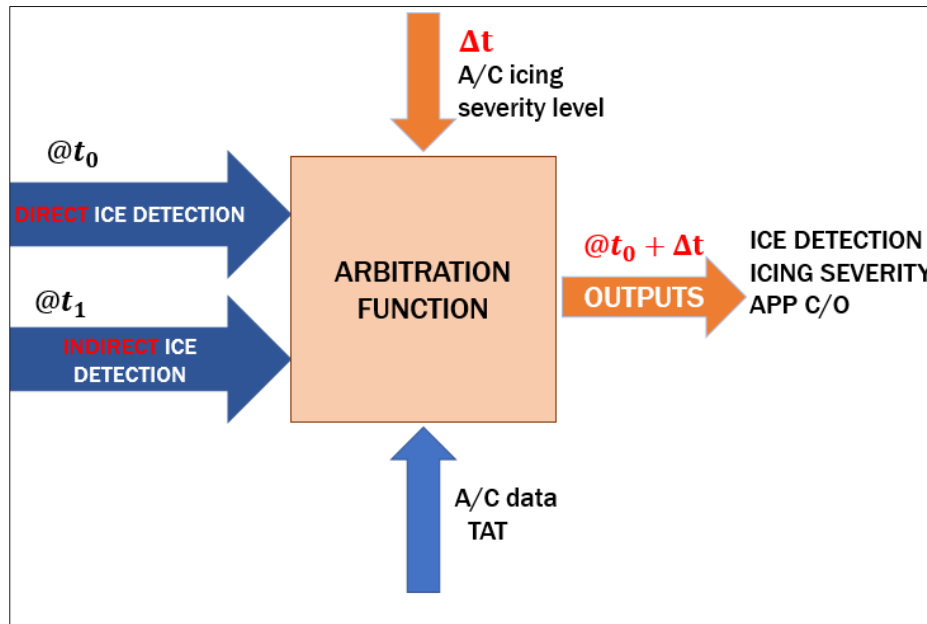


Figure 80: Schematic representation of HIDS Arbitration function.

On the SAFIRE ATR 42, HIDS had to guarantee two more functions:

1. To record all the project level (“public”) data, shared with the SENS4ICE consortium and used to perform the presented analyses;
2. To convert the aircraft data coming from ATR FDAU and SAFIRE FTI unit into the SENS4ICE IENA format, used for the North American flight test campaign. For more details on the SAFIRE ATR 42, see Ref. [1].

Actually, in order to limit the difference between Embraer and ATR HIDS demonstrator, on SAFIRE ATR 42 was installed the HIDS-PC: a PC with a software developed by SAFRAN able to perform the A/C data decoding, also used for data recording.

Moreover, the software installed on HIDS-PC was also used to monitor and display in real time HIDS/IID and DIDSs outputs, as well as A/C data. This last function of HIDS-PC turned out to be a real asset for European flight test campaign since it allowed the SENS4ICE partners participating to the flight test campaign to easily obtain real time information during the flight and to do in-situ cross-comparisons between different sensors.

Figure 81 shows the HIDS installed on SAFIRE ATR 42 on the left, and the HIDS-PC interface on the right.



Figure 81: ATR HIDS, on the left, and HIDS-PC user interface, on the right [images SAFRAN/ SENS4ICE project].

For the North American flight test campaign, data recording and HIDS/IID and DIDS monitoring were operated by Embraer flight test engineers.

The overall behaviour of HIDS during the two flight test campaigns was very promising: HIDS was always able to receive and provide data through the A/C network, IID was always well initialized before the take-off, and all the encountered icing conditions were detected thanks to the combination of direct and indirect detection.

Regarding data recording during the European flight test campaign, no problem was detected and the data were properly stored and shared with the involved partners.

In the following §§, detailed analyses of the selected flights are provided.

6.2.1. Specific Implementation during the North American Campaign

The experimental prototype of Phenom 300 was equipped with four different DIDS that were tested and used for hybridisation: Aerotex AIP, Collins IDS, Honeywell SRP and SAFRAN PFIDS, together with HIDS/IIDS. The basic HIDS architecture for this flight test campaign is given in Figure 82.

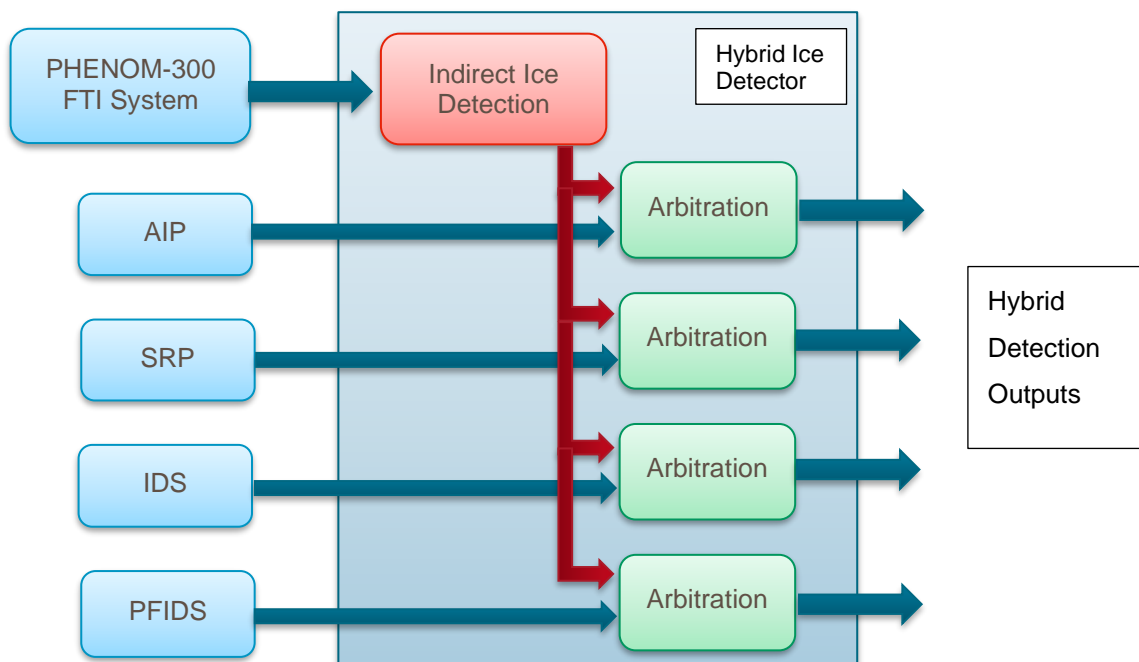


Figure 82: Basic HIDS architecture for North American flight tests.

6.2.2. Specific Implementation during the European Campaign

The SAFIRE ATR 42 environmental research aircraft was equipped with different direct sensors, of which only the following were used for hybridisation: INTA FOD, DLR LILD and ONERA AMPERA. The basic HIDS architecture for this flight test campaign is given in Figure 83.

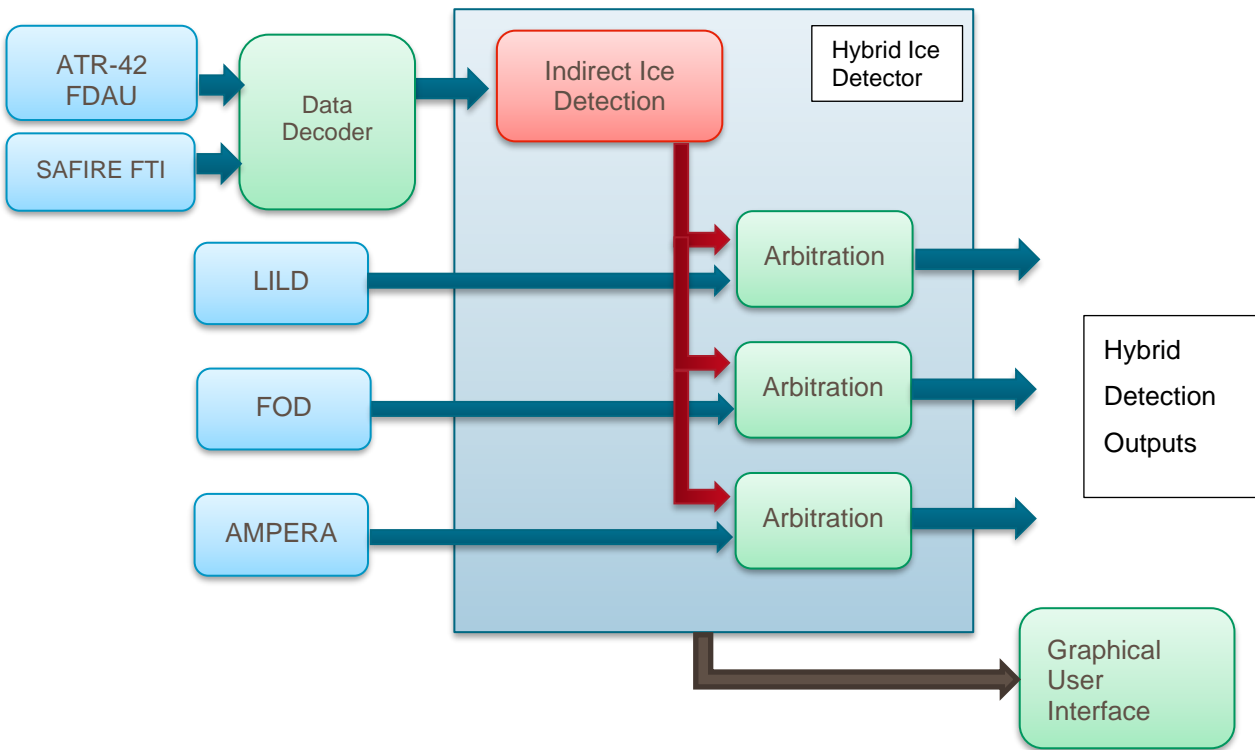


Figure 83: Basic HIDS architecture for European flight tests.

6.3. Indirect Ice Detection Algorithm and Implementation

Within SENS4ICE the “indirect ice detection” (IID) was further developed and matured and is one important project pillar. It is a novel methodology and system for the **on-board surveillance of aircraft flight performance used for ice detection purposes**. It was originally formulated and presented as a performance-based ice detection methodology, e.g., in Ref. [3]. It utilizes the effect of aircraft performance degradation due to ice accretion. The idea of the IID is not restricted to an application on large transport aircraft but can also enable a reliable ice detection for aircraft systems, such as small UAV, which currently have no ice detection system, but operate in hazardous environments with very different icing conditions.

One major effect of aircraft ice accretion is a **significant drag increase due to surface roughness changes**, parasitic influence of ice protuberances, and local flow separation. Another effect of icing is a change of the aircraft lift behaviour, causing e.g., earlier or more abrupt flow detachment with increasing angle of attack and/or a reduction in aircraft lift slope. Both together significantly alter the aircraft flight performance which can be monitored during flight. Figure 84 illustrates the typical icing-induced change of the lift and drag curves as generally described, e.g., in the AGARD report 344 [4]. Icing will also change the aircraft's flight dynamics (e.g., pitching and rolling moment). In addition, the control characteristics are negatively affected by icing and change the aircraft dynamics differently according to the specific occurrence of ice accretion. But these changes are very difficult to detect during flight, for what the IID relies on the icing-related change of aircraft flight performance [3].

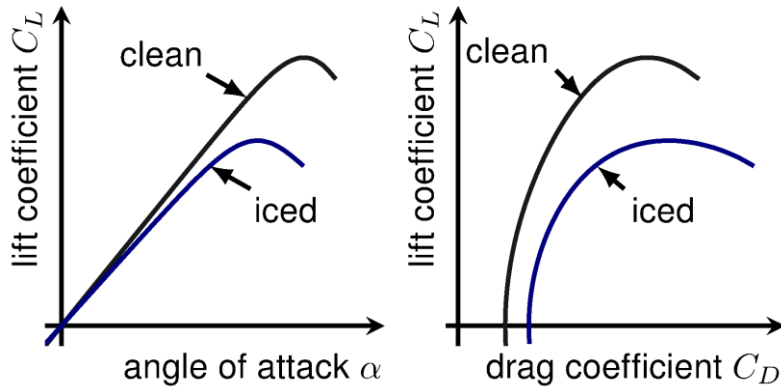


Figure 84: Expected icing influence on aircraft aerodynamics (lift and drag coefficient); adapted from [4].

Hence, aircraft flight performance monitoring can provide crucial information to the pilots about the current (limited/degraded) aircraft capabilities while only requiring the sensor information that is available on all modern airliners and business jets. The advantage of the developed methodology is that it relies only on the change in flight performance (i.e. steady flight states) contrary to the many failed attempts (see for detailed information about this in Ref. [3]) based on the estimation of changes in the aircraft's dynamic behaviour or a combination of both. The change/degradation in the flight performance is an indicator of ice accretion that is both robust and highly available: unlike the approaches based on the detection of changes in the aircraft dynamical behaviour, it can be used also during steady flight conditions (most of an operating flight) and can detect icing effects significantly before entering into stall. Although other direct ice measuring approaches for the detection of icing conditions or ice accretion on the airframe could deliver a partly similar information, the indirect detection using the performance monitoring approach would not require (potentially costly) modifications of existing and future aircraft. It is important to highlight that the method within the IID is focused on the flight performance changes without any specific need for additional dynamic aircraft excitations. Such an excitation is not acceptable during normal operations and especially not when flying with an aircraft that has a reduced (unknown) maximum-lift angle of attack due to icing.

The basic assumption for the indirect ice detection using performance monitoring is the possibility to discriminate between (very slow and low) performance variation of a single aircraft over lifetime in service (or within a fleet of same type) and the (much faster) performance variation caused by icing. Factors causing the flight performance variations across airplanes from the same type are for example:

- production tolerances,
- aircraft skin repairs,
- aircraft skin contamination (e.g., dirt),
- engine aging causing reduced efficiency, or
- engine contamination.

The aircraft flight performance can be seen as follows:

$$\text{Flight Performance} = \text{Nominal Aircraft Performance} + \text{Expectable Variation} + \text{Variation to be detected}$$

whereby the “Expectable Variation” part gathers the effects mentioned previously and the “Variation to be detected” is subject to the indirect ice detection approach. The first step is to determine the typical and most extreme flight performance variation (“Expectable Variation”) encountered during regular airline operations (due to a real performance variation or sensor errors).

The basic idea of the herein-proposed detection method is to compare the current (possibly ice-influenced) aircraft flight performance characteristics with a known reference, as schematically represented in Figure 85. The flight performance can be formulated as a power imbalance (change of total energy) \dot{E}_{tot} in both cases (current state and reference), which allows to represent the changed aircraft characteristics in only one significant value and reduces the detection module complexity. Moreover, it combines the influences of aerodynamics and engines on the aircraft performance.

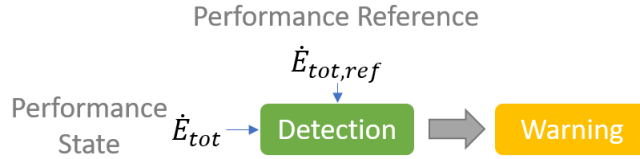


Figure 85: Basic principle of the IID method based on the aircraft power imbalance.

The power imbalance \dot{E}_{tot} is analytically derived through

$$\dot{E}_{tot} = V_{TAS} \cdot \dot{V}_{TAS} \cdot m_{AC} + \frac{1}{2} \cdot V_{TAS}^2 \cdot \dot{m}_{AC} + g \cdot \dot{H} \cdot m_{AC} + g \cdot H \cdot \dot{m}_{AC}$$

with the altitude change (with respect to time) \dot{H} referenced to the surrounding air and the speed change (with respect to time) \dot{V}_{TAS} . Note that the gravitational acceleration is assumed to be constant and its variation with time can be neglected for the calculation of the power imbalance. The following scaling/conversion of this power imbalance into an equivalent drag coefficient variation according to Ref. [3] is used:

$$\Delta C_D \approx \frac{\dot{E}_{tot,ref} - \dot{E}_{tot}}{V_{TAS} \cdot \bar{q} \cdot S}$$

This nondimensional value is well comparable to a predefined threshold and indicates an abnormal performance variation when exceeding the threshold value, independent from any flight point. Moreover, it is well interpretable in terms of aerodynamics and flight mechanics by aerospace engineers and allows a direct assessment of the magnitude of aerodynamic degradation caused by icing within the IID. The equivalent drag coefficient is calculated by comparison of the current determined power imbalance \dot{E}_{tot} and a predefined reference value $\dot{E}_{tot,ref}$. The latter is a function of certain aircraft flight parameters like altitude, speed and load factor, the aircraft configuration (e.g. mass, high lift system configuration) and propulsion system state. In Ref. [7] a description of the development of the performance reference for the two flight test benches is given.

The equivalent drag coefficient is well comparable to a predefined threshold value and indicates an abnormal performance variation when exceeding. This is further independent from any flight point. Note that a drag coefficient value is well interpretable in terms of aerodynamics and flight mechanics by aerospace engineers and allows a direct assessment of the magnitude of aerodynamic degradation caused by icing. Within the IID, this drag coefficient is normalized with the aircraft's zero-lift drag coefficient and compared to a predefined threshold of 10%⁹. Note that in the nominal case, the additional drag coefficient is zero and there is no relative change to the normal drag condition.

The indirect ice detection is implemented as a modular set of functions, including the core detection algorithm, the required data pre-processing and a subsequent detection result filtering to prevent false detections. The filtering also helps to achieve the necessary system robustness and reliability. Within SENS4ICE, the indirect ice detection is part of the HIDS and allows with its specific implementation detecting performance degradations and therefore the ice accretion on the two very different testing aircraft (see Figure 79). This is possible through the generic formulation of the detection methodology itself, not relying on specific information about the aircraft: the required aircraft-specific adaption of the detection is achieved by considering the aircraft-specific reference, which is an input to the algorithm and not part of the core implementation. With regard to a highly adaptable use of the IID for different aircraft types, this formulation of the detection methodology is a significant advantage for prototyping the specific system implementation compared to more integrated approaches. Such implementations would require more specific information about the aircraft inside the core detection algorithm. Hence, there are still several needs for adjustments inside the IID for a specific aircraft type, which concern:

1. the flight data pre-processing,
2. the flight performance reference data base,
3. the indirect ice detection threshold and confirmation times,
4. the detection reliability conditions.

which are further detailed below.

⁹ During the European flight test campaign, a threshold of 15% was used, but changed to 10% during the post flight data evaluation because the IID outputs were more robust to variations than initially expected.



The IID is currently implemented in MATLAB®/Simulink including several parts formulated in code originating from the SENS4ICE project partners. Basically, the methodology can be implemented in different formats depending on the framework to run with. For SENS4ICE a very agile prototyping and dynamic testing was required for which MATLAB®/Simulink is very handy. Furthermore, for flight testing the HIDS runs on a dSpace MicroAutoBox in real time, and the Simulink model can be easily transferred to the hardware including a full intellectual property protection required for several parts of the IID. Future exploitation will presumably provide a code implementation running with aircraft avionic systems.

The IID is designed to run continuously during the whole flight and to monitor the aircraft flight performance, and a potential degradation, independently from any specific flight phase or manoeuvre, as discussed in Ref. [3]. This also includes considering different aircraft configurations for different settings of the high lift system and gear extension. Nevertheless, the implementation in SENS4ICE was experimental and limited to one aircraft configuration without flaps or gear extended because of the flight test in icing conditions being only performed in this configuration for flight safety reasons. For all other aircraft configurations, the IID is designed to detect that the configuration is not reflected in the current implementation, freeze and set an unreliability flag allowing the HIDS to discard the current IID output. Freezing in this case allows to not load the moving average filters with unreliable data leading to a false positive detection when the IID is reactivated after a configuration change. A similar procedure is applied for short-term effects on the flight performance not included in the reference flight performance data base to reduce the overall effort for calculations in the IID like the use of speed-brakes. During these phases, the IID also freezes and the output unreliability is set.

6.4. Flight Test Results

DISCLAIMER: the assessment of icing severity used in this section is only for research and development purposes based on engineering science judgement but not related to the aircraft operations.

6.4.1. North American Flight Test Campaign

The results of the analyses shown hereinafter are obtained by replaying offline the whole flight test scenario by using post-processed data for the indirect detection, the microphysics and direct sensors (AIP, SRP and IDS).

As displayed in Figure 86 FT1476-1 was characterized by 5 IC classified as App. O encounters. The parameters characterizing these IC, as well as the theoretical IAR and detection time are reported in Table 9.



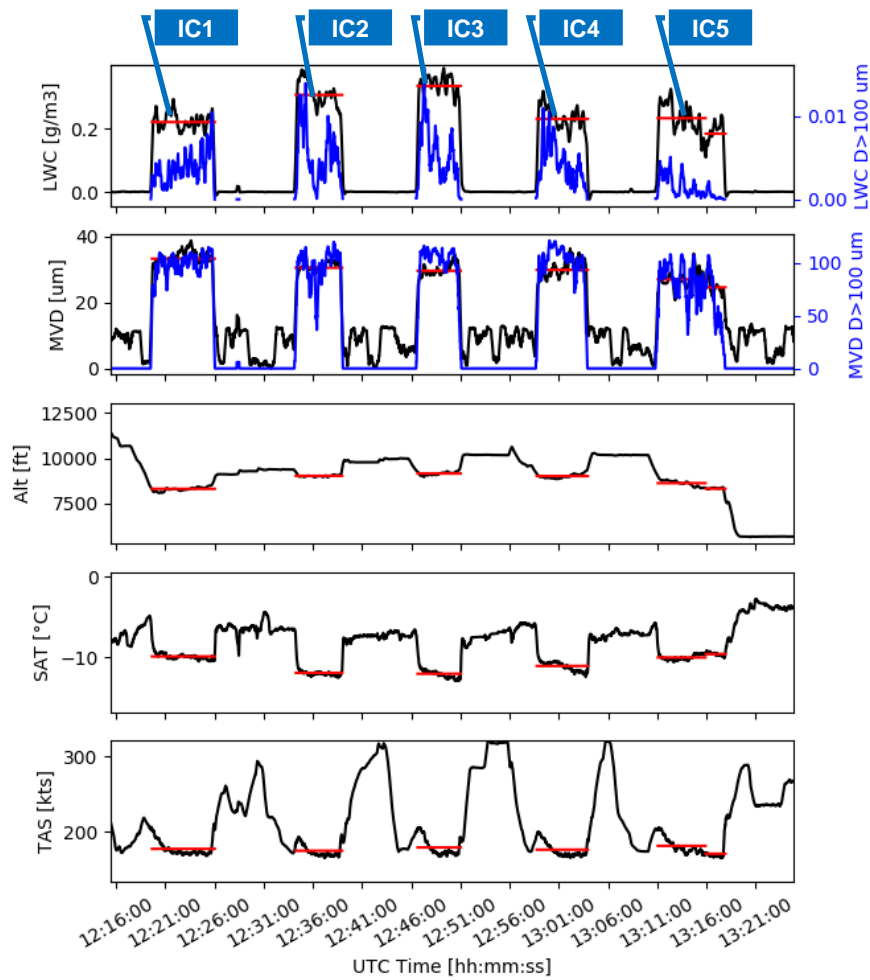


Figure 86: μ Physics and A/C data for FT1476-1. The red lines represent the calculated average values of each parameters during the icing encounters. Such values are reported in Table 9.

Table 9: Characteristics of IC1, IC2, IC3, IC4 and IC 5 for FT1476-1.

IC	ICE START (μ P)	ICE END (μ P)	Duration (μ P)	LWC [g/m ³]	MVD [micron]	Alt [ft]	SAT [°C]	TAS [kts]	ED103 IAR [mm/min]	ED103 Resp time [s]
1	12:19:37	12:25:58	00:06:21	0.22	32.91	8309.41	-9.82	177.97	1.15	15.66
2	12:34:14	12:39:05	00:04:51	0.30	29.79	9038.41	-11.76	175.31	1.52	11.85
3	12:46:38	12:51:07	00:04:29	0.33	28.97	9165.32	-11.91	180.03	1.70	10.58
4	12:58:47	13:03:55	00:05:08	0.23	29.83	9008.57	-11.00	176.47	1.18	15.19
5	13:10:58	13:17:51	00:06:53	0.22	26.10	8549.39	-9.83	178.73	1.10	16.38

The detection signals of DIDSs and IID are compared with the reference μ P ice flag in Figure 87: the detectors were able to detect the 5 conditions and SRP and IDS, which can discriminate between App. C and App. O, considered the 5 encounters as App. O conditions, as displayed by Figure 88. Table 10 reports the number of detections for each detector.

Unfortunately, during this flight Aerotex AIP faced same issues, for this reason its data are not available.

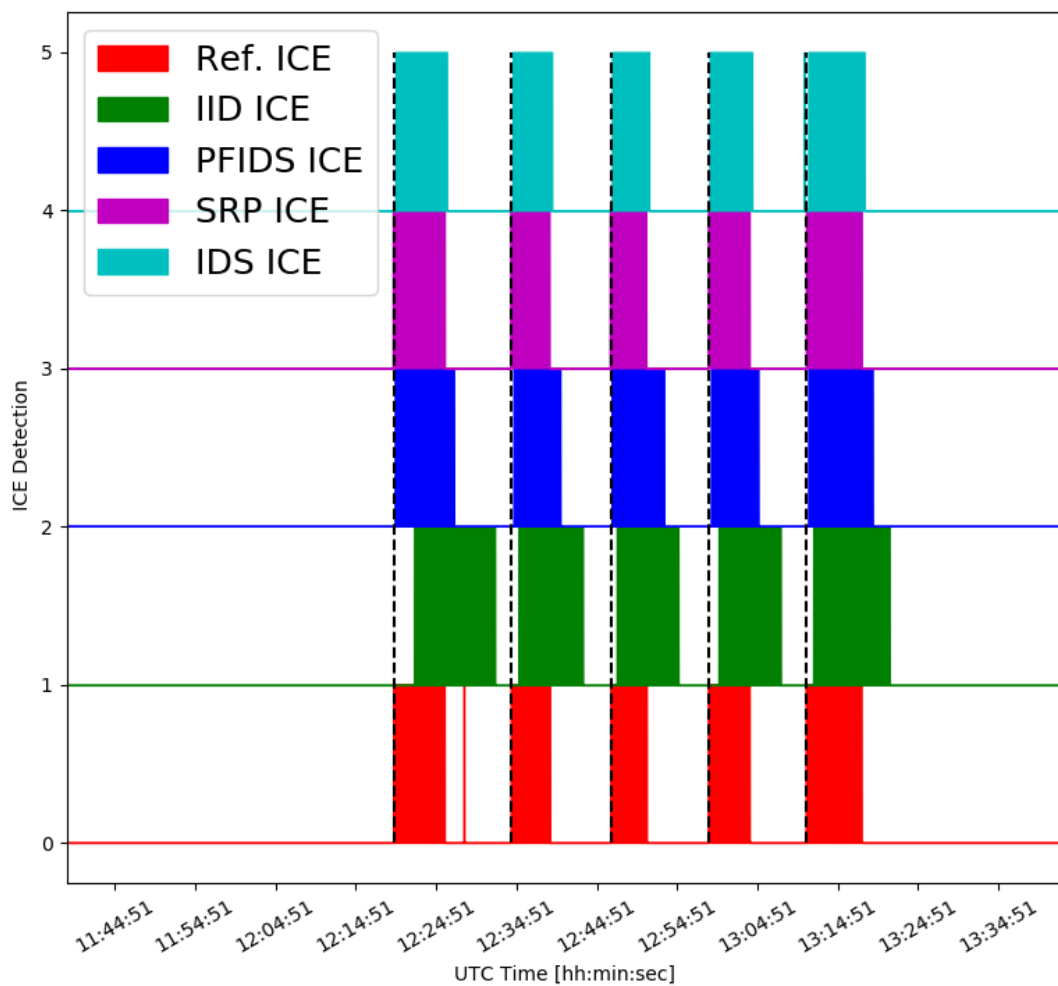


Figure 87: Ice Detection signal of DIDSs and IID for the icing encounters of FT1476-1. From the bottom to the top: μP , IID, PFIDS, SRP, IDS.

Flight 1476 leg1 of North America FT campaign

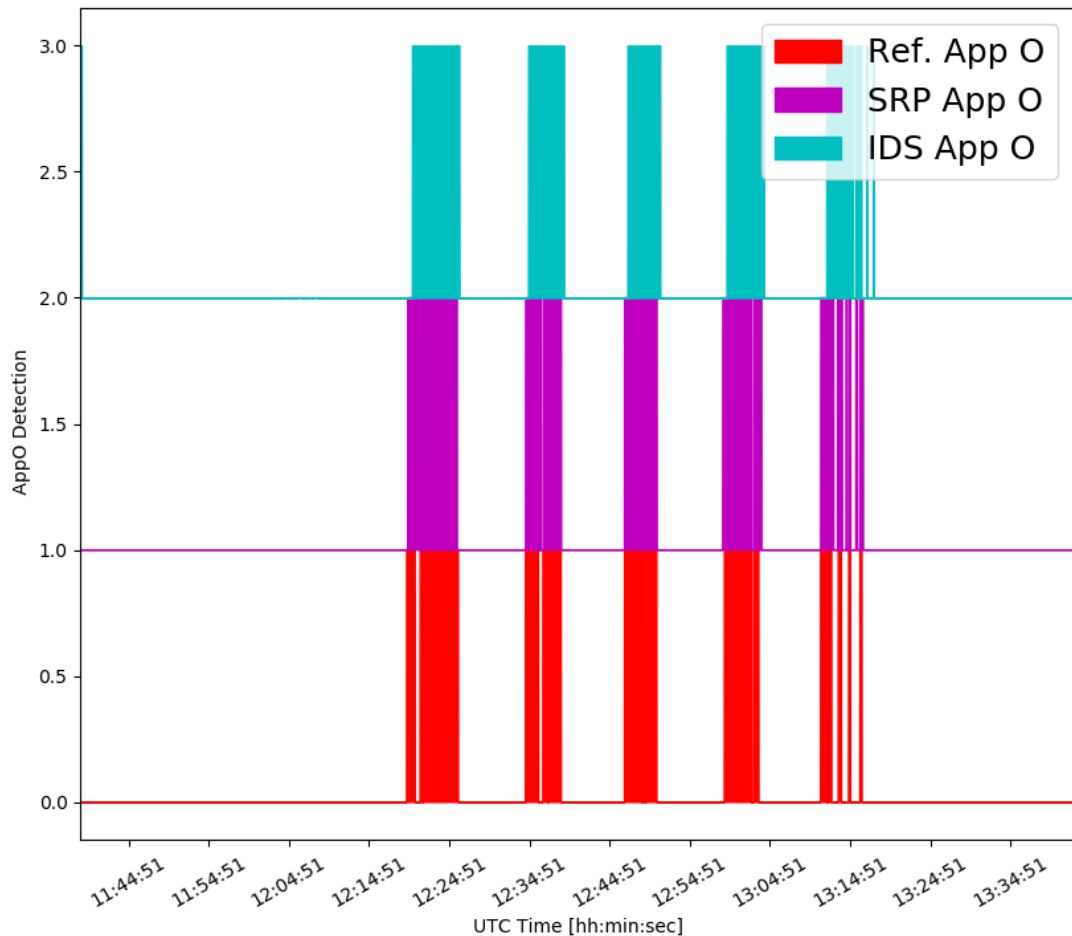


Figure 88: App O detection signals of DIDSs for the icing encounters of FT1476-1. From the bottom to the top: μP , SRP, IDS.

Table 10: Number of icing encounters for FT 1475-1 and number of IC /App. O Flags raised by each detector. Note that IID and PFIDS are not able to discriminate between App. C and App. O icing conditions.

	μP	IID	PFIDS	AIP	SRP	IDS
IC / APP O Flags	6 / 5	5 / -	5 / -	-	5 / 5	5 / 5

The response times reported in Table 11 show that DIDS are able to detect very fast each encounter, in particular SRP detected the conditions even before the μP probe. It is interesting to note that IID, even if not compliant to ED-103 response time, seems to detect App. O conditions faster than App. C, see Ref. [7].

The top plot in Figure 89 contains the altitude and indicated airspeed for the example encounter (IC3). It is clearly visible that the aircraft was intentionally descending into the (expected) icing conditions and climbing again out of these after a certain encounter time. The second plot (from top) shows the nominal drag estimation (based on clean aircraft zero-lift drag) and gives a direct impression about the performance degradation. In parallel, the IID detection output is given allowing a direct comparison of drag increase and IID detection performance. Note that the shown data are a result of the online IID calculation within the HIDS system

implementation directly fed with aircraft data/measurements. The third plot (from top) contains the information about the encountered icing conditions. The measured droplet size (MVD) and liquid water content (LWC) describe the atmospheric icing conditions (all drops, solid lines) with an additional information about the SLD part of the conditions (dashed line). The bottom plot contains the measured static air temperature as well as the averaged engine fan speed (left and right, assuming symmetric thrust conditions). During the descend into the icing conditions the temperature decreases significantly and increases again after leaving the conditions, indicating an atmospheric inversion layer. This allows a direct assessment about the icing encountered leading to airframe ice accretion and hence a performance degradation, together with the possibility to cross-check the detection reset with the flight through warm air and consequently de-icing. The averaged engine fan speed is directly linked to the total engine thrust and therefore gives an information about the forces applied to the aircraft in combination with the aerodynamic performance degradation.

During the encounter the IID was able to reliably detect the performance degradation shortly after the ice built up started. The confirmed detection remained every time until the aircraft left the conditions and was completely de-iced again. For these encounters, the time to restore the nominal flight performance and to reset the detection flag took approximately the same time as the aircraft stayed in the conditions itself. This shows the **great value of the IID because it reliably indicates the aircraft degradation being eventually critical for the aircraft operation and potentially unknown by the crew, even the icing conditions might be already left**. This is one of the keys related to the layered safety concept provided by SENS4ICE including the HIDS approach.

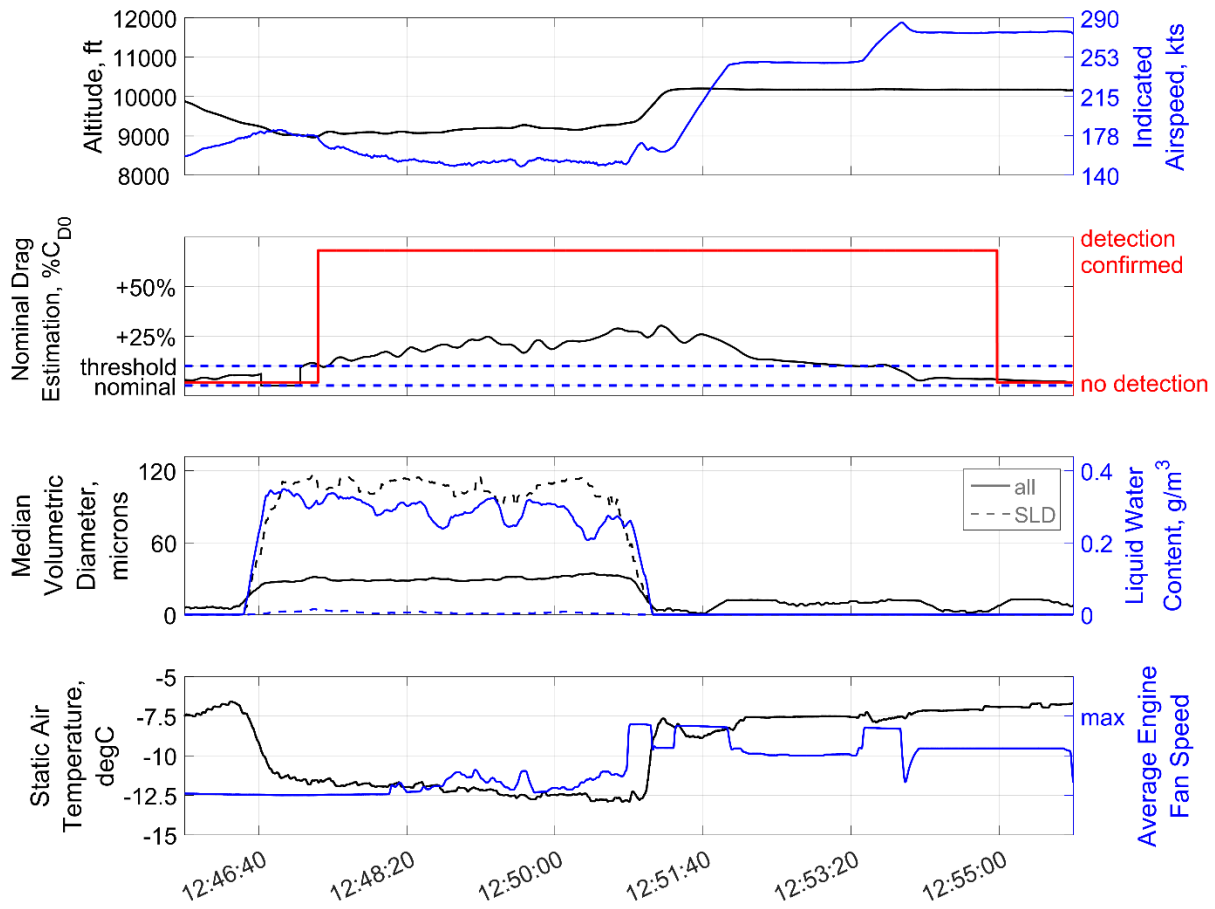


Figure 89: Time history of IID system performance during specific icing encounter from the first example flight (February 25th, 2023, 12:45:49 UTC to 12:55:49 UTC): altitude and indicated airspeed (top), nominal drag estimation and IID detection output (second plot), and MVD and LWC of encountered icing conditions (third plot) including the indication of the amount of SLD (dashed lines), and static air temperature and average engine fan speed (bottom); detection threshold at 10% relative drag increase; adjusted engine thrust model behaviour.

Table 11: IID and DIDSs response time for the 5 App O conditions of FT 1476-1.

IC	ICE START (μP)	ED103 Resp time [s]	IID ICE	IID Resp. time wrt μP	PFIDS ICE	PFIDS Resp. time wrt μP	SRP ICE	SRP Resp. time wrt μP	IDS ICE	IDS Resp. time wrt μP
1	12:19:37	15.66	12:22:08	02:31	12:19:49	00:12	12:19:34	-00:03	12:19:49	00:12
2	12:34:14	11.85	12:35:07	00:53	12:34:35	00:21	12:34:11	-00:03	12:34:24	00:10
3	12:46:38	10.58	12:47:21	00:43	12:46:48	00:10	12:46:34	-00:04	12:46:46	00:08
4	12:58:47	15.19	13:00:01	01:14	12:59:09	00:22	12:58:47	00:00	12:58:54	00:07
5	13:10:58	16.38	13:11:48	00:50	13:11:16	00:18	13:10:59	00:01	13:11:11	00:13

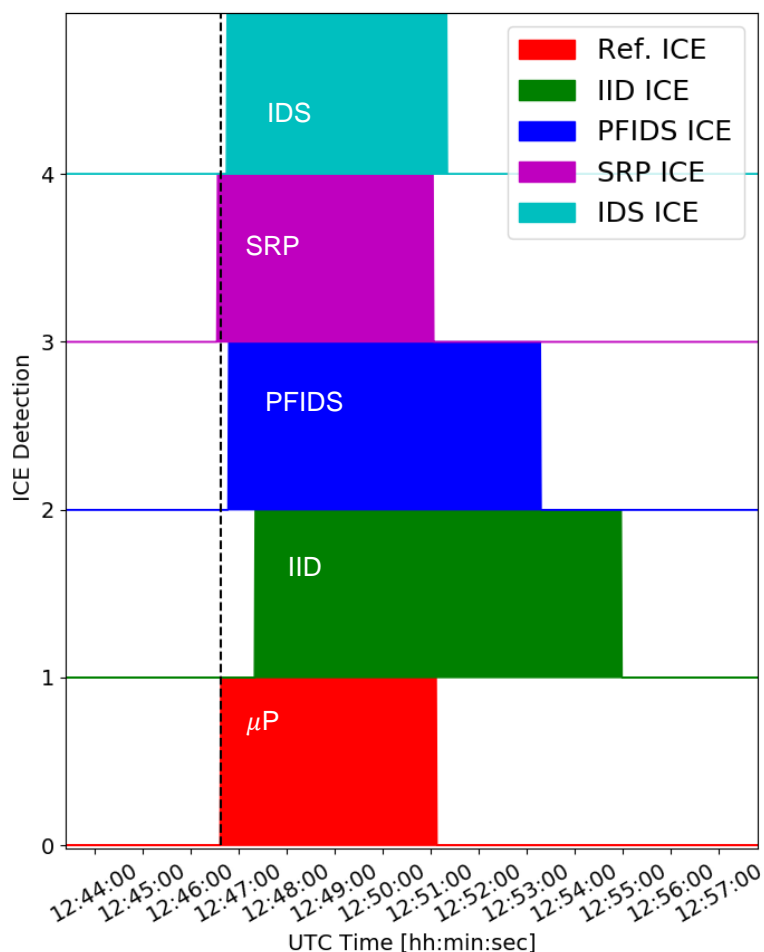

 Figure 90: Ice Detection signal of DIDSs and IID for IC3 of FT1476-1. From the bottom to the top: μP , IID, PFIDS, SRP, IDS.

Figure 90 shows that, if the DIDSs ICE flags dropped once the A/C exits the icing condition, the IIDS continued to detect performance degradation. Actually, Embraer engineers observed that the A/C left the clouds with moderate ice accreted on the unheated surfaces and that it entered in the new condition with still some ice. IIDS is thus able to detect a performance degradation due to remaining residual ice.

The Arbitration function checks also the reliability of DIDS and IID, in particular it creates a new IID ICE signal, called **IID ICE Valid**, based on the reliability of IID outputs and on the TAT value:



- if IID outputs are reliable and TAT < 5°C → IID ICE output is valid;
- if IID outputs are unreliable (for example when high lift devices are used and/or the landing gear is down) and/or the TAT ≥ 5°C → IID ICE output is not valid.

In order to keep an early ice detection and to monitor the A/C performance even when the A/C exits the icing clouds, the Arbitration flag encloses perfectly both DIDS and IID Ice flags (for S4I FT we used $\Delta t = 0$): the HIDS ICE flag is raised as soon as there is a DIDS detection and dropped when the IID ice flag drops. Moreover, the HIDS ICE flag can be equal to 2, if based on DIDS measurements (IAR or LWC), the IC can be considered as a severe IC, or it can assume a negative value if the encountered condition is an App O condition. Therefore, HIDS Arbitration output (i.e. HIDS ICE flag) can assume the following values:

- 0: no ice
- 1: ice
- 2: severe ice
- negative sign: App O conditions

The HIDS **Arbitration status** (the last subplot in Figure 91 and Figure 92) provides some details on how the Arbitration result has been built:

- Arbitration status = 0 → both DIDS and IID outputs are unavailable
- Arbitration status = 1 → only DIDS outputs are available and reliable
- Arbitration status = 2 → only IID outputs are available and reliable
- Arbitration status = 3 → both DIDS and IID are available and reliable

Thanks to this approach, even if only one detection source is available, HIDS will provide ice detection information.

Figure 91 and Figure 92 report the results of HIDS arbitration function for each couple DIDS/IID. As for the previous flight, HIDS ICE flag encloses perfectly both DIDS and IID Ice flags.

Based on PFIDS IAR measures, the 5 conditions can be considered as severe conditions, HIDS flag = 2, see Figure 91 on the left. For the couple SRP/IID and IDS/IID, the HIDS ice flag switches from 1 to -1, since the two detectors classified these encounters as App. O conditions.

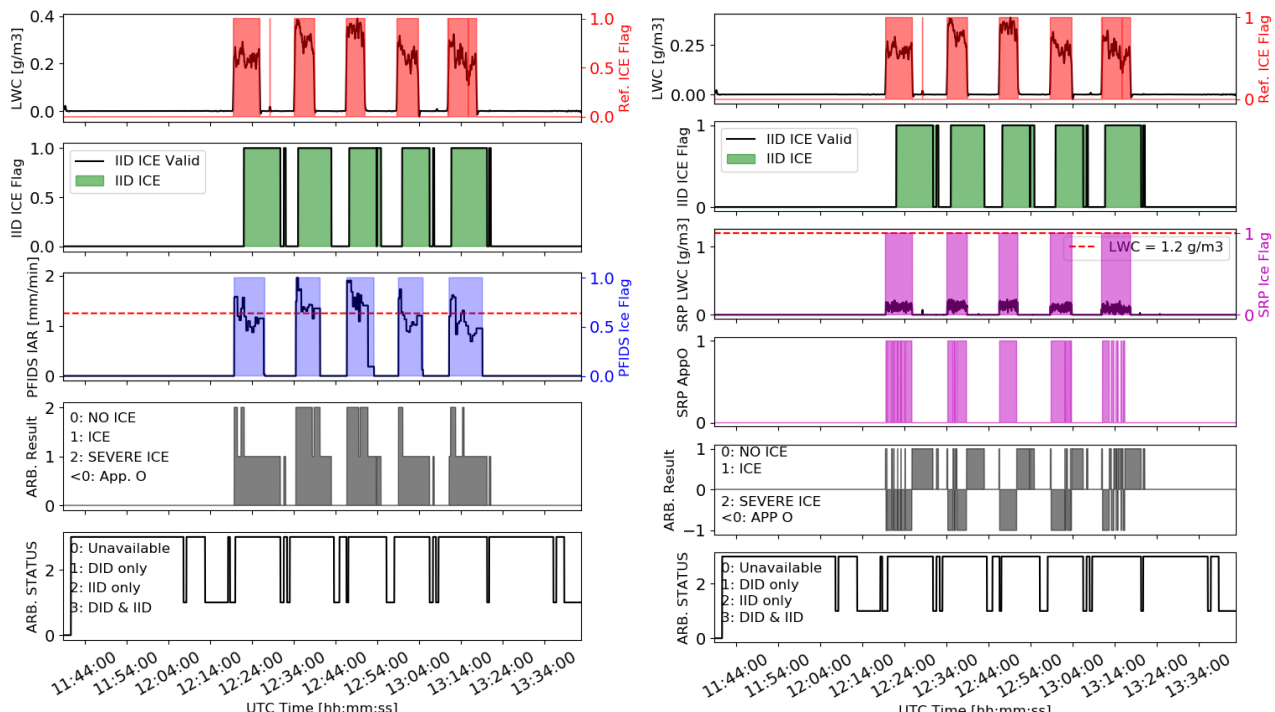


Figure 91: Results of HIDS arbitration for the couple PFIDS/IID, on the left, and the couple SRP/IID, on the right. From the top to the bottom: LWC curve and μ P ice flag; IID ice flag; DID IAR or LWC curve and ice flag; DID App O flag (not available for PFIDS since it cannot discriminate); HIDS Arbitration results; HIDS Arbitration status.



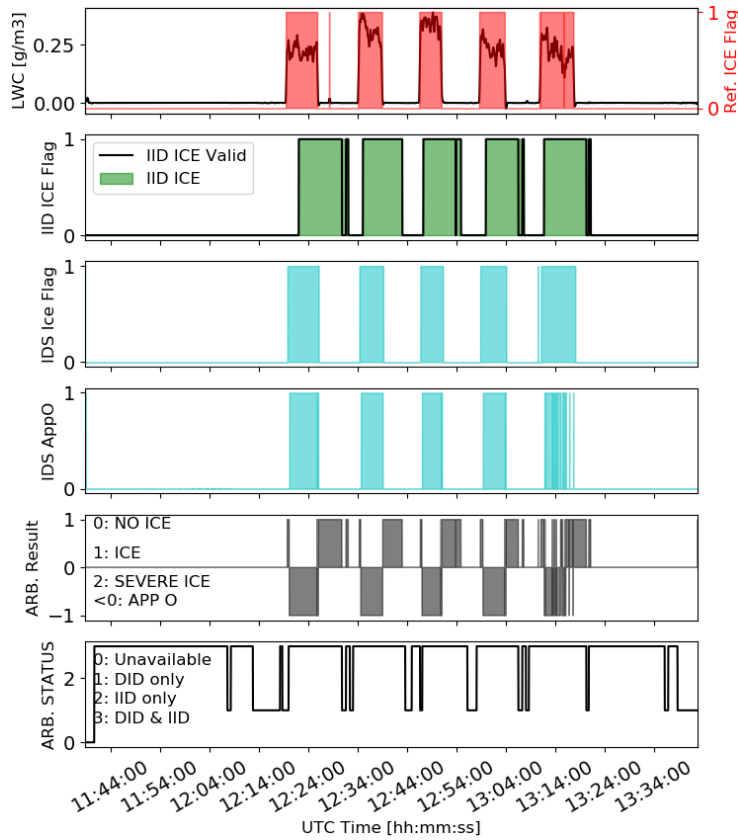


Figure 92: Results of HIDS arbitration for the couple IDS/IID. From the top to the bottom: LWC curve and μP ice flag; IID ice flag; IDS ice flag; IDS App O flag; HIDS Arbitration results; HIDS Arbitration status.

6.4.2. European Flight Test Campaign

A detailed evaluation of results from the European flight test campaign is given in Ref. [7]. In this section one flight of the campaign (flight as230018) is shown and results are briefly discussed. During this flight several icing conditions were encountered, including App C and App O conditions. The results of the analysis presented were obtained by replaying offline the whole flight test scenario by using post-processed data for indirect detection, microphysics and direct sensors.

In Figure 93 are reported A/C data, μP data and IID main outputs for the flight as230018. Note that for HIDS evaluation the IID outputs obtained by considering the 10% threshold for relative drag increase are used.

Flight as230018 lasted more than 4 hours and several icing clouds were encountered as demonstrated by RICE probe, the legacy ice accretion detector, and the μP measures. Actually, the ATR 42 flew through some clouds characterized by the presence of SLD and Ice Crystal too.

For safety reason, SAFIRE's pilots activated the Ice Protection System (pneumatic boots) when the A/C entered in icing conditions and ice accretion was visible on the “visual clue” outside the cockpit windows. After a while in icing conditions, the pilots exited the cloud by reducing the altitude in order to fly in warm air layer to ensure a full de-icing of the aircraft. The IPS were switched off during this phase.

Such de-icing cycle occurred 8 times during the flight, see the first subplot in Figure 93.

Indeed, a good correlation between the indirect ice detections and the period of activation of the ATR 42 pneumatic boots can be observed, meaning that the indirect ice detection matches the pilots' observations.

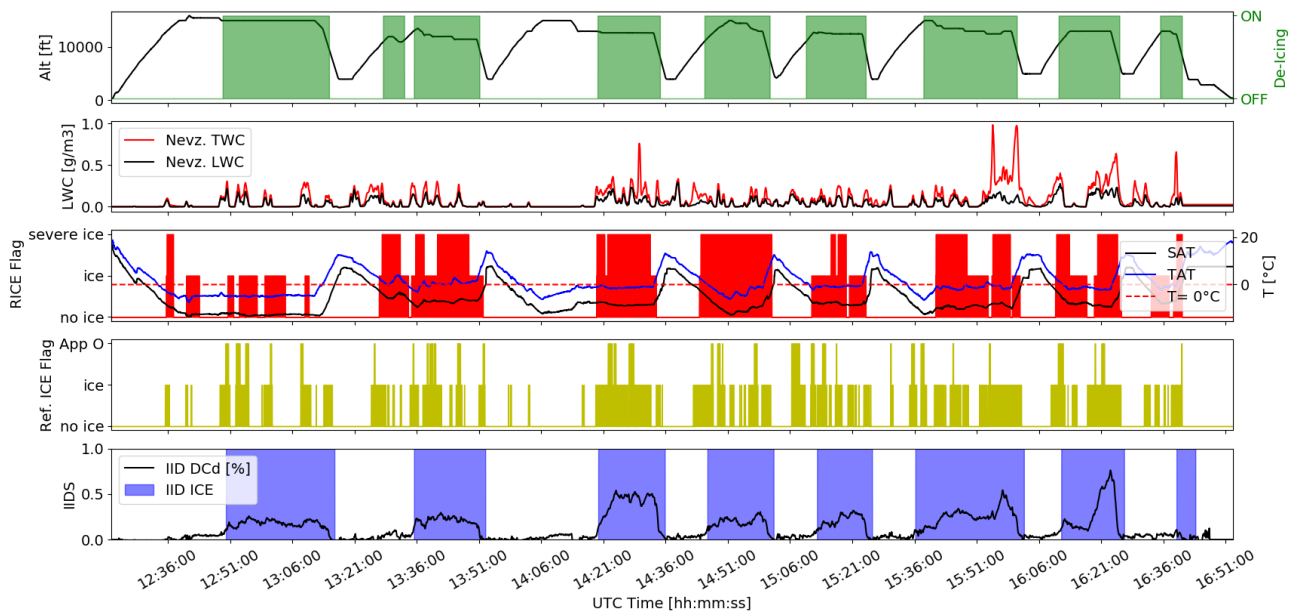


Figure 93: A/C data, μP data, reference icing flags and IID outputs for the flight as230018. From the top to the bottom: A/C altitude time history and IPS activation; Nevzorov measurements of LWC and TWC; Temperature time history (both SAT and TAT) and RICE reference probe ice flags; μP ice flags; IID relative drag increase and ice flags.

In Table 12 a summary of the number of IPS systems activations (both wings and horizontal tail IPS), the RICE reference probe detections, μP ice flags and App O flags is reported. Note that the RICE probe signals were considered severe for the following evaluation and assessment when the ice thickness on the probe is above 0.02 inch, corresponding to engineering judgement. As already stated, because of the nature of the encountered icing clouds, μP probes detected several very short icing encounters.

Table 12: Summary of the number of IPS activation, reference ice flags and indirect ice detection for the flight as230018.

IPS activation	RICE ice detection	RICE severe ice	μP ice detection	μP App O detection	IID ice detection
9	20	11	251	34	8

As illustrated in Figure 94, all the DIDSs were able to detect the icing encounters. As expected, the AMPERA icing flags are well correlated with the μP ones, while LILD and IID match up the RICE signals. The FOD detected as well several icing encounters, in agreement with the μP flags, but it was not able to hold the ice signal and to properly detect the exit from the cloud.

In effect, the FOD detection algorithm is based on the observation of abrupt temperature changes at the sensor surface due to the ice accretion. Thus, the exit from the icing cloud should correspond to a temperature decrease due to the convection heat flux. During the European flight test, because of the heterogeneous nature of the icing clouds, the temperature did not rise to its equilibrium temperature and therefore the convection could not cause an abrupt decrease of the temperature. For this reason, FOD developers preferred to modify the detection algorithm in order to detect each temperature changes and to display the ice presence in a discrete manner.

Neither LILD, nor FOD, detected the presence of SLD during this flight.

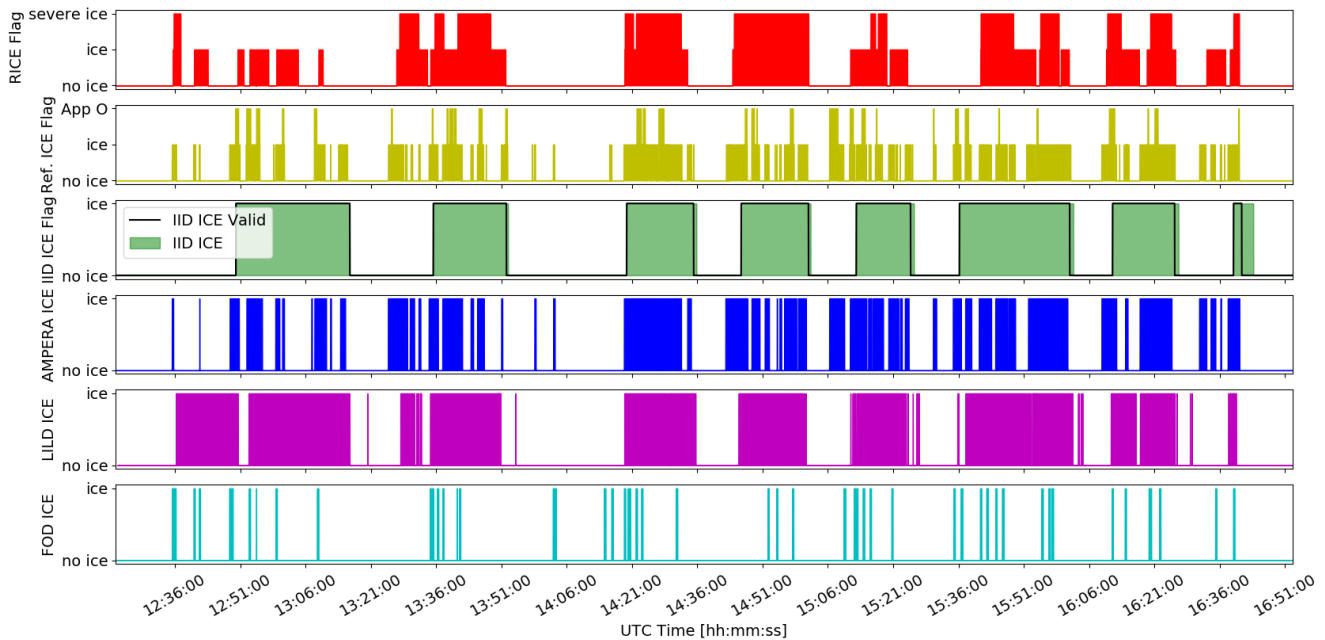


Figure 94: Ice Detection signal of DIDSs and IID for the icing encounters of flight as230018. From the top to the bottom: RICE (reference), μP , IID, AMPERA, LILD, FOD.

For this flight, the analysis is focused on two different time intervals:

1. IC1: [14:19:00 – 14:28:00] UTC time
2. IC2: [14:42:00 – 15:01:00] UTC time

These time intervals are characterized by two different icing encounters, detected by both RICE reference probe and μP . The two conditions are characterized by SLD presence.

Figure 95 shows the third encounter of this flight, which had a different profile than the previous ones. This time, the icing conditions led directly to a significant ice formation on the airframe (indicated through the jump in the reference ice probe signal) which is directly correlated with the strong icing situation also produced by SLDs in the air. The aircraft performance is continuously degraded until it reaches more than 50% relative drag increase compared to the nominal value. This degradation persists although the icing situation changes to even larger drops (see bottom plot at around 14:29 UTC). Due to the fact, that the de-icing boots were activated during the encounter, the aircraft was protected and a further aerodynamics degradation was prevented. The IID directly confirmed the ice formation on the airframe through the monitoring of the aircraft's flight performance within less than a minute after the encounters started. For this encounter pictures from the cameras indicating the airframe icing situation are available. Figure 96 show a specific view on the leading edges of left and right wing (from below) together with the horizontal tail for different times. At 14:19:25 UTC when the encounter started, the airframe was free of visible ice accretion. But around two minutes later and a confirmed IID detection information, the airframe shows an icing layer which on the wings is already broken from the active de-icing system. During the next minutes the formation does not really change in total and although the boots allow to remove some ice, new formations built up, which then cause almost no change in the estimated drag resulting from the IID. It is interesting to see that at around 14:29 UTC, when large drops were encountered, the wings seem to have less ice than before – resulting in the reduction of the additional drag estimated by the IID between 14:29 UTC and 14:31 UTC – because of presumably a good effectivity of the protection system. The drag rises again shortly after, where a more glaze ice looking ice formation is visible on the aircraft (14:32:37 UTC in Figure 96), which is presumably a result of the ongoing SLD icing situation. Anyway, this result shows that a currently present encounter might not have instantaneously a noticeable adverse effect on the aircraft aerodynamics. Monitoring only the icing conditions might consequently not give a correct indication on the criticality of the encounter even if the situation looks dangerous in terms of water drops in the air, but the continuous monitoring of the ice formation and corresponding aerodynamics degradation will give the comprehensive view on the current situation required for a safe aircraft operation. After descending and passing through the 0°C temperature layer, the aircraft got free of ice again (14:36 UTC).

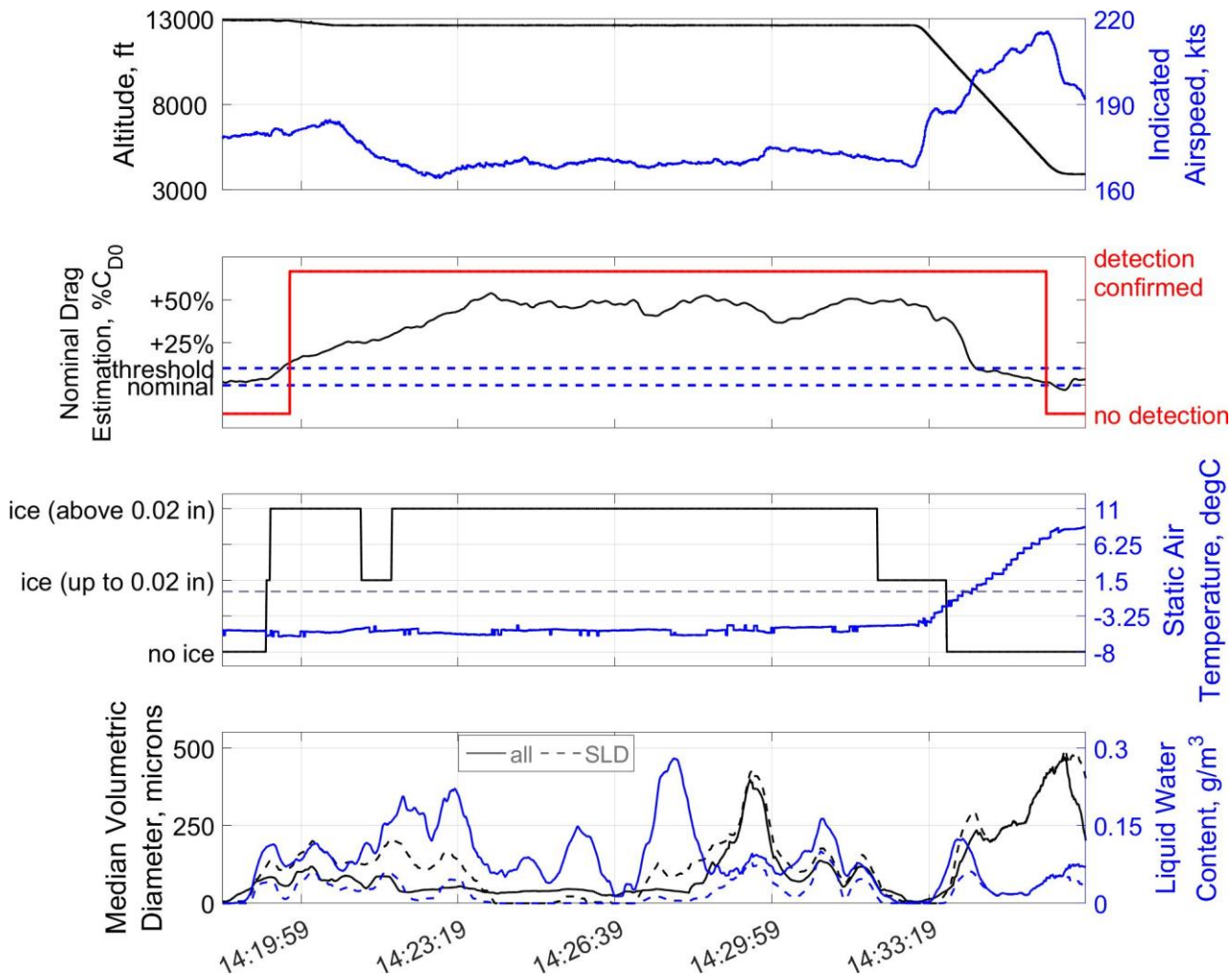


Figure 95: Time history of IID system performance during specific icing encounter from the first example flight (April 24TH, 2023, 14:18:20 UTC to 14:36:40 UTC): altitude and indicated airspeed (top), nominal drag estimation and IID detection output (second plot), ice built-up on reference accretion ice sensor and static air temperature (third plot), and MVD and LWC of encountered icing conditions (solid line) including the indication of the amount of SLD (dashed lines) (bottom); **updated detection threshold at 10% relative drag increase.**

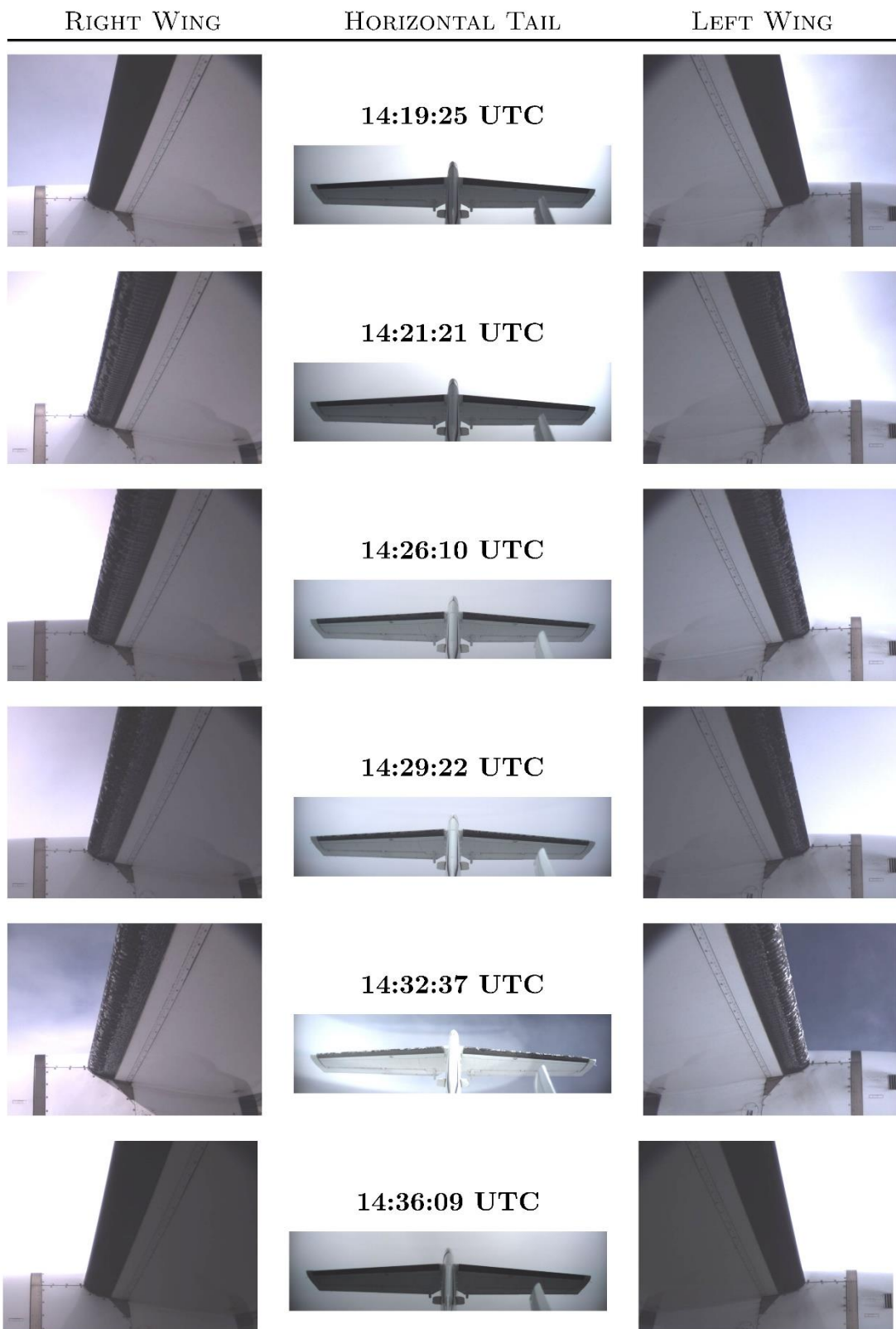


Figure 96: Evolution of ice accretion on the airframe during icing encounter: camera views on left & right wing and horizontal tail for specific moments during flight (increased brightness and contrast); corresponding to encounter and IID detection output given in Figure 95; credit Safire/ SENS4ICE project.

In Figure 97 are reported for the selected time interval [14:19:00 – 14:28:00] UTC, the LWC, MVD, SAT and TAS time histories, reference icing flags and the concentration of aspherical particles (LAS N), figure on the left, and the ice detection of DIDSs and IID w.r.t. the reference ones, figure on the right.

It is important to observe that the LAS N is always lower than 1/L (i.e. 1 per litre, corresponding to 0.001 per cm³), this means that the MVD evaluation was not affected by the presence of ice crystals, see SENS4ICE D4.3 [8].

Average values of LWC, MVD, SAT, ALT and TAS have been used to evaluate the ED103 theoretical IAR and response time for the encountered icing condition. This allows to compare DIDSs performances.

The detectors response time w.r.t. RICE reference probe, the legacy ice detector, for IC1 are reported in Table 13. Note that in this Table the IID response time is reported as well even if ED103 is addressed only to direct detectors.

IID raised the icing flag 30s after the RICE reference, while all the DIDS were more sensitive and raised an ice flag before RICE, in agreement with the μP flag.

Table 13: IID and DIDSs response time for the icing encounter during the time interval [14:19:00 – 14:28:00] UTC of flight as230018.

ED103 Resp. time [s]	ED103 IAR [mm/min]	μP ICE FLAG [hh:min:sec]	RICE ICE FLAG [hh:min:sec]	IID Resp. Time w.r.t. RICE [s]	AMPERA Resp. Time w.r.t. RICE [s]	LILD Resp. Time w.r.t. RICE [s]	FOD Resp. time w.r.t. RICE [s]
26	0.70	14:19:04	14:19:16	30s	-7s	-1s	-7s

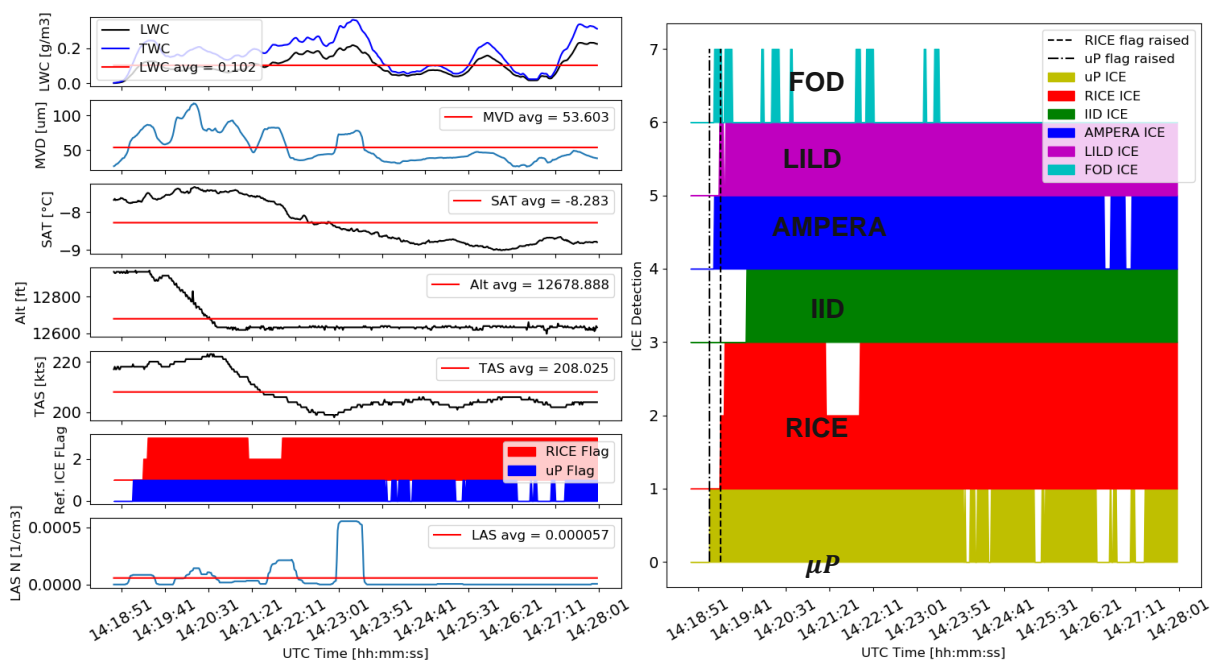


Figure 97: On the right, μP , A/C data and reference ice flags during the time interval [14:19:00 – 14:28:00] UTC of flight as230018. On the left: DIDSs, IID and reference ice flags during the time interval [14:19:00 – 14:28:00] UTC of flight as230018.

Similar results for the indirect ice detection can be obtained for the next encounter between 14:42:29 UTC and 15:02:39 UTC given in Figure 98 (time history plot) and Figure 99 (camera footage). During the climb to FL140 the aircraft entered icing conditions leading to an airframe ice accretion indicated by the reference icing probe. At around 14:46 UTC, the aircraft's wings and empennage are visible free of ice, which means that ice formation was presumably only present on the unprotected surfaces resulting in less than 10% relative drag deviation. But, during the following climb the aircraft performance was notably degraded and the IID correctly announced the performance loss. At 14:49:15 UTC the wings' leading edges had some ice formation



corresponding to the around 25% increase in the nominal drag estimation. The situation maintained almost constantly in terms of ice formation and degradation until the aircraft descended after 15:00 UTC into warmer air to remove the ice completely. Note that this encounter shows the advantage of the IID working throughout all flight conditions resulting in a fast and reliable information.

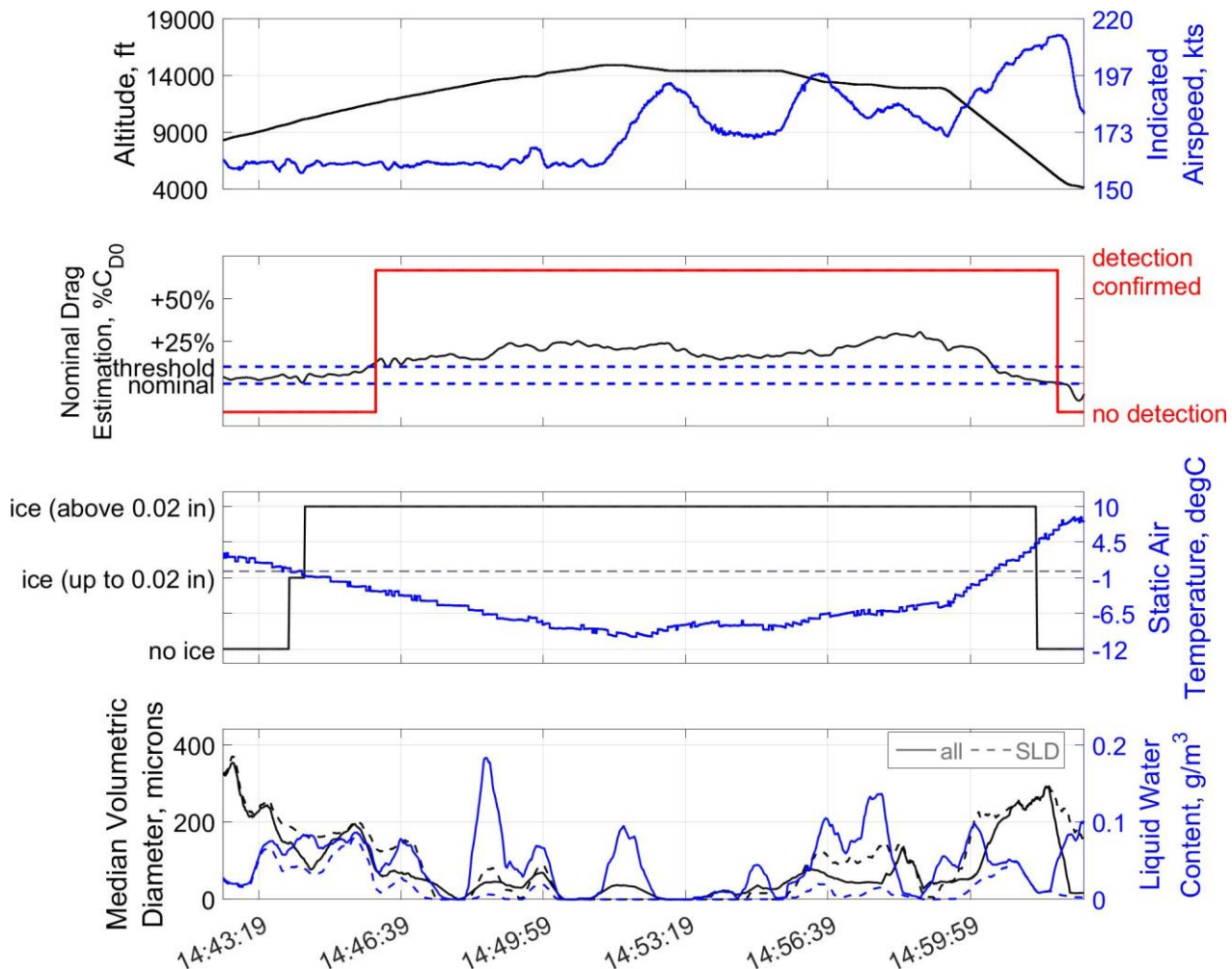


Figure 98: Time history of IID system performance during specific icing encounter from the first example flight (April 24TH, 2023, 14:42:29 UTC to 15:02:39 UTC): altitude and indicated airspeed (top), nominal drag estimation and IID detection output (second plot), ice built-up on reference accretion ice sensor and static air temperature (third plot), and MVD and LWC of encountered icing conditions (solid line) including the indication of the amount of SLD (dashed lines) (bottom); **updated detection threshold at 10% relative drag increase.**

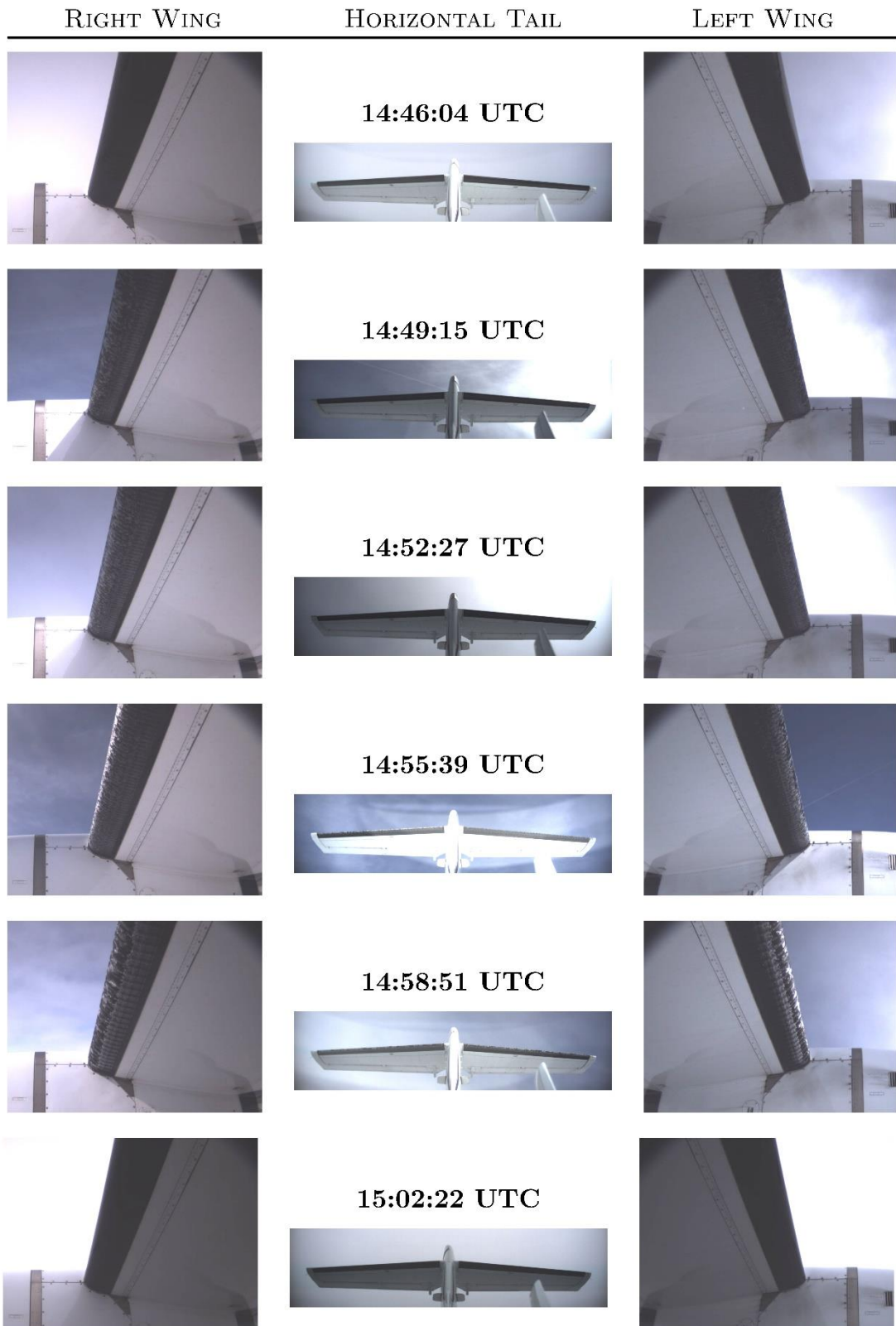


Figure 99: Evolution of ice accretion on the airframe during icing encounter: camera views on left & right wing and horizontal tail for specific moments during flight (increased brightness and contrast); corresponding to encounter and IID detection given in Figure 98; credit Safire / SENS4ICE project.

In Figure 100 are reported the time histories of LWC, MVD, SAT, TAS, reference ice flag and the concentration of aspherical particles (LAS N), figure on the left, and, the ice detection of DIDSs and IID w.r.t. the reference ones over the time interval [14:42:00 – 15:01:00] UTC, figure on the right.

Detectors response time w.r.t RICE reference are indicated in Table 14. IC2 is characterized by a lower IAR than IC1, this explains the higher response time of ice accretion detectors, such as LILD, FOD and IID as well. Once again, AMPERA, which is an atmospheric sensor, guaranteed an early detection in agreement with μP ice flag.

ED103 Resp. time [s]	ED103 IAR [mm/min]	μP ICE FLAG [hh:min:sec]	RICE ICE FLAG [hh:min:sec]	IID Resp Time wrt RICE [s]	AMPERA Resp Time wrt RICE [s]	LILD Resp Time wrt RICE [s]	FOD Resp time wrt RICE [s]
60	0.30	14:42:38	14:44:03	122	-95	84	486

Table 14: IID and DIDSs response time for the icing encounter during the time interval [14:42:00 – 15:01:00] UTC of flight as230018.

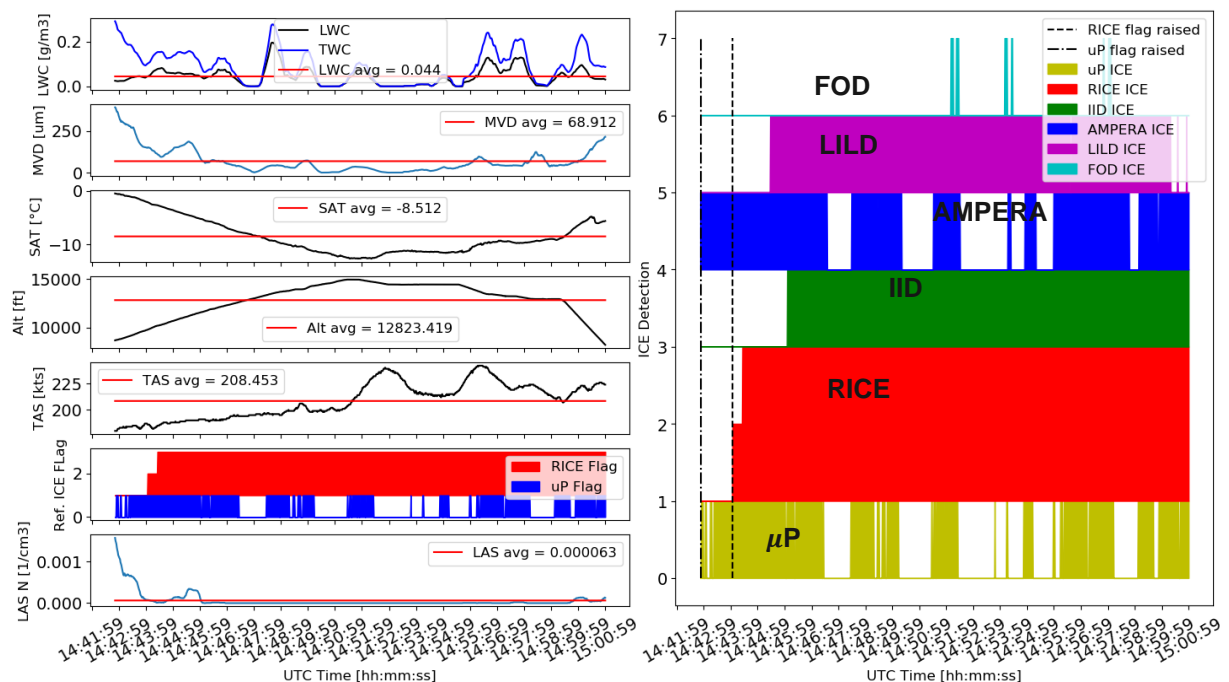


Figure 100: On the right, μP , A/C data and reference ice flags during the time interval [14:42:00 – 15:01:00] UTC of flight as230018. On the left: DIDSs, IID and reference ice flags during the time interval [14:42:00 – 15:01:00] UTC of flight as230018.

From Figure 101 to Figure 103, the results of HIDS arbitration, coupling each DIDS with IID, are reported. As for the North American flight campaign, HIDS ICE flag encloses perfectly both DIDS and IID Ice flags ($\Delta t = 0$ s) in order to guarantee an early detection based on DIDS signals, and the continuous monitoring of A/C performances provided by IID even after the exit from the icing clouds.

The **IID ICE Valid** signal used by the arbitration function, as explained in SENS4ICE D4.2 [7], truncates detections above the upper limit TAT_{cr} . In the EU campaign, this value is $10^\circ C$. Note that this limit [TAT_{cr}] should ideally be provided by the aircraft manufacturer, according to the aircraft performance.

Figure 101 shows a very good correlation between AMPERA TWC and Nevzorov measurements, while both LILD and FOD provided higher IAR values than expected (theoretical) ones, see the second subplot from the top of Figure 102 and Figure 103. Actually, for both detectors, the results of the arbitration indicates some severe icing encounters (i.e. $IAR > 1.25 \text{ mm/min}$).

For FOD, the IAR is evaluated indirectly, by resolving the classical *Messinger* balance equation. The observed overestimation could be due again to the heterogeneous nature of the icing clouds and a possible overestimation of the convective heat transfer coefficient.

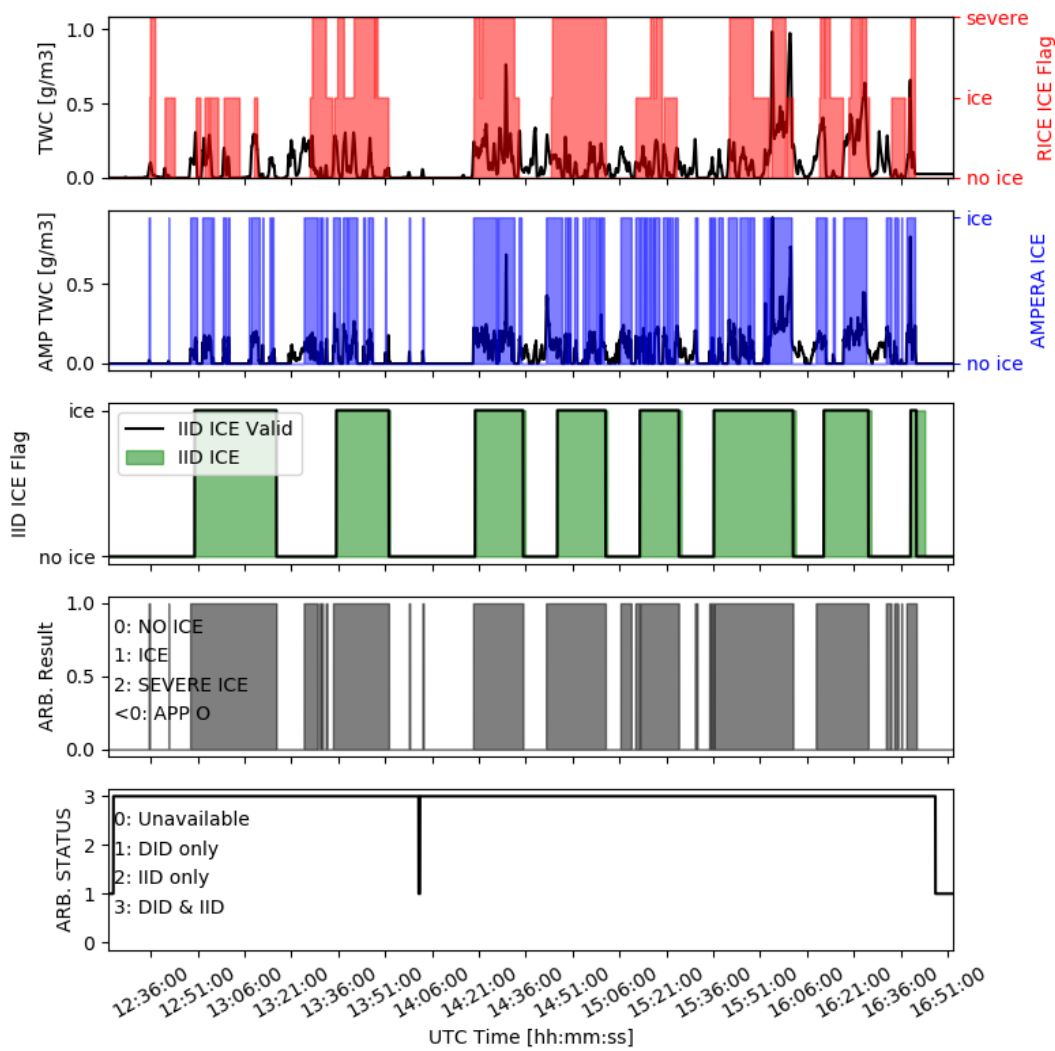


Figure 101: Results of HIDS arbitration for the couple AMPERA/IID. From the top to the bottom: TWC curve and RICE ice flag; AMEPRA TWC measurements and ice flags; IID ice flags; HIDS Arbitration results; HIDS Arbitration status.

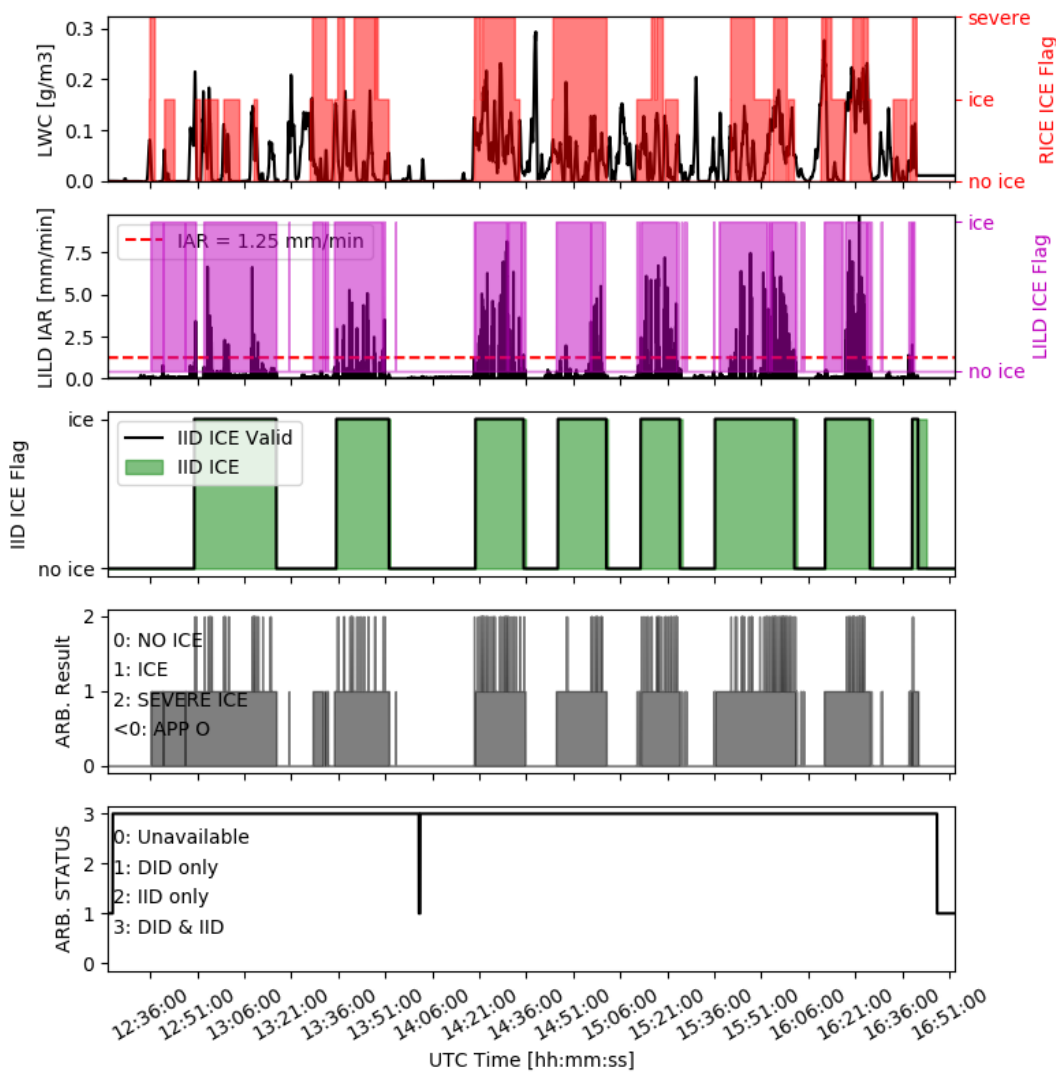


Figure 102: Results of HIDS arbitration for the couple LILD/IID. From the top to the bottom: LWC curve and RICE ice flag; LILD IAR measurements and ice flags; IID ice flags; HIDS Arbitration results; HIDS Arbitration status.

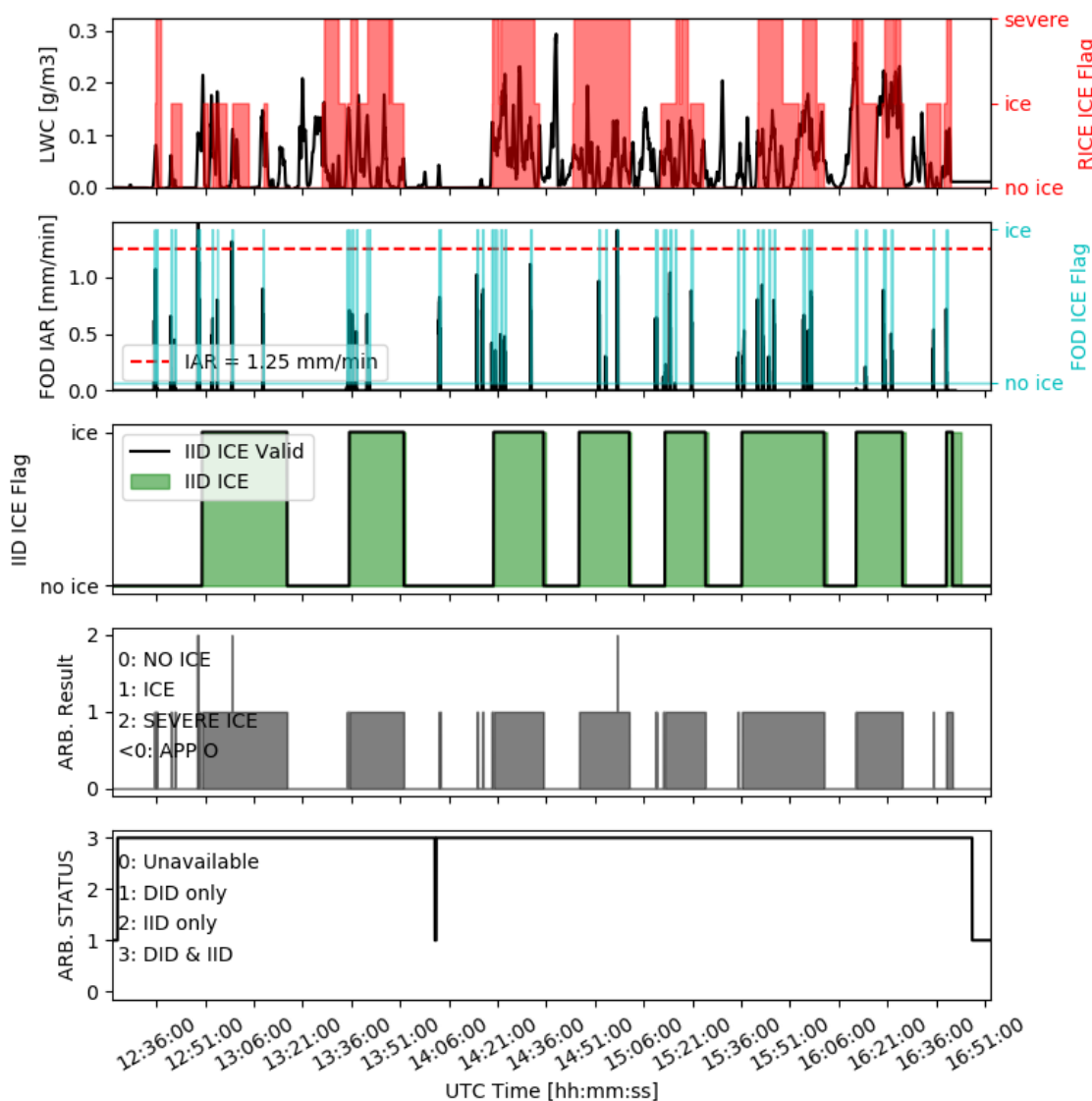


Figure 103: Results of HIDS arbitration for the couple FOD/IID. From the top to the bottom: LWC curve and RICE ice flag; FOD IAR measurements and ice flags; IID ice flags; HIDS Arbitration results; HIDS Arbitration status.

6.5. Further Development, Maturation and Exploitation

The results of the two SENS4ICE flight test campaigns are very promising: HIDS, indeed, appears to be a more robust and reliable ice detection system than the legacy one. Association of direct sensors with the IID makes the HIDS the only system that can perform both an early ice detection, and a continuous monitoring of remaining ice, after leaving the icing clouds.

Moreover, direct detection may be limited because it measures only very local characteristics of the flow or accretion, therefore global drag increase effects measured by IID can reduce false alarms and consolidate the early detection, and can be used to alert the pilot only whenever the A/C performance is reduced by the encounter condition. In order to properly consolidate the hybrid output the delay applied to the DIDS ice signal to wait for the indirect ice detection confirmation shall be adjusted. This can only be done once the A/C, the indirect ice detection and the direct ice detector performances are known. In this way, the IPS activation can be strongly optimized. Indeed, HIDS could enable significant reduction in fuel consumption thanks to a more efficient use of IPS, associated to the monitoring of remaining ice.



This requires to determine the IID detection thresholds: after the confirmed detection of the performance degradation, safety margins for envelope protection become relevant. These are subject to the individual aircraft and must be defined accordingly. With a feedback of this information to the flight management system, further flight operation can be planned and optimized, in order to maintain the original flight plan if possible. The performance degradation, and respectively the drag increase further, mainly indicated the presence of ice but does not directly allow a correlation to the ice formation itself. As the certification is mainly related to an admissible ice formation for certified icing operations, the information about a performance degradation must be transferred to a potentially admissible impact on flight performance for icing operations.

Probably, such an innovation in the ice protection domain will require a new certification approach, to be developed in collaboration with the certification authorities and aircraft manufacturers.

7. Conclusions and Recommendations

7.1. TRL Progress in SENS4ICE

Significant progress was made on technology maturation during the SENS4ICE project. A summary of the TRL progression is illustrated in Table 15. Most technologies started at low TRL, mostly TRL2-4, and made significant progression to higher TRLs, in many cases TRL6, which is a major achievement of the SENS4ICE project.





Table 15: SENS4ICE technology maturation progression in terms of TRLs.

Technology	TRL at project start (January 2019)	TRL at project mid-term (Dec 2020)	TRL objective at project end	TRL App C detection at project end	TRL App O detection at project end	TRL App O discrimination at project end
Atmospheric Hydrometeor Detection based on Electric measurement (AHDEL)	TRL1	TRL2-3	TRL5	TRL4	TRL4	TRL4
Atmospheric Icing Patches (AIP)	TRL2	TRL3	TRL5	TRL5-6	TRL5-6	TRL5-6
AMPERA	TRL4	TRL4-5	TRL5	TRL5-6	TRL5-6	-
Appendix O Discriminator (AOD)	TRL2	TRL2	originally TRL5, stopped at TRL3	-	-	TRL3
Aircraft Flight Performance Monitoring (AFPM/IID)	TRL3-4	TRL3-4	TRL5	TRL5	TRL5	-
Cloud Multi Detection Device (CM2D)	TRL5	TRL5	TRL6	TRL6	TRL6	TRL6
Fibre Optic Ice Detector (FOD)	TRL3-4	TRL5	TRL6	TRL6	TRL6	TRL4
Local Ice Layer Detector (LILD)	TRL3-4	TRL3-4	TRL5-6	TRL6	TRL6	TRL3
Primary in-Flight Icing Detection System (PFIDS)	TRL6	TRL6 (TRL4 for XTAL and IAR functions)	TRL6	TRL6	TRL6	TRL3
Nowcasting	TRL2	TRL3-4	TRL5	TRL5	TRL5	-
Collins Ice Differentiator System (IDS)	TRL2	TRL4	TRL6	TRL6	TRL6	TRL6
Short Range Particulate Sensor (SRP)	TRL3	TRL6	TRL6	TRL6	TRL6	TRL6



7.2. Direct and Remote Ice Detection Technology Conclusions

Direct and remote ice detection technologies particularly for SLD icing were further developed, considerably matured and successfully demonstrated, for the direct sensors in icing wind tunnels (IWT) and for direct and remote ice detection in natural icing conditions flight campaigns. Intense and significant coverage of relevant icing conditions was achieved for IWT and flight campaigns including valuable SLD encounters, while the certification envelope for Appendix O is multi-dimensional and much larger. All detection technologies performed well during the flight demonstration and generally exhibited robust and timely ice detection behaviour. For the satellite-based approach the evaluation of the detection tool in relevant icing conditions is promising, suggesting that this remote approach, after further maturation, can be exploited for applications supporting aviation meteorology. A major step for increasing technology readiness (TRL) for almost all technologies under development was achieved. The TRL was increased up to TRL5 in several cases and even TRL6 for many of the technologies. The demonstrated novel ice detection technologies facilitate broad and promising applications for many different air vehicle types (including UAV, UAM and any unconventional future air vehicles including greener aviation) and several applications including ensuring operational safety and supporting certification activities. This is particularly the case for many of the novel technology due to low size/low weight/ low power properties. Furthermore, the novel detection technologies support the efficiency optimization for future smart ice protection systems. However, further research/ development/ testing in enhanced icing wind tunnels and in natural icing conditions in flight is required for covering the full range of App O, specifically freezing rain, for maturing icing detection and discrimination technologies and identifying path for certification.

7.3. Hybrid and Indirect Ice Detection Conclusions

During the flight test campaigns in natural icing conditions with two different aircraft types, enough data about the individual direct detectors performance as well as the indirect ice detection system was gathered in order to make a first assessment of the hybrid approach and make some relevant conclusions.

Association of direct sensors with the indirect ice detection (aircraft performance monitoring) makes the HIDS (hybrid ice detection system) the only system that can perform both an early ice detection, and a continuous monitoring of remaining ice, after leaving the icing clouds.

These characteristics could make the HIDS a possible Primary Ice Detection System. As illustrated in Figure 104, HIDS could offer both the control and the monitoring of A/C IPS: when DIDS detects an icing encounter the IPS shall be switched on, then, the indirect ice detection continuously monitors the IPS efficiency. If a performance degradation is detected after the exit from the icing clouds, some residual ice is still present on the airframe. This could be due to an inefficiency of IPS or to ice accretion on unprotected surfaces, for example due to SLD or runback ice. Pilots are then aware of the real performance of the aircraft, and can apply corrective actions if needed.

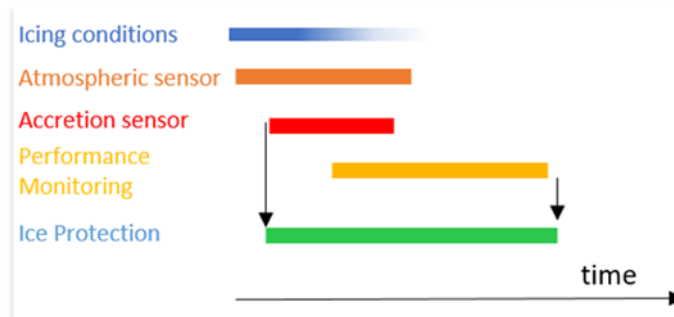


Figure 104: Schematic activation and monitoring of IPS provided by HIDS.

The main conclusions about the HIDS can be summarized as follows:

- The coupling of each direct ice detector with the indirect ice detection algorithm, through HIDS Arbitration function, gives extensive information on the aircraft status during an icing encounter, since it provides details on the icing conditions, ice accretion and remaining aircraft capabilities.





- Direct and indirect ice detection are not directly comparable but complementary technologies: direct ice detection technologies allow detecting icing conditions or local ice accretion fast and reliably, whereas the indirect ice detection methodology uses the aircraft as a sensor and gives an information about the performance degradation after ice formation.
- Preliminary analyses of flight test data show that the direct detection technologies tested are very promising and demonstrate a good agreement with ED103B standards, in particular regarding response time.
- The indirect ice detection was able to announce the performance degradation during all icing encounters of the SENS4ICE flight test campaigns. Although the algorithm is only reactive to conditions where the flight performance is already degraded due to ice accretion on the aircraft surfaces, it provides a high potential for applications where no direct sensing technology could be applied or is too complex or expensive, like smaller aircraft of the general aviation, unmanned aerial vehicles or new advanced air mobility vehicles. It further allows a reliable operational envelope monitoring for envelope protection and flight performance calculations, (e.g., endurance and range) if the reserves are limited.
- During flight testing, the indirect ice detection algorithm and the hybrid detection approach have shown their advantages for application on new and existing aircraft.
- Certification is mainly related to demonstration of safe operations in the icing environment or successful sense-and-exit operations. SENS4ICE flight test results have shown that especially for SLD conditions, the sensing with direct detection technologies is still a challenging task. Thanks to the ice detection approach developed within SENS4ICE, which allows more comprehensive information on the encountered icing situation and the aircraft capabilities, aircraft operations throughout the wide App. O envelope might be possible. Nevertheless, the hybrid ice detection approach is currently not reflected by the certification rules and this would require an agreement on acceptable mean of compliance.

With the SENS4ICE project, via the development of HIDS and the analysis of flight test campaign results, a big step to a more comprehensive view on the aircraft icing has been done.

7.4. SENS4ICE Recommendations

Based on the SENS4ICE project results, the following recommendations for future research programmes and activities can be made:

- Particularly for Appendix O/ SLD icing the conditions differed substantially for the two SENS4ICE flight campaigns. In general, the observations of atmospheric conditions impose the need for improvements of the physical understanding and forecasting/nowcasting capabilities:
 - Further extensive data collection with enhanced icing wind tunnels and in natural icing conditions in flight is required as sufficient data is not available today specifically for freezing rain.
- A further use and analysis of obtained natural icing flight test data during SENS4ICE is required beyond the scope of the project. This will provide valuable insights and knowledge gain for understanding of aircraft icing, including a detailed analysis of the camera images collected during flight.
- Enhancing aviation icing safety including for rare SLD conditions may involve revolutionary hybrid approach including novel detection technologies – addressing the challenge of detecting few large droplets/ low liquid water content:
 - further research/ development/ testing of detection technologies in enhanced icing wind tunnels and in natural icing conditions in flight required covering the full range of App O, specifically freezing rain,
 - develop robust and reliable discrimination of safety relevant icing conditions (e.g., freezing drizzle/rain),
 - no clear path existing yet for certification requirements for sensor technologies (including software algorithms).
- The SLD-icing poses still challenges for conventional aircraft, but icing in general is a particularly complex topic for future unconventional vehicles like UAV, UAM, more/all electric and any greener aviation vehicles due to low size/weight/power solutions, for which the SENS4ICE technologies can provide solutions. Further dedicated research and development is required for, e.g., small/ low speed/ low altitude vehicles and atmospheric conditions, including efficient and smart IPS.
- The transfer of SENS4ICE results to an arbitrary aircraft design is possible but a systematic evaluation is mandatory in order to further exploit the technologies, specifically the hybrid ice detection approach including the indirect ice detection. SENS4ICE developments were in close collaboration with the involved OEMs, which would force an even closer collaboration of OEM and ice protection system suppliers than it is for today's aircraft developments and certification.





- Safe aircraft operation in icing conditions are not solely related to atmospheric icing conditions but also to the ice formation on airframe and the corresponding degradation of flight characteristics.
 - SENS4ICE showed that the impact of SLD icing in App. O must also be considered regarding the effect on aircraft (relevant for certification) and not only detection of icing conditions.
 - This changes for view on certification path/ definition acceptable means of compliance (AMC/MoC) particularly for new aircraft designs.
- For the hybrid ice detection additional research for further maturation is still required as the technologies are currently only tested for a relatively small part of the Appendix O envelope leaving a wide part of the envelope not considered yet. Individual sensor technologies, indirect ice detection and the hybrid architectures must be tested during additional flight tests to give a more comprehensive conclusions on the approach's capabilities and performance.
- A more complete assessment of the technologies and hybrid architectures is needed to allow a better definition of required acceptable means of compliance for a potential system certification. SENS4ICE made the first step in the corresponding direction which needs to be proceeded.
- It is of high importance to better understand the actual SLD appearance during flight and the specific impact on the aircraft flight characteristics. The latter is essential for evidence-based definition of thresholds for the indirect ice detection and further understanding of required flight envelop protection in SLD-icing conditions. For this, numerical simulation or ice wind tunnel testing will not be able to replace the unique information from flight tests in natural icing conditions (particularly SLD), which are hence required in future.

Note that this is a non-exclusive list of recommendations for aircraft icing research in general. However, it reflects the major conclusions from the SENS4CIE project.





8. References

- [1] "HIDS demonstrator description document". SENS4ICE deliverable D2.6, December 2022
- [2] Christoph Deiler and Falk Sachs. "Design and testing of an indirect ice detection methodology." Vienna, Austria, June 20th - 22nd 2023. SAE International Conference on Icing of Aircraft, Engines, and Structures, SAE International, Paper 2023-01-1493.
- [3] Christoph Deiler and Nicolas Fezans. "Performance-based ice detection methodology." Journal of Aircraft, 57(2):209–223, March 2020. DOI:10.2514/1.C034828.
- [4] Anon. Ice accretion simulation. AGARD Advisory Report 344, Advisory Group for Aerospace Research & Development (AGARD) - Fluid Dynamics Panel Working Group 20, North Atlantic Treaty Organization (NATO), Neuilly-Sur-Seine, France, December 1997.
- [5] Anon., Aircraft Accident Report (NTSB/AAR-96/01, DCA95MA001), Safety Board Report, National Transportation Safety Board (NTSB), Washington, DC, USA, July 9th 1996.
- [6] SENS4ICE deliverable D4.1 Final roadmaps for future technology development and exploitation
- [7] SENS4ICE deliverable D4.2 Final report on hybrid ice detection development
- [8] SENS4ICE deliverable D4.3 Final report on airborne demonstration and atmospheric characterisation
- [9] SENS4ICE deliverable D4.4 Final report on evaluation of technologies developed in SENS4ICE and technical project results
- [10] A. Zollo, et al. „A Tool for Remote Detection and Nowcasting of In-Flight Icing Using Satellite Data,“ SAE Technical Paper2023-01-1489, <https://doi.org/10.4271/2023-01-1489>, 2023.
- [11] European Aviation Safety Agency, Certification Specifications and Acceptable Means of Compliance for Large Aeroplanes CS-25 Amendment 22, 5 November 2018.
- [12] Federal Aviation Administration, Code of Federal Regulations (CFR) Title 14 Aeronautics and Space Chapter I Federal Aviation Administration, Department of Transportation Subchapter C Aircraft Part 25 Airworthiness Standards: Transport Category Airplanes.
- [13] CORDIS EU Research and Development Information Service: SENS4ICE project profile
<https://cordis.europa.eu/project/id/824253>
- [14] SENS4ICE project website <https://www.sens4ice-project.eu>
- [15] Schwarz, C., Ohme, P., Deiler, C., "The SENS4ICE EU project – SENsors and certifiable hybrid architectures for safer aviation in Icing Environment", SAE Icing Conference on Icing of Aircraft, Engines, and Structures 2019, Minneapolis, MN, USA, 17 – 21 JUN 2019.
- [16] Schwarz, C., "The SENS4ICE EU project – SENsors and certifiable hybrid architectures for safer aviation in Icing Environment – A project midterm overview" 6th International Conference "Prospects of Civil Avionics Development", online / Moscow, Russia, GosNIIAS, July 22, 2021.
- [17] Schwarz, C., "The SENS4ICE EU project – SENsors and certifiable hybrid architectures for safer aviation in Icing Environment – Project Overview and Initial Results", International council of the aeronautical sciences (ICAS), Stockholm, Sweden, September 2022.
<https://doi.org/10.5281/zenodo.7105074>
- [18] Bansmer, S. E., Baumert, A., Sattler, S., Knop, I., Leroy, D., Schwarzenboeck, A., Jurkat-Witschas, T., Voigt, C., Pervier, H., and Esposito, B., "Design, construction and commissioning of the Braunschweig Icing Wind Tunnel", Atmos. Meas. Tech., 11, 3221–3249, DOI: 10.5194/amt-11-3221-2018, 2018.
- [19] Orchard, D. M., Clark, C., Chevrette, G., "Measurement of Liquid Water Content for Supercooled Large Drop conditions in the NRC's Altitude Icing Wind Tunnel", SAE Icing Conference on Icing of Aircraft, Engines, and Structures 2019, Minneapolis, MN, USA, 17 – 21 JUN 2019.
- [20] Lucke, J., Jurkat-Witschas, T., Heller, R., Hahn, V., Hamman, M., Breitfuss, W., Reddy Bora, V., Moser, M., and Voigt, C., "Icing wind tunnel measurements of supercooled large droplets using the 12 mm total water content cone of the Nevezorov probe", Atmos. Meas. Tech., 15, 7375–7394, DOI: 10.5194/amt-15-7375-2022, 2022
- [21] T. Jurkat-Witschas, J. Lucke, C. Schwarz, C. Deiler, F. Sachs, S. Kirschler, D. Menekay, C. Voigt, B. Bernstein, O. Jaron, F. Kalinka, A. Zollo, L. Lilie, J. Mayer, C. E. d. R. e. d. Christian Page, B. Vié, A. Bourdon, R. P. Lima und L. Vieira, „Overview of Cloud Microphysical Measurements during the SENS4ICE Airborne Test Campaigns: Contrasting Icing Frequencies from Climatological Data to First Results from Airborne Observations,“ in SAE Technical Paper Series, 2023.
- [22] R. C. Braga, D. Rosenfeld, R. Weigel, T. Jurkat, M. O. Andreae, M. Wendisch, M. L. Pöhlker, T. Klimach, U. Pöschl, C. Pöhlker, C. Voigt, C. Mahnke, S. Borrmann, R. I. Albrecht, S. Molleker, D. A.





- Vila, L. A. T. Machado und P. Artaxo, „Comparing parameterized versus measured microphysical properties of tropical convective cloud bases during the ACRIDICON–CHUVA campaign,“ *Atmospheric Chemistry and Physics*, Bd. 17, p. 7365–7386, June 2017.
- [23] S. Lance, „Coincidence Errors in a Cloud Droplet Probe (CDP) and a Cloud and Aerosol Spectrometer (CAS), and the Improved Performance of a Modified CDP,“ *Journal of Atmospheric and Oceanic Technology*, Bd. 29, p. 1532–1541, October 2012.
- [24] S. Faber, J. R. French und R. Jackson, „Laboratory and in-flight evaluation of measurement uncertainties from a commercial Cloud Droplet Probe (CDP),“ *Atmospheric Measurement Techniques*, Bd. 11, p. 3645–3659, June 2018.
- [25] L. E. Lilie, D. Bouley, C. P. Sivo und T. P. Ratovsky, „Test Results for the SEA Ice Crystal Detector (ICD) under SLD Conditions at the NASA IRT,“ 2021.
- [26] Schwarz, C., „SENS4ICE EU project preliminary results“, SAE International Conference on Icing of Aircraft, Engines, and Structures 2023, Vienna, Austria, 20-22 June 2023, 2023-01-1496.
- [27] EUROCAE, ED-103A/B Minimum operational performance standard for inflight icing detection systems. November 2017. <http://www.eurocae.net>
- [28] Hamman, M., Gelao, G., Ridouane, El H., Chabukswar, R., Botura, G., „Development and Validation Testing of the Collins Ice Differentiator System in App C and App O Icing Conditions“, SAE International Conference on Icing of Aircraft, Engines, and Structures 2023, Vienna, Austria, 20 – 22 June 2023, 2023-01-1490.
- [29] Bouchard, A. et al., „Relationship between airborne electrical and total water content measurements in ice clouds“, *Atmospheric Research*, Vol 237, 103836, 2020, DOI: 10.1016/j.atmosres.2019.104836
- [30] B. Bernstein, „Meteorological Analysis of Selected Natural Icing Flights – SENS4ICE North America Campaign“, Leading Edge Atmospherics, LLC, 2023
- [31] S. G. Cober und G. A. Isaac, „Characterization of Aircraft Icing Environments with Supercooled Large Drops for Application to Commercial Aircraft Certification“, *Journal of Applied Meteorology and Climatology*, Bd. 51, p. 265–284, February 2012.

DISCLAIMER

The Phenom 300 flight test data analysed is based on an experimental prototype. This aircraft prototype has embedded additional flight test instrumentation and features that do not represent any certified Phenom 300 aircraft model. Therefore, the analysis and performance estimations assessed in this study and within the SENS4ICE project do not represent the Phenom 300's certified performance.

Airborne data was obtained using the aircraft managed by Safire, the French facility for airborne research, and infrastructure of the French National Center for Scientific Research (CNRS), Météo-France and the French National Center for Space Studies (CNES). Distributed data are processed by SAFIRE.





9. Annex Horizon 2020 TRL Definitions

TRL	Horizon 2020 Definitions	Appendix C Detection	Appendix O [FZDZ only] Detection	Appendix O [FZDZ only] Discrimination	Example: forward scatter particle instrument for Appendix C (e.g. DMT's CDP)
TRL 6	technology demonstrated in relevant environment (industrially relevant environment in the case of key enabling technologies)	"Prototype built and tested over 5-10 conditions within the App C envelope in a relevant environment (IWT or FT). Some calculations or analysis should be included to show extension of coverage to non-tested cases."	"Prototype built and tested over 3-5 conditions within the App. O [FZDZ only] envelope in a relevant environment (IWT or FT). Some calculations or analysis should be included to show extension of coverage to non-tested cases."	"Prototype built and tested over 3-5 conditions within the App. O [FZDZ only] envelope and 5-10 conditions within the App. C envelope in a relevant environment (IWT or FT). This should include at least two test points where the size distributions of App. C and App. O [FZDZ only] overlap. Some calculations or analysis should be included to show extension of coverage to non-tested cases."	Build of prototype; tested for performance over 8 conditions within the App. C size range within an IWT and demonstration of system during flight test.
TRL 5	technology validated in relevant environment (industrially relevant environment in the case of key enabling technologies)	"Testing of key components or subsystems to show it can withstand relevant environmental conditions for proposed installation location on aircraft. Could also be testing of a full detector system but only in part of the set of required environmental conditions"	"Testing of key components or subsystems to show it can withstand relevant environmental conditions for proposed installation location on aircraft. Could also be testing of a full detector system but only in part of the set of required environmental conditions"	"Testing of key components or subsystems to show it can withstand relevant environmental conditions for proposed installation location on aircraft. Could also be testing of a full detector system but only in part of the set of required environmental conditions"	Testing of the photodetector and laser (or assembly) to show it can withstand relevant environmental conditions for proposed installation location on aircraft, which is outside the aircraft's skin.
TRL 4	technology validated in lab	"Build of prototype for lab testing; demonstration of detection of icing conditions (e.g. droplets, LWC, etc) or ice accretion over several conditions (3-5) within the App. C envelope. Some calculations or analysis should be included to show extension of coverage to non-tested cases."	"Build of prototype for lab testing; demonstration of detection of icing conditions (e.g. droplets, LWC, etc) or ice accretion over at least 2 conditions within the App. O [FZDZ only] envelope. Some calculations or analysis should be included to show extension of coverage to non-tested cases."	"Build of prototype for lab testing; demonstration of identification of icing conditions (e.g. droplets, LWC, etc) or ice accretion as App. O [FZDZ only]. This could be through the detection of both App. O [FZDZ only] vs App. C and subsequent discrimination or through an insensitivity to App. C. This should include at least four conditions, including at least one where the size distributions of App. C and App. O [FZDZ only] overlap."	"Build of non-environmentally robust prototype for testing with lab based spray nozzle or droplet generator covering the full App. C size range and some of the particle density range. Calculations completed to show the full particle density range can be measured."
TRL 3	experimental proof of concept	Build of prototype for lab testing; demonstration of detection of icing conditions (e.g. droplets, LWC, etc) or	Build of prototype for lab testing; demonstration of detection of icing conditions (e.g. droplets, LWC, etc) or	"Build of prototype for lab testing; demonstration of identification of icing conditions (e.g. droplets, LWC, etc) or ice accretion as App. O [FZDZ only]. This could be	Build of prototype for testing with lab based spray nozzle or droplet generator covering 2 conditions the App. C size range





		ice accretion over 1-2 conditions within the App. C envelope as a proof of concept.	ice accretion over at least one condition within the App. O [FZDZ only] envelope as a proof of concept.	through the detection of both App. O [FZDZ only] vs App. C and subsequent discrimination or through an insensitivity to App. C. This should include at least one test of an App. C condition and at least one test of an App. O [FZDZ only] condition."	
TRL 2	technology concept formulated	Basic detector design completed with relevant calculations completed	Basic detector design completed with relevant calculations completed	Basic detector design completed with relevant calculations completed	Basic detector design created; scattering collection estimated using Mie scattering theory; required laser power / detector efficiencies estimated
TRL 1	basic principles observed	Demonstration of the basic principles of detecting App. C icing conditions or ice accretion.	Demonstration of the basic principles of detecting App. O [FZDZ only] icing conditions or ice accretion.	Demonstration of the basic principles of discriminating App. O [FZDZ only] vs App. C icing conditions or ice accretion.	Demonstration of detection of optical forward scatter from liquid droplets within the App. C size range.
Notes	https://ec.europa.eu/research/participants/data/ref/h2020/wp/2014_2015/annexes/h2020-wp1415-annex-q-trl_en.pdf				http://www.dropletmeasurement.com/cloud-droplet-probe-cdp-2

